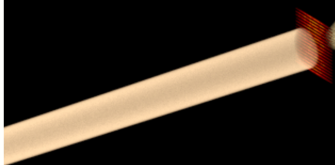
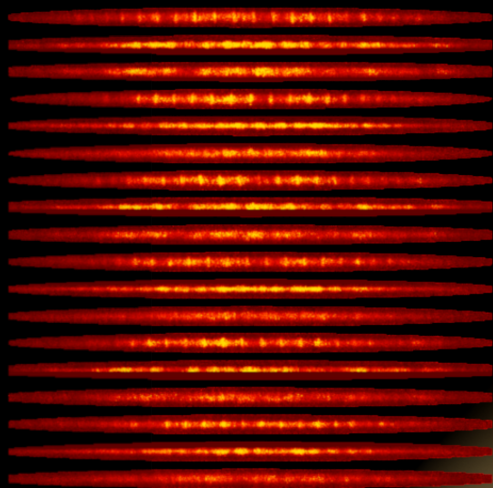


Space-time crystals in Bose-Einstein condensates



Jasper Smits

Space-time crystals in Bose-Einstein condensates

Ruimte-tijd kristallen in Bose-Einstein condensaten

Jasper Smits

Cover

Synthetic space-time Bragg diffraction on a space-time crystal,
by Dries van Oosten, with data from this work

Smits, Jasper

Ruimte-tijd kristallen in Bose-Einstein condensaten

J. Smits - Utrecht

Universiteit Utrecht

Faculteit Bètawetenschappen

Departement Natuurkunde

Thesis Universiteit Utrecht - With a summary in Dutch

ISBN: 978-90-393-7395-8

DOI: 10.33540/701

Space-time crystals in Bose-Einstein condensates

Ruimte-tijd kristallen in Bose-Einstein condensaten

(met een samenvatting in het Nederlands)

Proefschrift

ter verkrijging van de graad van doctor
aan de Universiteit Utrecht op gezag van
de rector magnificus, prof. dr. H.R.B.M. Kummeling,
ingevolge het besluit van het college voor promoties
in het openbaar te verdedigen
op maandag 20 september 2021
des middags te 12.15 uur

door

Jasper Smits

geboren op 27 december 1991 te Bernisse

Promotor: Prof. dr. P. van der Straten
Copromotor: Dr. D. van Oosten

*voor
mijn vader, moeder, broertje en zusje*

Contents

| | | |
|----------|-------------------------------------------------------------|-----------|
| 1 | Introduction | 1 |
| 1.1 | History of BEC | 2 |
| 1.2 | Symmetry breaking | 4 |
| 1.2.1 | The space-time crystal | 5 |
| 1.3 | Thesis outline | 6 |
| 2 | Setup | 11 |
| 2.1 | Manipulation of gaseous sodium | 12 |
| 2.1.1 | Properties of gaseous sodium | 12 |
| 2.1.2 | Laser system | 15 |
| 2.2 | Experimental setup and sequence | 16 |
| 2.2.1 | Sodium source | 17 |
| 2.2.2 | Laser cooling | 18 |
| 2.2.3 | Magnetic confinement | 21 |
| 2.2.4 | Evaporative cooling | 23 |
| 2.2.5 | Imaging | 23 |
| 2.3 | Experimental control | 25 |
| 2.3.1 | Control software | 25 |
| 2.3.2 | Control hardware | 27 |
| 2.4 | Data management | 29 |
| 3 | Imaging trapped quantum gases by off-axis holography | 37 |
| 4 | Observation of a Space-Time Crystal | 51 |
| 4.1 | Experiment | 53 |
| 4.2 | Simulations | 57 |
| 4.3 | Long-time behavior | 59 |

| | | |
|----------|------------------------------------------------------------|------------|
| 4.4 | Model | 61 |
| 4.5 | Conclusion | 64 |
| 5 | Dynamics of a Space-Time Crystal | 67 |
| 5.1 | The experiment | 69 |
| 5.2 | Effective action | 71 |
| 5.3 | Comparison to simulations | 76 |
| 5.4 | No mode coupling | 79 |
| 5.5 | Back-action | 82 |
| 5.6 | The Hamiltonian | 83 |
| 5.7 | Onset of the space-time crystal | 85 |
| 5.8 | Conclusion and outlook | 90 |
| 6 | Long-term stability of space-time crystals | 95 |
| 6.1 | Experiment | 96 |
| 6.2 | Modelling | 100 |
| 6.3 | Experimental results | 105 |
| 6.3.1 | Breaking discrete time symmetry | 108 |
| 6.3.2 | Growth rate | 108 |
| 6.3.3 | Saturation | 110 |
| 6.4 | Conclusion and outlook | 113 |
| 7 | Spontaneous breaking of a time-translation symmetry | 119 |
| 7.1 | Methods | 130 |
| 7.1.1 | Experiment | 130 |
| 7.1.2 | Analysis | 133 |
| 7.1.3 | Number of quanta | 135 |
| 7.1.4 | Initial number of quanta | 136 |
| 7.1.5 | Fluctuations in the growth | 136 |
| 7.1.6 | Dependencies on system parameters | 137 |
| | Samenvatting | 143 |
| | CV and Publications | 151 |
| | Dankwoord | 153 |

1 Introduction

PHASES of matter and the transitions between these phases have been one of the fascinations of scientists since the start of written history. In ancient times, Greek philosophers argued over what constitutes matter. Later, during the 18th and 19th century, scientists explored the possibility of molecules as combinations of atoms as the building blocks of all matter. They thought that these molecules exist in three states: gas, solid and liquid and to go between these states one has to vary the pressure or temperature of the material. Taking water as an example: starting at room temperature and cooling down, at 0 °C the water will turn from a liquid into a crystalline solid. This transition from one phase into the other, the phase transition, is well known to everyone but when looking at it closely some interesting things can be learned. While the temperature is decreased in a continuous manner, without sudden steps, the ordering of the material changes discontinuously, from a liquid in which all particles are free to move around, to a solid in which particles are pinned in place in a crystal lattice. These changes to material properties, such as density or ordering, as a result of changes in external variables, such as temperature or pressure, are characteristic of phase transitions. Since the earliest days of science, many new phases of matter have been discovered, such as ionized plasma, the quark-gluon plasma at the Large Hadron Collider and the Bose-Einstein condensate. This last one, the Bose-Einstein condensate (BEC), is what this work is about.

1.1 History of Bose-Einstein condensation

When Satyendra Nath Bose was developing the theory that later becomes the groundwork for the Bose-Einstein statistics, he was not trying to explain a new phase of matter, but rather trying to elucidate Planck's law, which describes the spectrum of black body radiation [1]. Having trouble getting his work published, he contacted Albert Einstein in an attempt to collaborate: convincing Einstein was the way to get his work published. Einstein did help Bose get his work published [2], but he also realised that while Bose only applied the theory to quanta of light, the theory can be applied to ideal gases as well. In his work *Quantentheorie des einatomigen idealen Gases* (1924) [3] (Quantum theory of the monoatomic ideal gas) Einstein derived all the associated thermodynamical relations associated with Bose's new statistics. Revisiting the topic a year later, in 1925 [4], he derived that, according to this theory, the system has capacity for only a finite number of thermal particles. As a result, if the total number of particles exceeds this capacity for thermal particles, the excess particles form a "condensate" of particles which gather in the lowest energy state, a new phase of matter. Since the availability of thermal states is dependent on the temperature, this alludes to the existence of a phase transition at some critical temperature at which the particle number exceeds the number of available thermal states. It was shown that the transition between a thermal gas and a Bose-Einstein condensate occurs approximately at the temperature at which the phase space density¹ is equal to unity.

At the time this new phase of matter was first predicted, the only accessible Bose-Einstein condensate was Helium-II. Liquid Helium cooled below its critical temperature (also known as the λ -point, at 2.18 Kelvin) exhibits superfluid behavior. When a superfluid is stirred, not one big vortex forms but a lattice of small vortices. In general, a Bose-Einstein condensate with interactions between its constituents is a superfluid; a fluid which can flow around obstacles without generating any heat. Helium-II exhibits

¹The phase space density is equal to the cube of the thermal wavelength of the particles, multiplied by the number density

superfluidity but due to the strong interactions between particles it is an extremely difficult system to study isolated phenomena in, and to describe theoretically. The Bose-Einstein condensate can be described by a single many-body wave function depending on the position of all particles. However, to effectively apply mean-field approximations, a more dilute medium is preferable. In the case of more dilute BECs, the Hartree-Fock approximation can be applied. The many-body wave function is then approximated by the product of identical single-particle wave functions and the condensate can be described by a single quantum mechanical wave function as if it was a single particle [5, 6]. When two of these Bose-Einstein condensates mix a matter interference pattern can be observed due to interference of the quantum mechanical wave functions, alike to classical waves such as light and waves on water.

Temperatures in the order of nanokelvins² are required in order to reach the critical temperature in dilute atomic gases, which were far beyond the experimental capabilities of the 1930's. The realization of the first gaseous Bose-Einstein condensate was eventually made possible by advances in cold atom physics. By bringing atoms into a vacuum, they are isolated from the environment. Atoms were initially shaped into beams and these beams were manipulated by light from gas lamps containing the same element as was used in the experiment, and later with lasers. The implementation of lasers was a large improvement, allowing for narrow-linewidth light sources. With the advances in Doppler cooling in the '80s, it was made possible to exert great forces on atoms, slowing atoms down from thermal velocities to a near standstill [7–9]. As these techniques matured, the Magneto-Optical Trap (MOT) was developed [10, 11]. In a MOT, atoms could be suspended in vacuum by a combination of laser beams and magnetic fields, and temperatures in the order of hundreds of microkelvins could be reached. For the advances in laser cooling of neutral atoms the Nobel Prize in Physics in 1997 was awarded to Steven Chu, Claude Cohen-Tannoudji and William Phillips.

²Degrees in the Kelvin temperature scale are the same as those in the Celsius scale, but the Kelvin scale is shifted such that zero Kelvin corresponds to the point of no thermal energy, so $0\text{ K} = -273.15\text{ }^\circ\text{C}$.



The MOT provides a good starting point for reaching Bose-Einstein condensation, but to reach Bose-Einstein condensation the temperature has to be decreased by another 3 orders of magnitude. To achieve this, the atoms are transferred to a magnetic trap. Subsequently, those atoms with energy, which is many times the average energy, are removed. As a result, the temperature of the sample is brought down to below the threshold for Bose-Einstein condensation. In this way, the first gaseous BEC was formed. Finally, Bose-Einstein condensation was achieved seventy years after its initial theorization, in 1995, independently at *JILA* [12] and *MIT* [13], for which Eric Cornell, Wolfgang Ketterle and Carl Wieman received the Nobel Prize in Physics in 2001.

1.2 Symmetry breaking as signature for phase transitions

In modern physics phase transitions are usually identified by a broken symmetry. In the (classical) example of freezing water, a transition from a liquid to a solid, the particles are free to move around in the liquid, while in the solid they are pinned in a crystalline lattice. If the system is assumed to be sufficiently large, the liquid has a continuous rotational and translation symmetry. The solid, however, has a discrete rotational and translational symmetry. It is said that this breaks the continuous rotational and translational symmetries, as the solid has rotational and translational symmetries, but the discrete symmetries of the solid are less general than the continuous symmetries of the liquid.

Theoretically, the physics is usually described by a Hamiltonian. A Hamiltonian is a functional for the energy of the system. This Hamiltonian will possess certain symmetries, such as translational or rotational symmetry. Symmetry breaking can then be described mathematically. A symmetry is said to be broken if a realization of the system does not possess the same symmetries as the Hamiltonian governing this system. In the case of Bose-Einstein condensation, the symmetry that is broken is a

$U(1)$ symmetry, the symmetry associated with the phase of a complex number. The Hamiltonian governing dynamics in a BEC generally does not pin the overall phase at any value, but any measurement of the phase returns a well-defined value. This implies that at the moment the BEC is formed, the phase is not yet determined. At the moment the phase is measured and returns a well-defined value, and the $U(1)$ symmetry is broken spontaneously.

1.2.1 The space-time crystal

The chapters of this dissertation are all related to a novel phenomena: the space-time crystal. In 2012 Frank Wilczek suggested that a system can be engineered in such a way that it breaks the continuous time translation symmetry in the ground state, thus forming a *time crystal*, analogous to spatial crystals breaking the continuous spatial translation symmetry [14, 15]. His suggestions encountered a lot of criticism and debate is still ongoing whether the continuous time translation can be broken in the ground state of a system [16–18]. However, they did give birth to the field of *discrete time crystals*³ [19–24]. In a system in which the continuous time translation symmetry is already broken by a periodic driving force, a discrete time crystal can be realised. A discrete time crystal breaks the symmetry of the underlying Hamiltonian; while the Hamiltonian is modulated with a period T , the time crystal is realised at a subharmonic of the drive with a period nT . The discrete time translation symmetry is thus broken into another discrete symmetry time translation symmetry.

We have realised a so-called space-time crystal in a BEC. Our BEC is trapped in a magnetic trap with a large aspect ratio leading to a cigar-shaped BEC. By squeezing the trap in the radial direction, the width of the BEC is made to oscillate, which functions as a drive. The drive couples to longitudinal modes through the non-linear (density-density) interaction in the BEC. The excited longitudinal modes oscillate at exactly half the driving frequency at

³Also sometimes referred to as *Floquet time crystal*



a subharmonic response. Every realization of a BEC in our setup has a slightly varying particle number and, as a result, varying dimensions. However, even with particle number variations as high as 10%, the longitudinal modes are observed consistently when the experiment is performed under otherwise equal conditions. This shows no fine-tuning of the system is required to observe this subharmonic response. Finally, as the BEC is a superfluid and the thermal fraction is small, the dissipation is very small. The observed longitudinal modes persist for many oscillation periods, with no sign of damping due to dissipation. Due to the apparently small coupling between the heat bath of the thermal cloud and the longitudinal mode, we assume that our observed mode is in a pre-thermal phase, a phase which has yet to thermalize and does so very slowly. We conclude the observation of a pre-thermal discrete time crystal with periodic spatial pattern, a space-time crystal.

1.3 Thesis outline

In Chapter 2, the experimental setup as it was used in Utrecht is described. Components of the setup which I have contributed to are described in detail, while existing parts of the setup are explained briefly and references to other dissertations with more information are given. There is a special emphasis on data collection and (responsible) data management.

In Chapter 3 a novel imaging method based on off-axis holography is presented. By using an external reference beam, the light used to probe the atoms can be used more efficiently such that less light is needed, reducing atom losses from imaging. In addition, both amplitude and phase of the light field can be extracted which allows image post-processing such as refocusing. Refocusing makes it unnecessary to physically align the imaging system perfectly, as numerical propagation enables one to always digitally refocus.

In Chapter 4 the initial observation of the space-time crystal is described. The

transverse breathing mode is considered as the driving excitation and a series of image is taken. A line density profile is calculated for each image in a series and stacked to create a space-time image of the crystal. By taking a Fourier transform of this image, we perform a synthetic Bragg diffraction experiment in space and time. A comparison is made to numerical simulations of the Gross-Pitaevskii equation and a good quantitative agreement is found.

In Chapter 5 a model to describe the formation of the space-time crystal is derived from the Gross-Pitaevskii equation. By comparison to simulation data, it is shown that the model can be used to predict the initial growth of the crystal. The mode function which is used as *Ansatz* is confirmed to be correct, but a small discrepancy between the predicted mode number and the mode number observed in experiment and simulation is noted.

In Chapter 6 the holographic imaging method is used to realise a significant improvement in data quality and quantity. While in Chapter 4 only thirty images can be taken in a single measurement run, in Chapter 6 this number is increased to 250 images. As a result the growth and dynamical stability can be studied. The model from Chapter 5 is expanded to also include a (dissipative) saturation term. It is shown that for realistic parameters of the model the growth and behaviour observed in the experiment are predicted.

Finally, in Chapter 7 the statistics of the phase lag between the transverse breathing mode and the time crystal are analyzed. It is found that the phase lag is bunched into two separate, approximately Gaussian peaks with a phase difference of π in between them. The technical reasons this symmetry breaking can occur is given. Analysis of these technical reasons excludes a technical source as source of the broken symmetry. The experimental results show a fifty-fifty split between the two phase lags. It is concluded that the symmetry is broken spontaneously.



References

- [1] M. Planck, *Verhandl. Dtsch. phys. Ges.* **2**, 237 (1900).
- [2] S. N. Bose, *Zeitschrift für Physik*, 178 (1924).
- [3] A. Einstein, *Sitzungsberichte der Preußischen Akademie der Wissenschaften zu Berlin*, 261 (1924).
- [4] A. Einstein, *Sitzungsberichte der Preußischen Akademie der Wissenschaften zu Berlin*, 3 (1925).
- [5] E. P. Gross, *Il Nuovo Cimento (1955-1965)* **20**, 454 (1961).
- [6] L. P. Pitaevskii, *J. Exptl. Theoret. Phys. (U.S.S.R.)* **40**, 646 (1961).
- [7] T. Hänsch and A. Schawlow, *Optics Communications* **13**, 68 (1975).
- [8] D. Wineland and H. Dehmelt, *Bull. Am. Phys. Soc.* **20**, 637 (1975).
- [9] W. D. Phillips and H. Metcalf, *Phys. Rev. Lett.* **48**, 596 (1982).
- [10] S. Chu, L. Hollberg, J. E. Bjorkholm, A. Cable, and A. Ashkin, *Phys. Rev. Lett.* **55**, 48 (1985).
- [11] E. L. Raab, M. Prentiss, A. Cable, S. Chu, and D. E. Pritchard, *Phys. Rev. Lett.* **59**, 2631 (1987).
- [12] M. H. Anderson, J. R. Ensher, M. R. Matthews, C. E. Wieman, and E. A. Cornell, *Science* **269**, 198 (1995).
- [13] K. B. Davis, M.-O. Mewes, M. R. Andrews, N. J. van Druten, D. S. Durfee, D. M. Kurn, and W. Ketterle, *Phys. Rev. Lett.* **75**, 3969 (1995).
- [14] A. Shapere and F. Wilczek, *Phys. Rev. Lett.* **109**, 160402 (2012).
- [15] F. Wilczek, *Phys. Rev. Lett.* **109**, 160401 (2012).
- [16] P. Bruno, *Phys. Rev. Lett.* **110**, 118901 (2013).
- [17] P. Nozières, *Europh. Lett.* **103**, 57008 (2013).
- [18] H. Watanabe and M. Oshikawa, *Phys. Rev. Lett.* **114**, 251603 (2015).
- [19] K. Sacha, *Phys. Rev. A* **91**, 033617 (2015).
- [20] D. V. Else, B. Bauer, and C. Nayak, *Phys. Rev. Lett.* **117**, 090402 (2016).

-
- [21] D. V. Else, B. Bauer, and C. Nayak, *Phys. Rev. X* **7**, 011026 (2017).
- [22] V. Khemani, A. Lazarides, R. Moessner, and S. L. Sondhi, *Phys. Rev. Lett.* **116**, 250401 (2016).
- [23] C. W. von Keyserlingk, V. Khemani, and S. L. Sondhi, *Phys. Rev. B* **94**, 085112 (2016).
- [24] K. Sacha and J. Zakrzewski, *Rep. Progr. Phys.* **81**, 016401 (2018).



2 Setup

In this Chapter I will discuss the requirements for realizing a Bose-Einstein condensate of sodium atoms. Parts of the process which have been adequately described in previous PhD theses will be discussed concisely with references to previous work for a more detailed description. Special attention is paid to the experimental control, both hardware and software, which has been updated during my time in Utrecht.



To reach the extremely low temperatures ($< 1\ \mu\text{K}$) required for Bose-Einstein condensation (BEC) a combination of laser Doppler cooling and evaporative cooling is used. Under high vacuum conditions, with pressures below 10^{-7} mbar, sodium atoms are heated in an oven. The oven produces a jet of sodium atoms, which is injected into a Zeeman slower [1]. The Zeeman slower slows the atoms almost to a stop. After the Zeeman slower, the atoms are captured and cooled in a magneto-optical trap [2, 3]. Atoms from the magneto-optical trap are transferred to a magnetic trap in which evaporative cooling takes place. Evaporative cooling can be used to produce a Bose-Einstein condensate directly. Alternatively, atoms can be transferred to the optical trap prior to crossing the critical temperature for Bose-Einstein condensation. In this case the final part of the evaporative cooling process is completed in the optical trap. The atoms are imaged during the experiment using either one of the established [4] techniques of absorption imaging or phase-contrast imaging, or the holographic techniques newly developed as part of this work. A description of the holographic imaging techniques can be found in Chapter 3.



This Chapter will first outline the properties of sodium and the laser setup in Sec. 2.1. In Sec. 2.2 I discuss how a Bose-Einstein condensate is realized by a combination of laser cooling and evaporative cooling, with a brief reference to the typical parameters used in imaging during calibration. In Sec. 2.3 I discuss the experimental control systems in more detail. In Sec. 2.4 I discuss the way data are managed from the moment of acquisition to the moment of publication.

2.1 Manipulation of gaseous sodium

Alkali metals are generally known for their corrosive nature and their spectacular and explosive chemical reactions when exposed to water [5]. In (ultra)cold atoms experiments the alkali metals are contained in a vacuum chamber under ultra high vacuum (typically 10^{-7} mbar at the sodium source, down to 10^{-10} mbar in the experimental chamber in our case) and the reactive properties of the alkali only become apparent when the vacuum is broken, either when the source has to be replenished or in case of a vacuum failure. Cold atom physicists, therefore, are interested in different properties of their alkali metal of choice: How does this atom interact with light when it is in a dilute gas phase? What are the collisional properties of this atom at ultra-low ($< 1 \mu\text{K}$) temperatures?

2.1.1 Properties of gaseous sodium

All experiments described in this dissertation have been performed using sodium atoms. Sodium is one of the alkali metals, which gives it a fairly uncomplicated electronic structure with transitions between ground and excited states that can be excited with visible light. These accessible optical transitions have a sufficiently large linewidth (~ 10 MHz), making sodium an excellent atom to perform laser cooling on. Moreover, sodium has only one stable isotope, sodium-23, which means that no enrichment has to take place, as is the case for some of the other alkali metals. Sodium-23 is bosonic

and has a positive s -wave scattering length. The positive s -wave scattering length is vital in providing a repulsive potential between atoms at low energy, as condensates made of particles with a negative s -wave scattering length collapse when a critical particle number is reached [6, 7]. Sodium has a very favorable ratio between its two- and three-body inelastic collision cross-section which makes it suitable for creating large Bose-Einstein condensates [8]. As three-body processes will limit particle number towards the end of the cooling process, higher collision rates can be attained during the cooling process, compared to other atomic species, leading to more efficient cooling.

The optical transitions used in this work are those between the $3^2S_{1/2}$ ground state and the $3^2P_{3/2}$ excited state, *i.e.* the D_2 line, with a resonance wavelength of around $\lambda = 589.16$ nm. A detailed representation of both ground and excited states can be seen in Fig. 2.1. Hyperfine splitting splits the ground state into a $F = 1$ state and a $F = 2$ state. The frequency splitting between these two ground states is approximately 1.8 GHz. The excited state is also split by hyperfine splitting but into four distinct hyperfine states $F' = 0, \dots, 3$, with a frequency difference in the order of 100 MHz between the outermost states. Each hyperfine state is moreover split into $2F + 1$ magnetic substates. The energy shift of the magnetic substates, commonly referred to as the Zeeman shift, depends on the strength of the magnetic field and can for low fields, in the order of several tens of Gauss, be approximated to be proportional to the magnetic field strength. The proportionality constant between magnetic field strength and frequency shift, for each hyperfine state, is displayed on the right side of Fig. 2.1.

Some basic properties of sodium, both optical and otherwise, are shown in Table 2.1. Constants listed here are used throughout this dissertation. The scattering length mentioned is that between atoms in the atoms in the $F = 1, m_F = -1$ state, which is the only ground state occupied in BEC experiments throughout this dissertation. Linewidth and lifetime are properties of the $3^2P_{3/2}$ excited state.



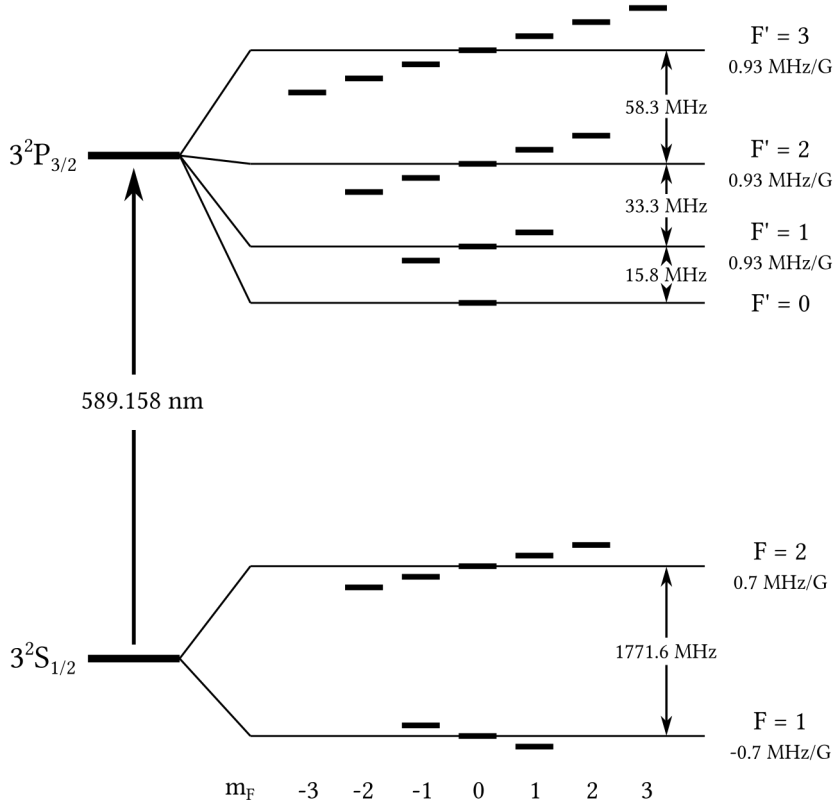


Figure 2.1: Level scheme of sodium. The difference between energy levels is not to scale. The frequency splitting displayed for the ground state hyperfine states is obtained from Ref. [9] and the frequency splittings for the excited hyperfine states are obtained from Ref. [10]. The Zeeman shift is obtained from Ref. [11].

Table 2.1: Some general properties of sodium-23.

| Basic properties | | |
|-------------------------------|----------------------------|----------|
| Number of protons N | 11 | [12] |
| Number of nucleons $N + Z$ | 23 | [12] |
| Atomic mass m | 22.990 u | [12] |
| | 3.817×10^{-26} kg | |
| Scattering Length | | |
| a_s | $52.98 a_0$ | [13] |
| | 2.804 nm | |
| Optical Properties | | |
| Vacuum wavelength λ_0 | 589.1583264(15) nm | [14] |
| Linewidth Γ | $2\pi \times 9.746$ MHz | [11] |
| Lifetime τ | 16.2492(77) ns | [15, 16] |

2.1.2 Laser system

To manipulate the atoms in the vacuum an arrangement is needed of laser beams with light tuned to the right frequency. Due to the large splitting between the hyperfine ground states in the $3^2S_{1/2}$ two laser systems are used: one locked to a transition from the $F = 1$ ground state and one locked to a transition from the $F = 2$ ground state. A schematic representation of the laser table can be found in Ref. [17]. Both lasers¹ are tuned to the vacuum wavelength $\lambda_0 = 589.16$ nm and locked, using Doppler-free absorption spectroscopy [18], to the atomic transition. An error signal is generated using a lock-in amplifier. To this end, the frequency of the one of the beams in the spectroscopy is scanned with small bandwidth using an acousto-optic modulator. The laser locked to the transition from the $F = 2$ ground state, which will be referred to in the following paragraphs as the “ $F = 2$ laser”, is locked -78 MHz from the $F = 2$ to $F' = 3$ transition. The laser locked to the transition from the $F = 1$ ground state, which will be referred to in the following paragraphs as the “ $F = 1$ laser”, is locked

¹Toptica TA-SHG Pro

Table 2.2: List of beams generated from the $F = 1$ laser. Detuning is shown with respect to the $F = 1$ to $F' = 1$ transition.

| Beam | Detuning (MHz) | Power (mW) |
|-----------------|-----------------------|-------------------|
| Probe/Reference | -340 - +10 | 0.005-0.1 |
| Spinpol | 0 | 5 |
| MOT Repump | +34 | 10 |
| Zeeman Repump | -334 | 7 |

Table 2.3: List of beams generated from the $F = 2$ laser. Detuning is shown with respect to the $F = 2$ to $F' = 3$ transition.

| Beam | Detuning (MHz) | Power (mW) |
|-------------|-----------------------|-------------------|
| MOT XY | -15 | 75 |
| MOT Z | -16 | 20 |
| Zeeman | -335 | 300 |

-80 MHz from the $F = 1$ to the $F' = 1, 2$ cross-over transition. The $F = 1$ laser is locked to this cross-over transition as it is by far the strongest peak in the signal. The power of each laser is distributed over different beam paths using half-wave plates and polarizing beam splitters. For each beam, the desired frequency is obtained by shifting the frequency using an acousto-optic modulator (AOM). All beams generated from light from the $F = 1$ and $F = 2$ lasers are shown Table 2.2 and 2.3, respectively.

2.2 Experimental setup and sequence

To create a Bose-Einstein condensate a large vacuum chamber is required to sufficiently isolate the atoms from the environment during the slowing and cooling processes. A schematic overview of the vacuum setup can be seen in Fig. 2.2. The vacuum setup in Utrecht is divided into three parts: sodium oven, Zeeman slower and experimental chamber. Each of the parts is isolated from

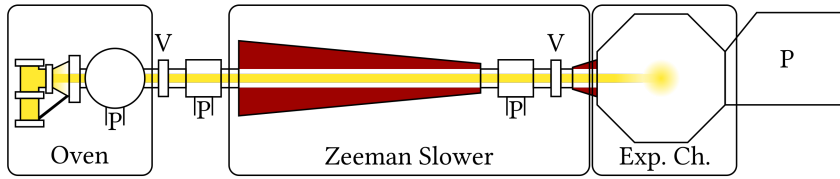


Figure 2.2: Schematic overview of the full vacuum setup with the three segmented parts indicated. Symbol V represents a valve while symbol P represents a vacuum pump. The red shaded areas indicate the coils of the Zeeman slower. Image is not to scale.

the others by electronically controlled, air-pressure operated vacuum valves. In case of a (partial) vacuum failure, electronic failure, or loss of air-pressure these valves will close such that vacuum is maintained for an extended period of time providing extra time for troubleshooting. The segmented nature of the vacuum system also allows replacement of the sodium oven while keeping the rest of the experimental setup at ultra-high vacuum, saving time after oven replacement.

2.2.1 Sodium source

To obtain sodium vapor for laser cooling, approximately 25 g of sodium is heated to 320°C in a recirculation oven [19]. As shown in Fig. 2.3, the oven is divided into two chambers, separated by the first diaphragm. The primary chamber produces the sodium vapor at controlled pressure and temperature, which will exit through the diaphragm. To produce a beam with small divergence, a secondary diaphragm is placed at the exit of the secondary chamber. The sodium which collects in the secondary chamber flows back into the primary chamber through a 2 mm diameter recirculation tube connecting the bottom of the second chamber with the bottom of the primary chamber to prevent collection of sodium in the secondary chamber. Sodium will aggregate at the coolest point in the primary chamber causing the coolest point in the oven to determine



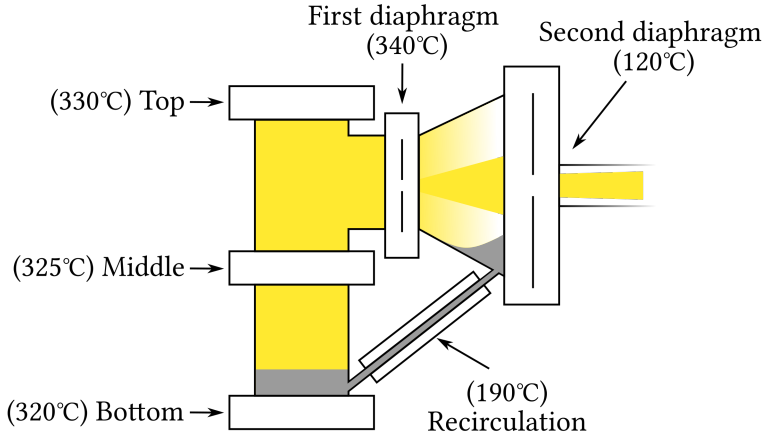


Figure 2.3: Schematic representation of the sodium recirculation oven used in our experiment. The temperature setting of the heating elements located at different positions are shown.

the pressure and temperature of the gas. To prevent collection of sodium elsewhere a slight temperature gradient across the primary chamber is maintained. To provide homogeneous heating it is imperative that the oven is tightly wrapped in insulation, as the stainless steel of which the chamber is constructed does not conduct heat sufficiently to attain a homogeneous temperature. Insufficient insulation will thus lead to cold spots where insulation is lacking, requiring significantly higher temperatures, up to 70°C above the desirable set point. These required higher temperatures will in turn impact heating element lifetime, leading to more downtime.

2.2.2 Laser cooling

Sodium atoms leave the oven with a mean velocity of approximately 800 m/s. To slow down the atoms, a Zeeman slower is used [20]. A circularly polarized laser beam is used to cycle atoms between the $|F = 2, m_F = 2\rangle$ and $|F' = 3, m_{F'} = 3\rangle$ states. Note that atoms from the

$|3', 3'\rangle^2$ state can only decay to the $|2, 2\rangle$ state due to selection rules, thus this is a closed. An inhomogenous magnetic field is used to counteract the change in Doppler shift the atoms will experience as they slow down. Due to stray magnetic fields, non-linear Zeeman shifts and slightly elliptical polarization of the Zeeman beam, atoms will sometimes be excited to the $|2', 2'\rangle$ state, from which they can decay to the $F = 1$ ground state. As the splitting between the $F = 1$ and $F = 2$ ground states is many linewidths, a second beam (repump beam) is needed, locked from the $F = 1$ ground state to the $F' = 2$ excited state. This second beam will bring atoms back into the cooling cycle, as atoms re-excited to the $F' = 2$ excited state by the repump beam have a chance to decay to the $F = 2$ ground state and re-enter the cooling process. As can be seen in Tabs. 2.2 and 2.3, the Zeeman beam typically has a few orders of magnitude larger power than the repump beam. Polarization and beam path of both beams are the same. The Zeeman slower in our setup is split in two parts, with the first part slowing atoms from 800 m/s to 200 m/s and the second part slowing atoms from 200 m/s to the capture velocity for our Magneto-Optical Trap (MOT). This is done to combat beam divergence. As the atoms slow down, the distribution of longitudinal velocity is compressed, but the radial velocity distribution is unchanged. So, since only the longitudinal velocity profile is cooled, the divergence will increase as the atoms slow down. To circumvent the problem of the transverse spreading, the final stage of slowing is done right before the atoms enter the experimental chamber, which makes divergence less of a problem as less distance has to be travelled before the capture point. In Fig. 2.4 an overview of the magnetic field strength inside the Zeeman coils is shown. From this, the “resonant velocity” is calculated by taking the expression for Doppler and Zeeman shifts, and inverting it while setting the detuning to zero. The Zeeman slower captures atoms at velocities up to 950 m/s and slows them down to velocities around 40 m/s in the second stage.

After exiting the Zeeman slower, atoms are captured in a MOT [3]. The magnetic field required for the MOT is generated by two coils in

²Here we introduce a shorter notation, shortening $|F^{(\prime)}, m_{F^{(\prime)}} = m_{F^{(\prime)}}\rangle$ to $|F^{(\prime)}, m_{F^{(\prime)}}\rangle$.



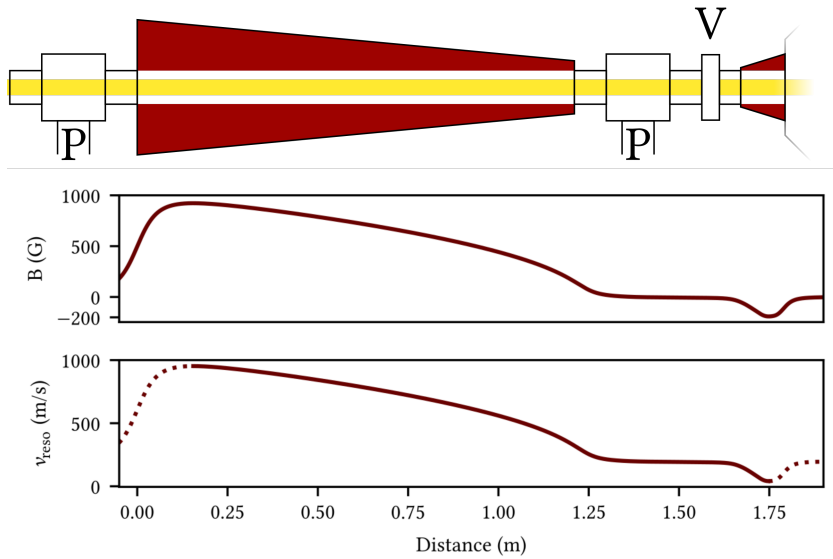


Figure 2.4: Schematic representation of the Zeeman slower. The triangular shaded area indicates where the magnetic coils are located. The middle figure shows the strength of the field generated by the coils. From this the resonant velocity v_{reso} is calculated, shown in the lower figure. The solid line indicates the part of the process in which the resonant velocity is monotonously decreasing, and thus slowing takes place.

anti-Helmholtz configuration. These coils are part of the main coil assembly used for cooling and trapping in the experimental chamber. Details on the design of the coil assembly can be found in Ref. [21]. Additionally, a system of rectangular coils is present around the vacuum chamber to compensate the earth magnetic field, but these coils can also be used to shift the zero-crossing of the magnetic field to effectively move the MOT to a different location. Optically, the beams which will make up the MOT are split on the optical table using a polarizing beam splitter into two different single mode polarization maintaining optical fibers. One fiber provides the beams for the $\hat{x} + \hat{y}$ and $\hat{x} - \hat{y}$ directions, while another provides the beams along the \hat{z} direction. All MOT beams are circularly polarized and detuned approximately -1.5 linewidths from the $|2, 2\rangle$ to $|3', 3'\rangle$ cycling transition. There is an 1 MHz frequency difference between the beams along the \hat{z} direction and the beams along the other two directions to prevent the formation of an optical lattice where the beams cross. All beams are retroreflected, passing through a $\lambda/4$ plate twice to ensure the circular polarization is maintained. A single repump beam is used. This repump beam has its center obstructed and this obstruction is imaged on the location of the MOT in the vacuum chamber. The atoms in the center of the MOT are therefore not repumped. This is a so-called “dark SPOT³” design [22]. Blocking the center of the repump beam prevents losses from light pressure in the center of the MOT, allowing up to a thousand-fold higher density compared to a non-blocked repump beam. We are able to trap approximately 12×10^9 atoms in the MOT at a temperature of 350 μK . Filling the MOT with atoms from the Zeeman slower takes approximately 9 s.

2.2.3 Magnetic confinement

After filling the MOT, atoms are transferred to the magnetic trap (MT). In the MT, atoms are trapped based on their magnetic dipole moment and only atoms in internal states which experience a positive energy shift due to an increasing magnetic field, so-called low-field seekers, can be trapped. This

³Spontaneous-Force Optical Trap



limits magnetic confinement to atoms in the $|1, 1\rangle$, $|2, 1\rangle$ and $|2, 2\rangle$ ground states. Atoms in the $|2, 1\rangle$ state can undergo spin-changing collisions and therefore cannot be trapped for long periods of time. Additionally, atoms in the $|1, -1\rangle$ state have preferable collisional properties over atoms in the $|2, 2\rangle$. So, as many atoms as possible are transferred into the $|1, -1\rangle$ state by means of spin polarization [19]. A short pulse of circularly polarized light is used to transfer atoms in the $|1, 1\rangle$ and $|1, 0\rangle$ states to the $|1, -1\rangle$ state, while the MOT XY beams are turned on to depump any atoms pumped to the $|2, m_F\rangle$ states. As a result, instead of the expected one-third fraction, up to two-thirds of the atoms end up in the $|1, -1\rangle$ state [23]. The magnetic fields used for confinement are generated by the main coil assembly around the experimental chamber, see Ref. [21] for details. The resulting magnetic trap shape is cigar-shaped, with tight confinement along the two radial directions and relatively weak confinement along the axial direction. The MOT coils can be used to move the minimum of the trap or, by changing from an anti-Helmholtz to a Helmholtz configuration, to provide a small additional curvature. To prevent the existence of a magnetic zero crossing, a small set of coils provides a bias field putting the minimum field strength of the trapping field at approximately 5 Gauss. The chosen coil configuration would normally provide a linear confinement in the radial direction ($V(r) \propto |r|$) but due to the bias field the radial confinement is linear at large distances and approximately quadratic at small distances. As a result the trap is effectively linear at high temperatures and quadratic at low temperatures. The cross-over between the linear and quadratic regime is found at a temperature of approximately $10 \mu\text{K}$ [24]. The axial potential is quadratic over the entire range. Approximately 6×10^9 atoms are transferred to the magnetic trap under typical experimental conditions, with a final temperature of $350 \mu\text{K}$. The trapping frequencies attainable in the magnetic trap are $\omega_r = 2\pi \times (30 - 100) \text{ Hz}$ and $\omega_z = 2\pi \times (1.2 - 16) \text{ Hz}$.

2.2.4 Evaporative cooling

To further cool the atoms after transfer to the magnetic trap, evaporative cooling is used. In this process, the hottest atoms are continuously removed from the trap and while the atoms in the cloud rethermalize through collisions. The threshold energy for removal is gradually lowered as the atom cloud cools down. Every atom removed carries away 6–10 times the average energy of an atom in the cloud. Removal of atoms is done by inducing a transition from the trapped $|1, -1\rangle$ to the untrapped $|1, 0\rangle$ state using a radiofrequency (RF) field with a frequency between 3 and 60 MHz. Atoms are selected by tuning the RF frequency. Atoms in different locations in the potential will experience a different Zeeman shift. By starting the RF ramp at a high frequency those atoms are selected which reach only the highest potential energies, *i.e.* the hottest atoms. Lowering the RF frequency gradually reduces the energy at which atoms are expelled. The entire cooling process takes approximately 80 s. Cooling typically takes place in a maximally compressed trap, as this increases the collision rate and thus increases cooling efficiency and reduces cooling time. Bose-Einstein condensation can be reached in several ways: by cooling the cloud through the transition temperature using evaporative cooling, either in a maximally compressed trap or in a decompressed trap, or by transferring atoms to an optical trap and completing the cooling process in the optical trap. In a maximally compressed trap, a Bose-Einstein condensate of approximately 30×10^6 atoms is created. Typically, less strict confinement will lead to lower particle numbers in the BEC as evaporative cooling is less efficient and the critical temperature in a decompressed traps is lower. A detailed description of the optical trap can be found in Ref. [25].

2.2.5 Imaging

Whether an experiment is running to acquire data for a paper, or just to optimize particle number, the atoms need to be imaged. The proven and standard technique to do this is on-resonance absorption imaging



[4]. In on-resonance absorption imaging, the atoms are released from the trap to decrease the (optical) density at the moment of probing. After the pre-determined time of flight, the atom cloud is illuminated with a Gaussian beam many times larger than the size of the atom cloud, so that locally at the position of the atoms the intensity profile is approximately flat. The exact time of flight is determined by considering the expected density. If the time of flight is chosen to be too short, the sample will be completely opaque, but when it is chosen to be too long, the signal-to-noise will be low. The atoms in the cloud will absorb light proportionally to the local density after expansion. The shadow observed in transmission is therefore a quantitative measure of the density integrated along the path of the light. As the resonant light is absorbed during imaging, atoms are lost from the condensate due to heating and scattering into untrapped states. Thus absorption imaging is a destructive imaging method. When studying dynamics a destructive imaging method is very unpractical as the evolution of a single sample can not be followed. Non-destructive imaging can be performed by tuning the laser away from the resonance. When the probe beam is detuned many linewidths away from the resonance, the absorption of light is negligible but the phase delay induced by the atoms can still be measured. The phase of a light field can be measured using an interferometric technique, for which a reference beam is overlapped on the camera with the signal beam. The phase is determined from the interference of both beams. In Utrecht, previously, phase-contrast imaging was used to perform non-destructive imaging of atoms, the details of which can be found in Ref. [26]. As part of this work an off-axis holography method to image atoms has been developed and implemented. This imaging method provides several improvements over phase-contrast imaging. The details of this holographic imaging method can be found in Chapter 3. Typically, absorption imaging is used to perform diagnostic measurements such as optimizing particle number when aligning lasers since non-destructive methods don't provide the necessary (phase) contrast for clouds above the critical temperature for BEC. Non-destructive imaging methods are used to obtain all the data in the following chapters of this dissertation. A schematic representation of the imaging setup can be found in Chapter 3, in

Fig. 3.1.

2.3 Experimental control

In the previous section I described the physical processes required to make a Bose-Einstein condensate. However, it does not list the technical challenges involved in controlling the devices needed to perform the described processes. The entire experimental sequence requires precise timing on different time scales. The cooling sequence takes 80 seconds, but for imaging pulses only a few microseconds are required. Experimental control can roughly be divided in three categories; digital channels, which are on or off, analog channels, which can attain a value between two voltages, and miscellaneous channels such as those controlling or reading out cameras and function generators, which need dedicated features integrated into the software.

2.3.1 Control software

The heart of our control software is the *Cicero WordGenerator* developed at MIT by Aviv Keshet [27]. It simplifies the complicated task of controlling the setup by cutting the entire sequence up into timesteps of a certain duration. For each timestep one selects which digital channels are turned on or off. Analog channels are controlled by analog groups, which contain a set of waveforms for each analog channel. At the beginning of each timestep an analog group can be started, changing the output of the active analog channels to the values specified by the waveforms in that analog group. While timesteps are the main way the status of a digital channel is controlled, *Pulses* provide a way to deviate from this. Sometimes it is desirable to toggle a channel on or off shortly before the next step begins. A *Pulse* allows one to take an action a certain amount of time before or after the start or end of a timestep, overriding the status of a digital channel in the timestep and setting it to a certain value. This is extremely useful for devices which have to be pre-triggered, such as cameras.



Since it is desired for all data of an experimental sequence to be stored in the same sequence file, all miscellaneous devices were integrated into the *WordGenerator* software. To integrate the camera, the *WordGenerator* is expanded with an interface which contains all features of the camera. This way, settings for the camera are stored in the *WordGenerator* data files. For the evaporative cooling a direct digital synthesizer (DDS) is used with a serial interface. Controlling the DDS directly over *RS232* during the experiment leads to inaccurate timings and is taxing on the control hardware. To solve these problems a stand-alone device has been realised. This stand-alone device stores up to eight RF curves which are loaded into the device before the start of a run over a serial connection. The interface used for entering waveforms already present in the *WordGenerator* is extended to input the evaporation curves. In principle, an infinite number of waveforms can be added to a sequence. At the start of each run, up to 8 waveforms are loaded as RF curves into the device. For RF curves that do not change from run to run, the software keeps a hash⁴ such that the curves are only loaded to the device when they have changed.

To spread the load of experiment control, three computer systems are used in controlling the experiment. The *WordGenerator* supports splitting the user interface and actual server controlling the hardware, such that the computer receiving the user input and performing auxiliary tasks is partly decoupled from the actual computer controlling the experiment. The communication between the client (*Cicero*) and server (*Atticus*) uses a proprietary *.NET* protocol which allows over-network sharing of the complete settings and sequence data. All user input is given on the client computer. At the start of each run, the client will send a message to both servers. The *Atticus* server will take the timestep data from the client system and generate buffers to be used with the output cards. When the buffer generation is finished, the RF curves are loaded, and the camera is ready for acquisition. The run is started. A pre-programmed FPGA⁵ generates a variable clock signal, to ensure precise timing on both long and

⁴The entire RF sequence is turned into a string, of which the *MD5* hash is calculated and stored.

⁵Opal Kelly XEM3001

short time-scales. At the end of the run, the status of the buffers is read out to confirm that the correct number of clock pulses has been received by every output card. If the camera also reports a successful acquisition, the run is deemed successful and all files are saved.

To control the camera⁶ a separate server is written in *C++*. As a single run can generate gigabytes of data the choice was made to have a dedicated computer for controlling the camera. Communication between the *WordGenerator* and camera server follows a simple plain-text TCP/IP protocol. The camera settings can be set directly from the *WordGenerator* client at any time when no data are being acquired. At the start of each run, the camera server is primed with a message listing the number of images taken in the run. The camera server will confirm being ready, then await triggers. After receiving all triggers the data are saved in *FITS* format by the camera server.

2.3.2 Control hardware*

To output signals we make use of *National Instruments* digital and analog output cards. For the digital signals, two 32-channel *PCIe-6612* are used, for a total of 64 digital channels. Both cards are connected to a breakout box. Twenty channels are reserved to control the stand-alone DDS and the power supplies of the magnetic coils. Thus 44 digital channels are freely available. For signals needed near the control system, such as those used to control the magnetic coils and Zeeman slower, the control cards are galvanically isolated from the rest of the signal path, but no special measures are taken to ensure signal integrity. However, signals are needed at different locations in the lab and long coaxial cables can suffer from delays and signal distortion due to reflection. For signals travelling to the optical tables, up to 12 metres from the control system, on top of galvanic isolation, additional measure have to be taken to prevent signal integrity. Forty of the digital signals are grouped in five groups of eight channels and fed through a pair of differential line

⁶Andor Zyla 5.5-USB3

*This subsection is based on work done by F. Ditewig and D. Killian, see [28].



drivers⁷. Using a shielded 25-channel cable, the signal is relayed to anywhere in the lab. At the receiver, a differential line receiver⁸ converts the signal back to a TTL signal, which is output through BNC connectors. The receiver obtains power from the same 25-channel cable that provide the signal, such that no external power source is required. This allows us to have flexible access to control signals everywhere in the lab. This system is completely modular and a spare driver and receiver module are present, to minimize downtime in the event of failure of a module.

For the analog signals, two 8-channel *PCI-6713* analog output cards with 14-bit Digital-to-Analog converters (DACs) are used. Of these 16 channels, eight channels are reserved for controlling current through the main magnetic coils (5) and the compensation cage (3) around the main coils. The eight channels reserved for the coils are not galvanically isolated at the output of the control module, but galvanic isolation is present in the control modules at the end of the signal line. The remaining eight analog channels are immediately led through an isolating amplifier. The isolating amplifier both protects the output cards and enables one to change the output voltage. While the output cards output between -10 V and +10 V, some devices require a voltage between 0 and 5 V, or perhaps even 0 and 1 V, and will lose resolution if a 1:1 conversion in the isolating amplifier is used. The isolating amplifier can be modified to output voltages between 0 and 5 V (or 1 V) with the same 14-bit resolution available for the full -10 to +10 V range. No special care is taken with extra-long cables. The capacity of a coaxial cable of some length can be significant, and for fast-changing signals special care has to be taken to ensure signal fidelity on a case-to-case basis.

The FPGA generating the variable clock signal is mounted in the digital signal breakout box. The clock signal is connected to one of the two digital output cards and subsequently transmitted to the other 3 control cards using a ribbon cable. Programming the FPGA and loading the variable clock signal for each cycle is done over a USB-3 connection, connected to the *Atticus* server.

⁷AM26C31

⁸AM26C32

The stand-alone RF cabinet, containing the DDS and the microcontroller, used for evaporative cooling is connected through a USB-to-Serial connector to the *Atticus* server to load the different RF curves. Five of the reserved digital channels are also connected to the RF cabinet, such that during the experimental run rapid communication between the main experimental control and the microcontroller is possible. Three channels are reserved for picking the waveform, one channel triggers the start of outputting a RF signal and one channel functions as a switch, which has to be high as long as output is desired from the RF cabinet.

2.4 Data management*

Running the experiment is only part of the work of actually acquiring data for a publication. After a succesful run, it is imperative that the data are stored in a way that allows a scientist to find the data files for analysis months or even years after the data are acquired. To this end, data in our experiment are stored by date, and measurements on a single date are numbered incrementally. This allows one to easily keep track of measurements in a lab journal, and since measurements are assigned consecutive numbers. Ideally, all data and metadata are stored in one place, in a queryable database with keywords to quickly find measurements of a certain category. However, we have not yet reached this utopia of data management. For quick searches through measurements a lab journal, digitized or not, remains a vital tool.

The main results of an experimental run are the images acquired by the camera. However, to interpret this data, metadata such as the settings for each run are required. To this end, the *Cicero* server stores the executed

*Some information in this section has previously been published as part of the data management article *Van Labboek naar cloudservice* in the *Nederlands Tijdschrift voor Natuurkunde*, edition 11, 2019. [29]



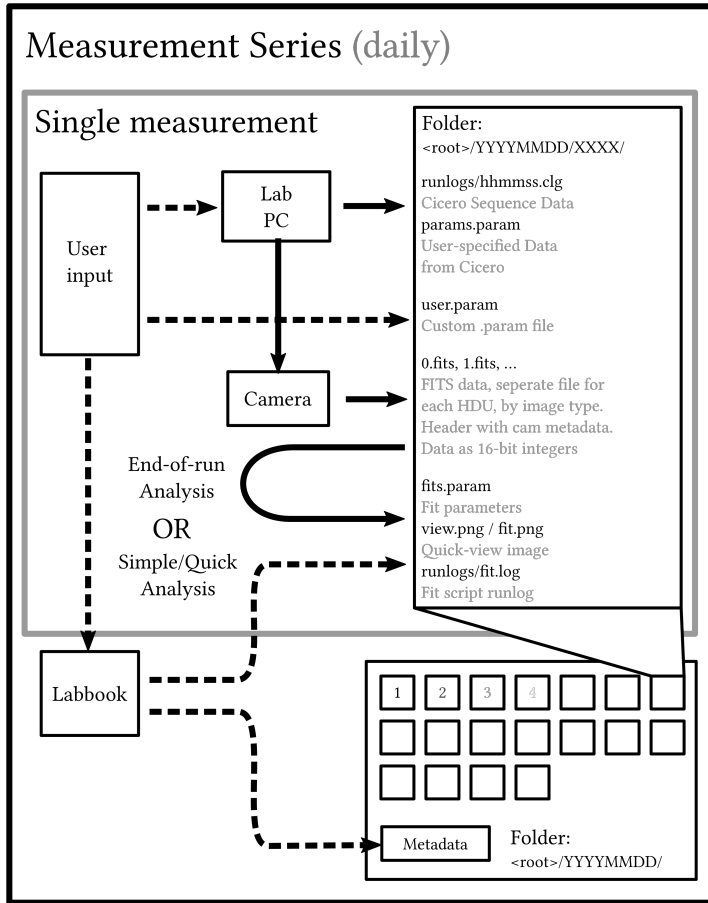


Figure 2.5: Data flow from measurement to storage. Solid lines represent automated processes. Dashed lines indicate user input. All data and metadata are gathered, including preliminary analyses and stored in a single folder. Data from a single date can be merged with metadata from the lab journal into a single unit.

sequence with each succesful run, and in addition provides an easily interpretable file with parameters which often changes from run to run, such as time of flight. The files from the *Cicero* server are gathered on the camera server. For each date a separate folder is created and within this folder, a folder for each measurement run on this date. For each measurement, all logs and preliminary analyses are stored in this folder, such that raw data, metadata, and preliminary analysis results are all easily accessible and clearly associated with a single measurement. Figure 2.5 provides a schematic representation of data flow from acquisition to local storage.

For scientific data management and storage, Utrecht University has developed *Yoda* [30], based on open source data management software *iRODS* developed by the iRODS consortium [31], of which several universities in the Netherlands including Utrecht University are members. *Yoda* serves as a data management and archiving system, storing data on servers located in at least two datacenters to ensure persistence. A group of users (“research group”) has access to the data, either as read-only user or as “full” user. Data in *Yoda* can be locked and unlocked to prevent accidental changes to the data. Data sets can also be vaulted, in which case a data set is made read-only. Vaulted data can be given a Digital Object Identifier (DOI) and can be published. Transferring files to *Yoda* is easy: it can be mounted as a drive in the filesystem. For bigger files, a set of command-line utilities named *iCommands* are recommended.

In our lab, the last three days of data folders are checked for changes every five minutes and new or changed files are uploaded to the online storage. This process is automated using *iCommands*. All data from a specific date is automatically locked four days after acquisition, as after this time no more preliminary analysis is expected to be done. Data are shared between all group members on different platforms, with bachelor and master students typically having read-only access and others having full access. Data analysis is typically done locally and raw data, results and manuscripts are bundled and vaulted. Sadly, for publications associated with this dissertation no complete vault is available, as this way of data management was developed and slowly implemented over the two years



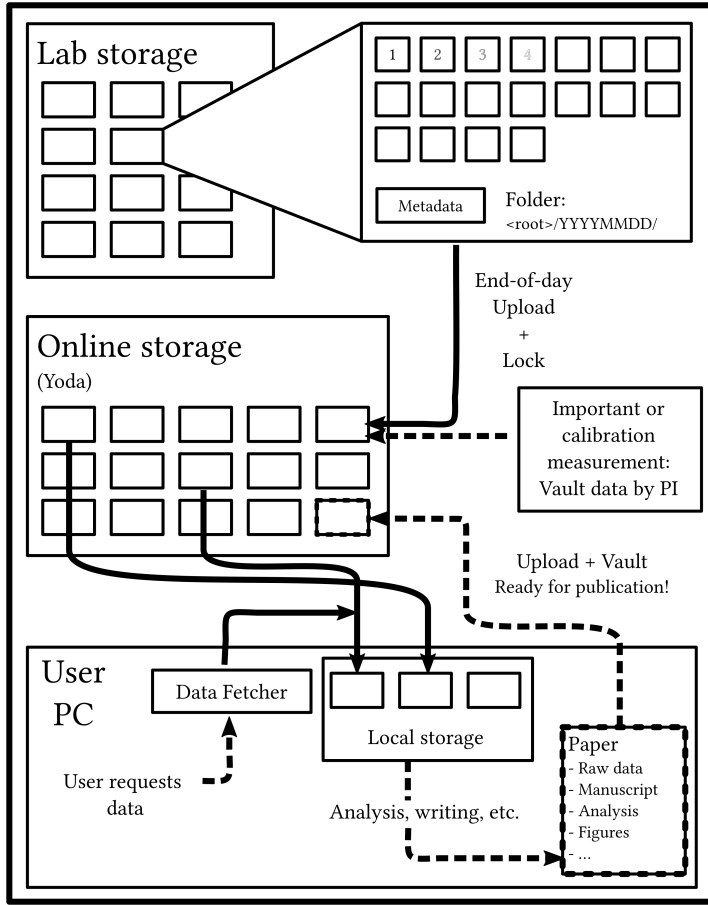


Figure 2.6: Data flow from lab storage, to online storage, to publication. Solid lines represent automated processes. Dashed lines represent user input. Each day data are uploaded from the lab storage to the *Yoda* online database. Folders on the online database are locked to prevent accidental data corruption. Users can download files to work on locally. When working on a publication, all raw data, analysis scripts, processed data and even the \TeX files can be bundled into a single unit, which is vaulted to ensure data integrity. Important raw data can also be vaulted immediately to ensure data integrity.

prior to the publication of this work. Fig. 2.6 provides an overview of the data flow from local storage to online storage, and how this data can be used by different users and in the end published as a vault.



References

- [1] W. D. Phillips and H. Metcalf, *Phys. Rev. Lett.* **48**, 596 (1982).
- [2] S. Chu, L. Hollberg, J. E. Bjorkholm, A. Cable, and A. Ashkin, *Phys. Rev. Lett.* **55**, 48 (1985).
- [3] E. L. Raab, M. Prentiss, A. Cable, S. Chu, and D. E. Pritchard, *Phys. Rev. Lett.* **59**, 2631 (1987).
- [4] W. Ketterle, D. S. Durfee, and D. Stamper-Kurn, arXiv preprint cond-mat/9904034 (1999).
- [5] M. M. Markowitz, *Journal of Chemical Education* **40**, 633 (1963).
- [6] P. A. Ruprecht, M. J. Holland, K. Burnett, and M. Edwards, *Phys. Rev. A* **51**, 4704 (1995).
- [7] E. A. Donley, N. R. Claussen, S. L. Cornish, J. L. Roberts, E. A. Cornell, and C. E. Wieman, *Nature* **412**, 295 (2001).
- [8] E. W. Streed, A. P. Chikkatur, T. L. Gustavson, M. Boyd, Y. Torii, D. Schneble, G. K. Campbell, D. E. Pritchard, and W. Ketterle, *Review of Scientific Instruments* **77**, 023106 (2006).
- [9] E. Arimondo, M. Inguscio, and P. Violino, *Rev. Mod. Phys.* **49**, 31 (1977).
- [10] W. Yei, A. Sieradzan, and M. D. Havey, *Phys. Rev. A* **48**, 1909 (1993).
- [11] D. A. Steck, *Sodium D Line Data*, 2000.
- [12] R. C. Weast, *Handbook of Chemistry and Physics, 49th Edition*, 1968.
- [13] C. Samuelis, E. Tiesinga, T. Laue, M. Elbs, H. Knöckel, and E. Tiemann, *Phys. Rev. A* **63**, 012710 (2000).
- [14] P. Juncar, J. Pinard, J. Hamon, and A. Chartier, *Metrologia* **17**, 77 (1981).
- [15] C. W. Oates, K. R. Vogel, and J. L. Hall, *Phys. Rev. Lett.* **76**, 2866 (1996).
- [16] U. Volz, M. Majerus, H. Liebel, A. Schmitt, and H. Schmoranzner, *Phys. Rev. Lett.* **76**, 2862 (1996).
- [17] J. Smits, *Phase imprinting of vortices in Bose-Einstein condensates using shaped light*, 2016.

- [18] M. S. Feld and V. S. Letokhov, *Scientific American* **229**, 69 (1973).
- [19] K. M. R. van der Stam, E. D. van Ooijen, R. Meppelink, J. M. Vogels, and P. van der Straten, *Review of Scientific Instruments* **78**, 013102 (2007).
- [20] W. D. Phillips and H. Metcalf, *Phys. Rev. Lett.* **48**, 596 (1982).
- [21] E. D. van Ooijen, “Realization and Illumination of Bose-condensed Sodium Atoms”, PhD thesis (Utrecht University, 2005).
- [22] W. Ketterle, K. B. Davis, M. A. Joffe, A. Martin, and D. E. Pritchard, *Phys. Rev. Lett.* **70**, 2253 (1993).
- [23] K. M. R. van der Stam, “Superradiant scattering of laser light from a Bose-Einstein condensate”, PhD thesis (Utrecht University, 2006).
- [24] C. Beulenkamp, “Evaporative Cooling in a Bose Gas”, BSc thesis (Utrecht University, 2017).
- [25] A. Groot, “Excitations in hydrodynamic ultra-cold Bose gases”, PhD thesis (Utrecht University, 2015).
- [26] R. Meppelink, R. A. Rozendaal, S. B. Koller, J. M. Vogels, and P. van der Straten, *Phys. Rev. A* **81**, 053632 (2010).
- [27] A. Keshet and W. Ketterle, *Review of Scientific Instruments* **84**, 015105 (2013).
- [28] There is no published work available on the hardware system. However, technical documentation on this system is stored digitally and should be available upon request at the current technician of the Nanophotonics research group in Utrecht, at the time of writing Dante Killian or Aron Opheij. The main project identifier is BECCTRL2, with the overview found in file F1201c.
- [29] J. Smits and D. van Oosten, *Nederlands Tijdschrift voor Natuurkunde* **85**, 18 (2019).
- [30] Yoda on *Utrecht University website*, <https://www.uu.nl/en/research/yoda>, Accessed on 2020-11-17.
- [31] iRODS *consortium website*, <https://irods.org/>, Accessed on 2020-11-17.

3 Imaging trapped quantum gases by off-axis holography

In this Chapter we present a dispersive imaging method for trapped quantum gases based on digital off-axis holography. Both phase delay and intensity of the probe field are determined from the same image. Due to the heterodyne gain inherent to the holographic method it is possible to retrieve the phase delay induced by the atoms at probe beam doses two orders of magnitude lower than phase-contrast imaging methods. Using the full field of the probe beam we numerically correct for image defocusing.



WHEN studying the dynamics of trapped quantum gases, it is desirable to have a method of imaging that perturbs the atom cloud as little as possible, which makes it possible to perform a study on atom cloud dynamics on a single sample. Due to the extremely low temperatures of quantum gases any photon absorption event induces significant atom losses, which influences the outcome of a sequence of measurements. To reduce scattering the frequency of the light can be detuned from the atomic transition, but this in turn reduces the refractive index contrast. This makes that a quantum gas has at the same time very low refractive index contrast and can endure very little probe light. In this Chapter we present a dispersive imaging method for quantum degenerate

This chapter is based on *Imaging trapped quantum gases by off-axis holography*, J. Smits, A. P. Mosk, and P. van der Straten, **Optics Letters** 45, 981-984 (2020) [1] (© 2020 Optical Society of America).



atom clouds based on off-axis holography [2–5]. In addition to the probe beam, a reference beam is used which interferes with the probe beam. From the interference pattern between the two beams, the full field of the probe beam is reconstructed. Use of an external reference beam enables imaging at the probe beam shot noise level for any intensity. As atom losses are directly related to the dose of a light pulse, reducing the intensity or pulse time of the probe beam reduces the atom losses allowing for longer interrogation time of the same sample. Moreover, as the recorded hologram contains both absorption and phase delay resulting from interaction with the atoms, both can be studied independently. Since the full field of the probe beam is known, it is possible to use numerical refocusing [6] to correct for defocusing in the experiment using data post-processing.

Many different imaging methods have been developed [7–17] to image quantum gases at minimum losses, most notably partial-transfer absorption imaging [7] and several dispersive methods such as phase-contrast imaging [8–10], intensity-based defocus-contrast imaging [11, 12], and more recently dark-field Faraday rotation imaging [13] and shadowgraph imaging [14]. However, these dispersive methods lack the heterodyne gain present in a method based on off-axis holography leading to increased noise at lower probe doses. Holographic imaging methods have been demonstrated on atoms trapped in a magneto-optical trap [16, 17]. Here we apply the method to degenerate Bose gasses, which are far more sensitive to the scattering of photons due to their intrinsic lower temperatures. The method presented here is non-iterative as opposed to Ref. [16] and thus allows for an instantaneous retrieval of both phase and amplitude. Furthermore, it retrieves both phase and amplitude as opposed to Ref. [17], which are subsequently utilized for refocusing to obtain optimal image quality.

In quantum gases the refractive index is proportional to the density [18]. By changing the detuning δ from the atomic resonance a quantum gas can be made mostly an absorber ($\delta \approx 0$, on resonance) or mostly a phase-object ($|\delta| \gg \gamma$, many atomic linewidths γ detuned). The imaginary part of the refractive index, responsible for absorption, scales as $\Im(\mathcal{N}) \propto 1/\delta^2$ for large detuning δ . The real part, responsible for the phase shift, scales as $\Re(\mathcal{N}) \propto$

$1/\delta$. Increasing the detuning from resonance reduces atom losses, at the cost of signal strength. In this work, experiments are performed at $\delta = -350$ MHz or approximately 36 atomic linewidths from the resonance. At typical peak densities in these experiments, the refractive index contrast is $\Re(\mathcal{N}) - 1 \approx 2 \times 10^{-3}$.

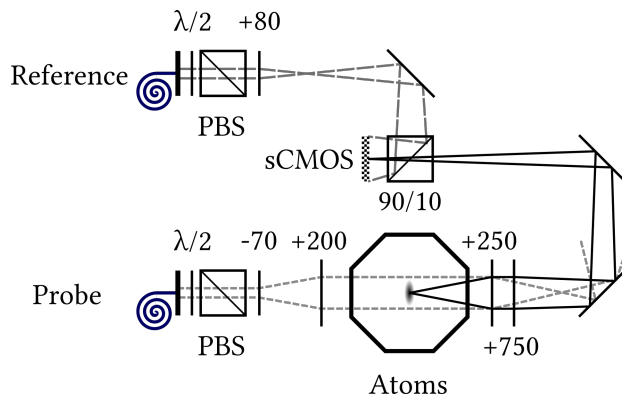


Figure 3.1: Schematic representation of the setup. The focal distance of lenses is given in millimetres. The octagon represents the vacuum chamber and is approximately 50 cm across. After each fiber there is a half-wave plate, denoted by $\lambda/2$, and a polarizing beam splitter, denoted by PBS, to ensure the polarization of the light. The label sCMOS denotes the camera.

The imaging is performed on a Bose-condensed gas of Na atoms. The atoms are trapped in a cylindrically-symmetric magnetic trap with effective trapping frequencies $(\omega_\rho, \omega_z) = 2\pi \times (60.0, 15.0)$ Hz and are cooled to below the critical temperature for Bose-Einstein condensation by means of evaporative cooling, reaching temperatures between 400 and 600 nK with approximately $N = 5 \times 10^7$ particles. The atoms are illuminated by a locally flat beam and are imaged on the camera (see Fig. 3.1). To be able to perform off-axis holography, the probe light is split on a separate optical table and both probe and reference beam are transported to the experimental setup by polarization maintaining fibers. The reference beam is matched in divergence to the unscattered probe light to cancel the relative curvature between the wavefronts of probe and

reference beam. The angle between the probe and reference beam on the camera is a few degrees. The large size of the vacuum chamber limits the numerical aperture using optics with a 50-mm diameter to $NA = 0.1$. Due to the use of two separate fibers to transport reference and probe beam a global phase shift will be present for each image, which is removed in post-processing by setting the part of the image where no atoms are present to zero accumulated phase. The coherence length of the probe laser is in the order of 100 m owing to the 1 MHz laser linewidth. Since probe illumination time of individual images are in the order of 10 – 100 μs , no special precautions are taken to ensure stability from vibrations, as the probe pulse is generally shorter than the time scales of vibrations in the setup. Since a typical cold atoms laboratory has lasers operating at sub-MHz laser linewidth, adding a reference beam on the camera at a small angle with respect to the probe beam is all that is needed to convert an existing imaging system for absorption or phase-contrast imaging to use this holographic method.

The resulting image on the camera is an interference pattern between probe and reference beam,

$$I \propto \left| E_{\text{ref}} e^{i\mathbf{k}_{\text{ref}} \cdot \mathbf{r}} + E_{\text{probe}} e^{i\mathbf{k}_{\text{probe}} \cdot \mathbf{r}} \right|^2 = |E_{\text{ref}}|^2 + |E_{\text{probe}}|^2 + E_{\text{ref}}^* E_{\text{probe}} e^{i\tilde{\mathbf{k}} \cdot \mathbf{r}} + E_{\text{ref}} E_{\text{probe}}^* e^{-i\tilde{\mathbf{k}} \cdot \mathbf{r}}, \quad (3.1)$$

where $\mathbf{r} = (x, z)$ and $\tilde{\mathbf{k}} = \mathbf{k}_{\text{probe}} - \mathbf{k}_{\text{ref}}$ is the difference wavevector of the incoming fields, which is determined by the angle θ_x, θ_z between the reference and probe beam, and given by $\tilde{\mathbf{k}} = k_0(\sin \theta_x, \sin \theta_z)$, where k_0 is the laser wavenumber. A cutout of such an intensity profile, centered on the atom cloud, is shown in Fig. 3.2a. The Fourier transform of the intensity pattern contains well-defined peaks associated with the interference pattern. To prevent artefacts in the fast Fourier transform due to boundary effects, a square Tukey window with width $\alpha = 0.1$ is applied prior to applying the Fourier transform. The result of the Fourier transform is shown in Fig. 3.2b. Focussing on one of the interference terms in Eq. 3.1, the Fourier transform is given by

$$\mathcal{F}(E_{\text{ref}}^* E_{\text{probe}} e^{i\tilde{\mathbf{k}} \cdot \mathbf{r}})(\mathbf{k}) = \mathcal{F}(E_{\text{ref}}^* E_{\text{probe}})(\mathbf{k} - \tilde{\mathbf{k}}). \quad (3.2)$$

Essentially, the interference term in the Fourier transform contains the information of the product of the fields translated from the origin. By taking an appropriate cutout in Fourier space, the information of the product of these fields can be isolated. In this case, an elliptical window (Tukey, $\alpha = 0.1$) is chosen, resulting in numerical apertures $\text{NA}_x = 0.064$ and $\text{NA}_z = 0.040$ (see Fig. 3.2b). This reduction in numerical aperture compared to the physical limit can be overcome by using multiple pixels per resolution element, but this oversampling is not possible in our setup due to space limitations.

An elliptical window is chosen as the elongated shape of the atom cloud will have a larger extent in Fourier space in its short (x) direction, while being relatively compact in Fourier space in the long (z) direction. This yields the most accurate image of the atom cloud at rest, but the choice of window shape should be considered based on the type of experiment that is performed. The inverse Fourier transform of the cutout yields the product of the fields of the probe and reference beam. The reference beam is sufficiently flat, such that the result is the field of the probe beam, scaled by the magnitude of the field of the reference beam. By applying an inverse Fourier transform to the cutout, the full field (both amplitude and phase) of the probe beam can be retrieved. For normalization, a second recording without atoms is made afterwards to calculate the normalized field of the probe beam,

$$\tilde{E} = \frac{E_{\text{ref}}^* E_{\text{probe}}}{E_{\text{ref}}^* E_{\text{empty}}} \equiv e^{-\phi'' - i\phi'}, \quad (3.3)$$

where ϕ' is the phase delay of the probe beam accumulated as it passes through the atom cloud, and $2\phi''$ is the optical density. The argument of \tilde{E} is directly proportional to the phase delay, as opposed to phase contrast imaging or shadowgraph imaging methods in which the phase is reconstructed from the intensity profile, which makes these methods more susceptible to noise. The phase delay is shown in Fig. 3.2c. The Bose-Einstein condensate is seen as a dense core in a diffuse thermal cloud. The optical density is extracted from the field amplitude and is shown in Fig. 3.2d. Here the signal from the thermal cloud is too weak to be observed, but the Bose-Einstein condensate is clearly visible. This signal is very



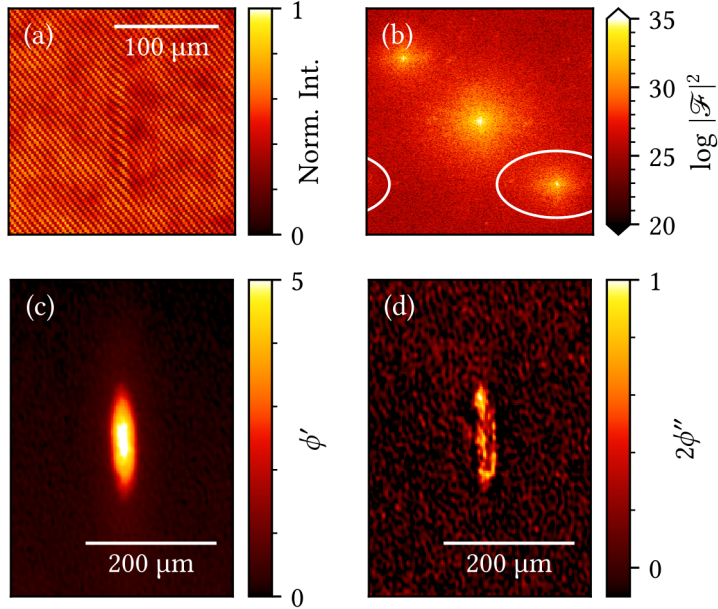


Figure 3.2: From hologram to phase and optical density. Image at a probe power of $88 \mu\text{W}/\text{cm}^2$ and an illumination time of $100 \mu\text{s}$. (a) Cut-out of the interference pattern as recorded by the camera, centered on the atom cloud. Note that the fringes are curved due to the extra accumulated phase. (b) Fourier space before the cut and translation. The cut-out is indicated by the white ellipse. (c) Accumulated phase extracted from the inverse Fourier transform, centered on the atom cloud. (d) Optical density extracted from the inverse Fourier transform centered on the atom cloud.

dependent on the chosen focal plane. The absence of signal for the thermal cloud in this image is due to the much lower density in the thermal cloud. To determine the density distribution in the atom cloud for $|\delta| \gg \gamma$, it is sufficient to consider only the accumulated phase.

For minimally destructive imaging the dose of the probe beam is chosen as low as possible, while preserving a sufficiently low noise level for analysis of the resulting image. Since the reference beam can be chosen arbitrarily intense for increased heterodyne gain [17], off-axis holography allows shot-noise limited imaging down to the single-count-per-pixel level in the reference beam [19]. In Fig. 3.3 we demonstrate the effect of reduced probe power and duration on the image quality. Figure 3.3a approximately corresponds to typical probe power and duration used in phase-contrast imaging in earlier experiments [20], which is an irradiated dose of approximately 1700 photons/px. At lower probe power we observe an acceptable increase in noise down to an irradiated dose of 9 photons/px. At an irradiated dose of 5 photons/px the reconstructed field contains phase vortices, as can be seen in the cut-through in Figs. 3.3e and 3.3f. These spurious vortices can be attributed to a reduction in fringe contrast and decrease the signal-to-noise ratio in the reconstructed phase. A slice through each cloud along its long axis is shown in Fig. 3.3f. The SNR determined from the data follows the square-root dependence on the number of photons per pixel, as derived in Ref. [17].

To study the effect of defocusing on the quality of the image, a slice of the field is taken through the radial direction of the condensate. Since the full field is known, the Beam Propagation Method (BPM) [21, 22] in free space can be used. With the BPM the field is calculated at different planes, such that to propagate the field from a plane at y to a plane at y' one calculates

$$\tilde{E}(x, y') = \mathcal{F}_x^{-1} \left\{ e^{-ik^2(y'-y)/(2k_0)} \times \mathcal{F}_x[\tilde{E}(x, y)](k) \right\} (x). \quad (3.4)$$

For comparison, light propagation through a Bose-Einstein condensate is calculated using the BPM and a time-splitting spectral method [23]. In the calculation, a cut is made in Fourier space to simulate $\text{NA}_x = 0.064$, as in the experiment. The results of propagating the experimental results and the



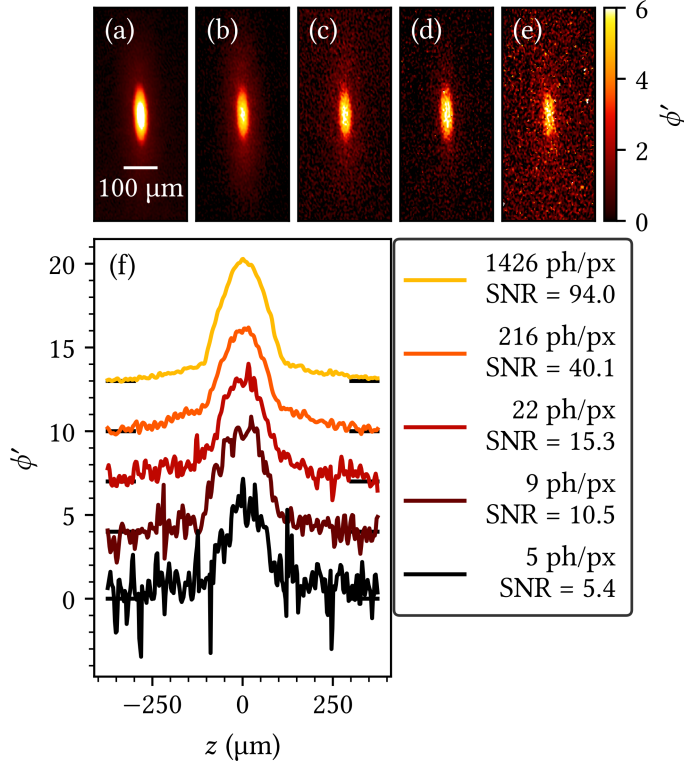


Figure 3.3: Advantages of heterodyne gain in determining accumulated phase. All doses in irradiated photons per pixel. (a-e) Degenerate atom clouds imaged at different photon doses at similar atom numbers in the atomic cloud. The ratio between reference and probe beam intensity is $\sim 14\times$ for (a,b) and $\sim 64\times$ for (c-e). (a) Pulse time of $\tau = 100 \mu\text{s}$ at intensity $I = 69 \mu\text{W}/\text{cm}^2$, corresponding to 1426 photons/px. (b) $\tau = 50 \mu\text{s}$, $I = 21 \mu\text{W}/\text{cm}^2$, 216 photons/px. (c) $\tau = 25 \mu\text{s}$, $I = 4 \mu\text{W}/\text{cm}^2$, 22 photons/px. (d) $\tau = 10 \mu\text{s}$, $I = 4 \mu\text{W}/\text{cm}^2$, 9 photons/px. (e) $\tau = 5 \mu\text{s}$, $I = 4 \mu\text{W}/\text{cm}^2$, corresponding to 5 photons/px. (f) Slice through a single row of pixels in the center of the cloud for figures (a-e). The black horizontal lines indicate the zero level for the different lines. The signal-to-noise ratio (SNR) is calculated by dividing the peak signal by the RMS deviation in an empty part of the image.

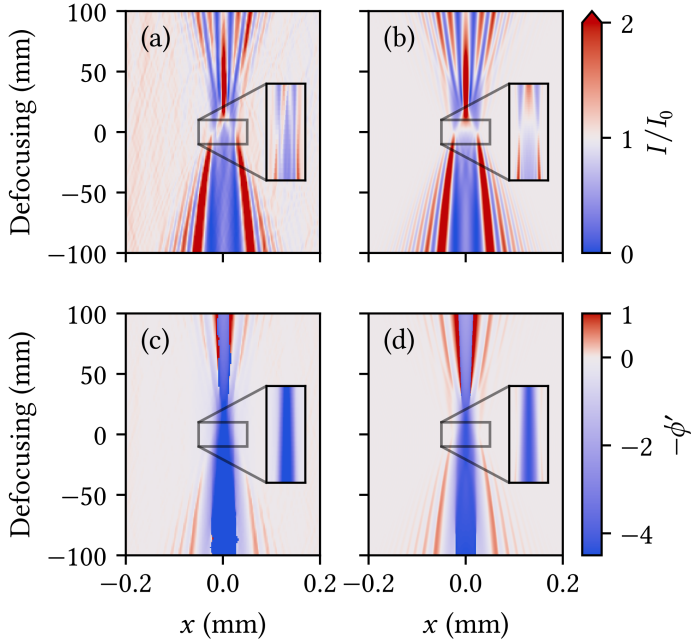


Figure 3.4: Effect of defocusing on phase and amplitude. Cross-section through the center of the atomic cloud in the radial direction. The total span of the inset is 1 cm. (a) Effect of numerical defocusing on the intensity in a typical experiment. (b) Comparison of (a) to a numerical model. (c) Effect of numerical defocusing on the phase in a typical experiment. (d) Comparison of (c) to a numerical model.

comparison to theory are shown in Fig. 3.4. The intensity varies strongly at slight defocusing due to cross-talk between phase and amplitude. This can be attributed to the lensing properties of the Bose-Einstein condensate: Light passing through the atom cloud is refracted, causing strong dependence on the chosen image plane. The phase is more robust against defocusing yielding an interpretable signal even at slight misalignment of the focus, but defocusing will change the perceived dimensions of the cloud.

The information from Fig. 3.4 can be used to accurately position the image plane in the same plane as the atom cloud. However, as the full field is measured, it is also possible to numerically propagate the image plane to the plane that contains the atoms, using Eq. 3.4 in 2D. To demonstrate this process of numerical refocusing, atom clouds are recorded with intentional defocusing by moving one of the imaging lenses in the setup. In Fig. 3.5 the result of this measurement is shown. The red boxes around frames (a), (e) and (i) indicate the actual images recorded in the experiment. Each row corresponds to a single measurement run and columns indicate different image planes, using data which is obtained by numerical propagation. For comparison, the BPM and a time-splitting spectral method has been used to calculate the expected intensity and phase for the parameters in Fig. 3.5e at each image plane with a window function to attain the same numerical aperture as in the experiment. When the atom cloud is not in focus, a clear diffraction pattern is observed. Numerical refocusing of out-of-focus images reproduces both the thermal cloud and the Bose-Einstein condensate very accurately. Propagating to the image planes for the other two experiments yields similar diffraction patterns. This demonstrates that in our method the choice of image plane is irrelevant, since both phase and amplitude of the probe beam are known. In addition, in the case that more than one atom cloud is present, both can be imaged in a single shot, and then individually brought into focus numerically. Moreover, this method allows for correction of coma and spherical aberrations of the imaging system during the post-processing step in a manner similar to the treatment of refocusing here [24].

In conclusion, we present a holographic method for imaging trapped

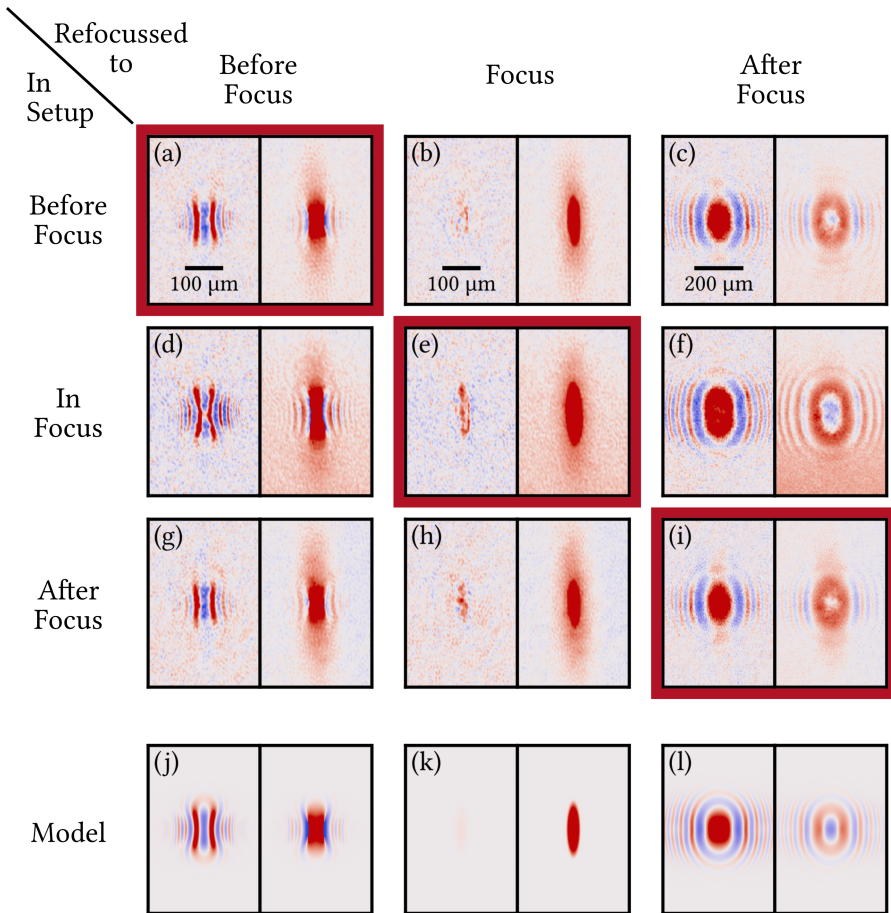


Figure 3.5: Demonstration of numerical refocusing. For every image the left half shows the optical density, the right half shows the accumulated phase. Both are clipped at ± 1 rad. Signal strength varies due to shot-to-shot variations in particle number. Rows represent different locations of the image plane in the setup: (a-c) before the focus, (d-f) in focus (same data as Fig. 3.2), (g-i) after the focus, and (j-l) comparison to the theoretical model. The columns represent a numerical refocusing to a certain image plane, chosen such that the diagonal, which is indicated by red borders, contains the data as recorded by the camera.

quantum gases which provides significant advantages over established methods due to the inherent heterodyne gain. Using off-axis holography we retrieve the phase delay in the sample directly, as opposed to phase contrast imaging or shadowgraph imaging which yield a signal with a non-linear dependence on the phase and require subsequent unwrapping susceptible to noise. Due to the heterodyne gain, density profiles suitable for quantitative analysis are obtained at probe doses two orders of magnitude smaller compared to phase-contrast imaging. This makes it possible to record hundreds of images of the same atom cloud, which enables the study of long term dynamics on a single sample. Using the phase and amplitude, the image plane is numerically scanned to determine the imaging plane of the atoms. Moreover, we demonstrate numerical refocusing, which also provides the possibility to correct coma and spherical aberrations of the imaging system. This imaging method can be extended to observe a contrast between spin species to study the dynamics of spin systems. Converting an existing imaging system for quantum gases to use off-axis holography is done by adding a single reference beam to illuminate the camera, and therefore we envision the method will be adopted in every cold atoms laboratory.

References

- [1] J. Smits, A. P. Mosk, and P. van der Straten, *Opt. Lett.* **45**, 981 (2020).
- [2] E. N. Leith and J. Upatnieks, *J. Opt. Soc. Am.* **52**, 1123 (1962).
- [3] M. Takeda, H. Ina, and S. Kobayashi, *J. Opt. Soc. Am.* **72**, 156 (1982).
- [4] E. Cuche, P. Marquet, and C. Depeursinge, *Appl. Opt.* **39**, 4070 (2000).
- [5] Y. Park, C. Depeursinge, and G. Popescu, *Nature Photonics* **12**, 578 (2018).
- [6] P. Ferraro, S. Grilli, D. Alfieri, S. D. Nicola, A. Finizio, G. Pierattini, B. Javidi, G. Coppola, and V. Striano, *Opt. Express* **13**, 6738 (2005).
- [7] A. Ramanathan, S. R. Muniz, K. C. Wright, R. P. Anderson, W. D. Phillips, K. Helmerson, and G. K. Campbell, *Review of Scientific Instruments* **83**, 083119 (2012).
- [8] M. R. Andrews, M.-O. Mewes, N. J. van Druten, D. S. Durfee, D. M. Kurn, and W. Ketterle, *Science* **273**, 84 (1996).
- [9] C. C. Bradley, C. A. Sackett, and R. G. Hulet, *Phys. Rev. Lett.* **78**, 985 (1997).
- [10] J. M. Higbie, L. E. Sadler, S. Inouye, A. P. Chikkatur, S. R. Leslie, K. L. Moore, V. Savalli, and D. M. Stamper-Kurn, *Phys. Rev. Lett.* **95**, 050401 (2005).
- [11] L. D. Turner, K. P. Weber, D. Paganin, and R. E. Scholten, *Opt. Lett.* **29**, 232 (2004).
- [12] L. D. Turner, K. F. E. M. Domen, and R. E. Scholten, *Phys. Rev. A* **72**, 031403 (2005).
- [13] M. Gajdacz, P. L. Pedersen, T. Mørch, A. J. Hilliard, J. Arlt, and J. F. Sherson, *Review of Scientific Instruments* **84**, 083105 (2013).
- [14] P. B. Wigley, P. J. Everitt, K. S. Hardman, M. R. Hush, C. H. Wei, M. A. Sooriyabandara, P. Manju, J. D. Close, N. P. Robins, and C. C. N. Kuhn, *Opt. Lett.* **41**, 4795 (2016).

-
- [15] P. S. Light, C. Perrella, and A. N. Luiten, *Applied Physics Letters* **102**, 171108 (2013).
- [16] J. P. Sobol and S. Wu, *New Journal of Physics* **16**, 093064 (2014).
- [17] S. Kadlecěk, J. Sebby, R. Newell, and T. G. Walker, *Opt. Lett.* **26**, 137 (2001).
- [18] R. Meppelink, R. A. Rozendaal, S. B. Koller, J. M. Vogels, and P. van der Straten, *Phys. Rev. A* **81**, 053632 (2010).
- [19] F. Verpillat, F. Joud, M. Atlan, and M. Gross, *J. Display Technol.* **6**, 455 (2010).
- [20] P. C. Bons, R. de Haas, D. de Jong, A. Groot, and P. van der Straten, *Phys. Rev. Lett.* **116**, 173602 (2016).
- [21] L. Thylén, *Optical and Quantum Electronics* **15**, 433 (1983).
- [22] J. W. Goodman, *Introduction to Fourier optics*, 3rd ed., by JW Goodman. Englewood, CO: Roberts & Co. Publishers, 2005 **1** (2005).
- [23] W. Bao, S. Jin, and P. A. Markowich, *Journal of Computational Physics* **175**, 487 (2002).
- [24] H. Faulkner, L. Allen, M. Oxley, and D. Paganin, *Optics Communications* **216**, 89 (2003).

4 Observation of a Space-Time Crystal in a Superfluid Quantum Gas

Time crystals are a phase of matter, for which the discrete time symmetry of the driving Hamiltonian is spontaneously broken. The breaking of discrete time symmetry has been observed in several experiments in driven spin systems. Here, an observation of a space-time crystal in a cloud of ultracold atoms is shown. Moreover, a variational model is presented that describes, from first principles, the coupling between the radial breathing mode and the higher-order axial modes that underlies the observation of the space-time crystal. By comparing with numerical simulations the validity of our variational Ansatz is verified. From the model the requirements for the observation of the space-time crystal are determined.



FRANK Wilczek proposed the idea of time crystals in 2012 [2], where, in analogy to space crystals, the continuous time symmetry is broken spontaneously. Since that time there has been discussion on what should constitute a time crystal [3, 4] and how to create it. Watanabe *et al.* [5] showed that in principle the continuous time symmetry cannot be broken spontaneously into a discrete symmetry

This chapter is based on *Observation of a Space-Time Crystal in a Superfluid Quantum Gas*, J. Smits, L. Liao, H. T. C. Stoof, and P. van der Straten, **Phys. Rev. Lett.** **121**, 185301 [1] (© 2018 American Physical Society). Information from the supplementary materials has been merged into the main text and figures have been made legible.



in the ground state. However, there have been proposals to realize instead a discrete time crystal by breaking of a discrete time translation symmetry [6–10]. Following a theoretical model by Yao *et al.* [11] several experiments [12–15] realized this particular symmetry breaking in driven spin systems. These experiments were limited to probing a very restricted number of particles [12] or an ensemble of particles without any spatial resolution [13–15], preventing the direct observation of spatial ordering.

Here, we report the direct observation of a space-time crystal exhibiting not only periodic oscillations in time with double the period of the driving force, but also an oscillatory spatial structure, *i.e.*, both a discrete time translation symmetry as well as the continuous spatial translation symmetry are broken. Due to the small dissipation in our superfluid gas we can study the space-time crystal over an extensive period of time showing the collapse and revival of the oscillating long-lived spatially ordered state. Superfluid quantum gases are the ideal system to study discrete time-crystals. Due to the low viscosity and heat conduction, excitations in the system can be induced without the associated heating of the system. Periodic driving of the excitations in the system can easily be arranged due to the harmonic confinement of the atoms in the trap. Crucial in the driven spin systems [12, 13, 16] has been the occurrence of strong disorder, where either many-body localization or some other mechanism is the cause for the small dissipation in the experiments.

However, as shown by Else *et al.* [17], time-crystals can also exist in the prethermal regime, if the drive frequency is sufficiently large compared to the excitation frequency. Following these experiments there have been a large number of proposals [18–23] for the observation of time crystals using several different systems (see also the review [24]). In superfluid quantum gases disorder is absent. Since superfluid quantum gases can be imaged using phase-contrast techniques, which allows the accumulation of several tens of images of the same superfluid cloud, the dynamics of the system can be studied over many cycles. Moreover, as the conditions of the space-time crystal are not very sensitive to the initial drive of the excitations, the superfluid cloud can be studied over a prolonged period of time by combining multiple measurement series together extending the observation

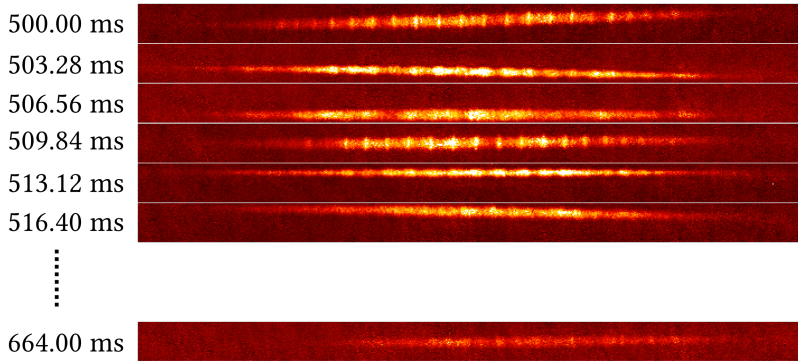


Figure 4.1: Imaging sequence showing the first six and the last image of a run after 500 ms wait time. On the left, the time since the initial pulse is shown. Note the strongly excited radial size oscillation and the presence of the axial excitation. In total 50 images are taken each run with 3.28 ms between images.

period to several seconds. Finally, the dynamics of the superfluid quantum gas in a radial symmetric trap can be simulated using time-splitting spectral methods [25], which allows us to compare our experimental findings with simulations, to elucidate the mechanisms behind the space-time crystal formation.

4.1 Experiment

The superfluid is produced in the trap in a cigar-shaped form. The trap frequencies are $(\omega_\rho, \omega_z) = 2\pi \times (52.7, 1.43)$ Hz, causing the axial size to be about 40 times larger than the radial size. After the cooling process an atom cloud with approximately $N = 5 \times 10^7$ and a condensate fraction of $N_0/N > 0.9$ is obtained. The radial trap frequency is then suddenly perturbed. This induces a radial breathing mode of the cloud with a frequency of $f_D = 104.691(16)$ Hz, which is only weakly damped and has a decay time of several seconds. This radial breathing mode, with a period

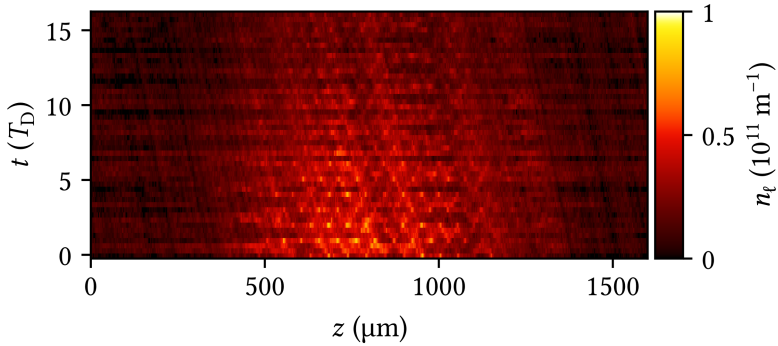


Figure 4.2: Line density n_l as a function of time and position starting 500 ms after the onset of the drive. Time slices taken from a single experimental run. Both in space and time a recurring pattern is observed. The (temporal) period of the pattern corresponds to twice the breathing period T_D . The diagonal streaks in the image are caused by correction for the uncoupled axial center-of-mass motion and darker areas in the imaging. Decrease of the signal is attributed to slight particle loss (3% per shot) due to interactions of imaging light with the atoms.

$T_D = 1/f_D$, acts as the drive for the excitation of the cloud in the axial direction. After many radial oscillations a high-order excitation emerges in the axial direction, which has been observed previously and interpreted in that paper as “Faraday waves” [26]. By observing the spatio-temporal long-range order, we show that an interpretation as a space-time crystal is more appropriate using the modern language of nonequilibrium phase transitions. Figure 4.1 shows several images of the pattern displaying the large variety in radial size and axial excitation. This axial pattern is only observed, if the radial breathing mode is strongly excited and the perturbation of the cloud is in the non-linear regime.

From the experimental images, the column density is determined by inverting the formula used for phase-contrast imaging, see Section 2.2.5. To study the

axial pattern, the resulting column density n_c is integrated over the remaining radial direction to produce a line density

$$n_\ell(t; z) = \int dx n_c(t; x, z). \quad (4.1)$$

The line density is shown in Fig. 4.2 as a function of time. A lattice of maxima in the density is observed in both the temporal and spatial direction; a clear signature of a space-time crystal. The wavenumber of the pattern increases slightly towards the edges of the superfluid, which is attributed to the finite extent of the cloud. The period of the pattern is determined to be $2T_D$ over the entire detection period.

In Fig. 4.3a,c the central part of the axial profile of Fig. 4.2 is shown just after the start of the drive (Fig. 4.3a) and after the axial excitation pattern emerged (Fig. 4.3c). Figure 4.3c shows that the space-time crystal has a centered cubic lattice structure with a period $2T_D$ in time. To determine the long-range temporal and spatial order, these patterns are Fourier transformed and shown in Fig. 4.3b,d, respectively. The Fourier signal for the axial excitation pattern in Fig. 4.3d contains four peaks at $(k/k_c, f/f_D) = (\pm 1, \pm 1/2)$, where the temporal frequency is half the driving frequency $f_D = 1/T_D$. This again shows that we are dealing with a discrete time crystal. The spatial periodicity $2\pi/k_c = 57.1 \mu\text{m}$ is determined by assuming a linear dispersion relation $k_c = 2\pi f c$, and using $f = f_D/2$, and the radially averaged speed of sound [27] $c = \sqrt{\bar{n}U_0/m}$, where $\bar{n} = n(0, 0, 0)/2$ is the cross-sectional averaged density. The appearance of the narrow peaks in the (momentum–frequency) Fourier plane is a clear indication of the simultaneous spatial and temporal long-range order in our system and manifestly indicates that we can truly speak of a space-time crystal. The Fourier signals in Fig. 4.3b,d also contain two peaks in the temporal signal for non-zero frequencies at $f \simeq \pm f_D$ indicating the excitation of a weakly excited scissor mode. Such a mode can easily be induced due to small imperfections in the fabrication of the magnetic trap.



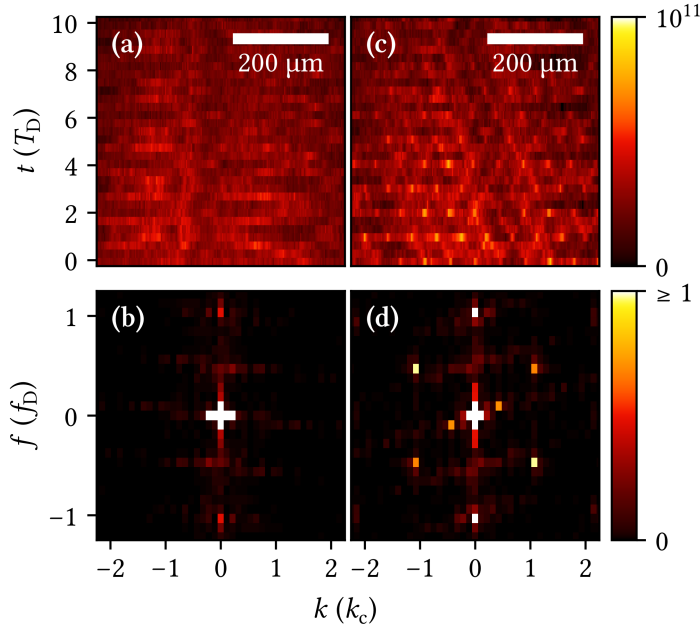


Figure 4.3: Fourier analysis of the line density profile before and after onset of space-time crystalline phase. (a) Line density at the center of the cloud before the onset of the space-time crystalline phase, directly after the excitation. (b) Fourier transform of the data in (a). Peaks at $f/f_D = \pm 1$ are associated with a weakly excited scissors mode. The signal around the origin is associated with the equilibrium profile of the condensate. (c) Take-out of Fig. 4.2. Line density at the center of the cloud after the transition to the space-time crystalline phase, after a driving time of 500 ms. A lattice has formed. (d) Fourier transform of the data in (c), with the appearance of four additional peaks due to the space-time crystal at $(k/k_c, f/f_D) = (\pm 1, \pm 0.5)$, where k_c is the center wavelength. Line density in (a) and (c) is in units of 10^{11} atoms/m. Fourier images in (b) and (d) are truncated and normalized to 1.

4.2 Simulations

In order to further check the validity of our experimental findings, we have numerically simulated the evolution of a Bose-Einstein condensation using a time-splitting spectral method under the same conditions regarding the number of atoms, the trap frequencies, and the drive assuming a radial-symmetric trap, see Ref. [28]. The results in Fig. 4.4a-d show excellent agreement with the experimental results apart from the weak scissor mode, which is absent in the simulations. This agreement shows that the physics of the space-time crystal for our experimental conditions is fully encapsulated in the Gross-Pitaevskii equation.



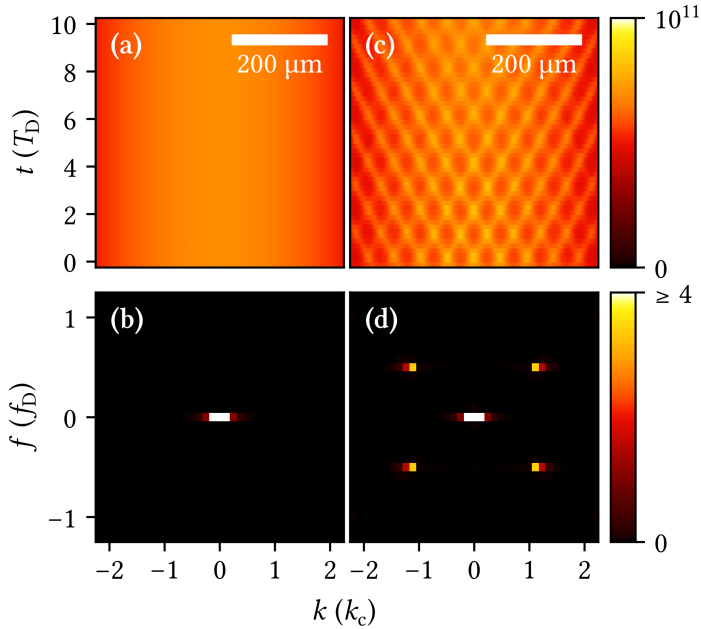


Figure 4.4: Fourier analysis of simulation results. (a) Simulated line density for a modulation depth of 0.02, after a wait time of $25 T_D$. (b) Fourier transform of the data in (a). Notice that in the simulation only the equilibrium profile is visible. (c) Simulated line density for a modulation depth of 0.2 after a wait time of $25 T_D$. A pattern similar to the experimental data of (c) is observed. (d) Fourier transform of (c). Note the appearance of the four additional peaks at $(k/k_c, f/f_D) = (\pm 1, \pm 0.5)$ attributed to the space-time crystal. Line density in (a) and (c) is in units of 10^{11} atoms/m. Fourier images in (b) and (d) are truncated and normalized in the same way as the Fourier images of Fig. 4.3b,d.

4.3 Long-time behavior

To demonstrate the longevity of the space-time crystal, we compare the amplitude of the driving mode to the crystal fraction. To determine the relative amplitude of the driving mode $\delta A_D/\bar{A}_D$, the radial size of the atom cloud $R_\rho(t)$ is determined for every experimental image by performing a least squares fit directly on the data using a Thomas-Fermi distribution [30]. The oscillation is assumed to be of the form $R_\rho(t) \propto \bar{A}_D + \delta A_D \cos(2\pi f_D t)$. The standard deviation σ_ρ and mean \bar{R}_ρ are calculated for a time interval $[t, t + \Delta t]$. The relative amplitude is subsequently calculated using the expression $\sqrt{2}\sigma_\rho/\bar{R}_\rho = \langle \delta A_D/\bar{A}_D \rangle$ over this time interval. We choose $\Delta t = 50$ ms.

To determine the crystalline fraction for the space-time crystal the first 30 images are selected from every measurement run and the center of the atom cloud is used as in Fig. 4.3a,c. Subsequently for every measurement run the crystalline fraction is determined through the formula

$$f_X = \sqrt{\frac{\sum_{(k,f) \in I} |\mathcal{F}(n_\ell)(k, f)|^2}{\sum_{\text{all } (k,f)} |\mathcal{F}(n_\ell)(k, f)|^2}}, \quad (4.2)$$

where $\mathcal{F}(n_\ell)$ represents the Fourier transform of the line density $n_\ell(t; z)$. The set I is chosen as a union of 4 subsets $[\pm k_c - \Delta k, \pm k_c + \Delta k] \times [\pm f_D/2 - \Delta f, \pm f_D/2 + \Delta f]$ centered on the 4 peaks $(\pm k_c, \pm f_D/2)$. Here, Δk is 3 points in Fourier space and is chosen such that any contributions from off-center k as a result of lattice spacing variations due to density inhomogeneities are included. In addition, Δf is chosen to be one point in Fourier space to account for a slight tilt of the crystal lattice due to imperfect compensated axial center-of-mass motion. This corresponds to $\Delta f \approx 0.05 f_D$.

The amplitude of the drive and emergence of the crystalline phase are shown in Fig. 4.5. The dashed line in Fig. 4.5 corresponds to the first measurement run without wait time where no pattern is observed. This is an indicator for the background level due to shot noise. Over a full experimental run of 2.6 s, the pattern is seen to appear and disappear two



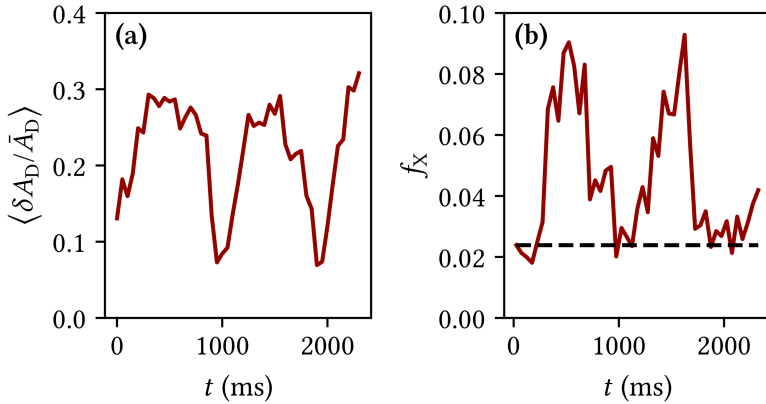


Figure 4.5: Long-term behavior of the amplitudes of the drive and crystal fraction. (a) Relative amplitude of the radial breathing mode derived by fitting a two-dimensional profile to data. (b) Crystal fraction determined from each measurement run. The dashed line indicates background signal from shot-to-shot noise. Notice that the crystalline phase appears a certain time after the driving mode revives [29].

times. Appearances of the space-time crystal occur at times $t = 350$ and 1350 ms, while the disappearance of the crystalline phase coincides with the decrease of the driving mode amplitude to near zero. The space-time crystal lasts, in each individual appearance, for over 500 ms or $50 T_D$. The decrease of the driving mode is caused by the coupling to the scissor mode. The periodicity in the occurrence of the space-time crystal coincides approximately with the period that we extract from our simplified model describing the coupling between scissor and breathing mode [29]. The scissor mode has a period of about $T_D/2$ and is not linearly coupled to the axial excitation pattern due to parity conservation.

4.4 Model

Theoretically, we treat the space-time crystal variationally as a multimode system with the mode functions $P_{4j+2}(\tilde{z}) - P_{4j}(\tilde{z})$ with $\tilde{z} = z/R_z(t)$ in terms of Legendre polynomials, and frequencies f_j excited by the drive due to the time-dependence of the Thomas-Fermi radii $R_x(t)$, $R_y(t)$ and $R_z(t)$, for which $R_i(t) = R_i(t+T_D)$ and $i = x, y$, and z . After substituting this *Ansatz* in the action for the Gross-Pitaevskii equation and neglecting nonlinear mode coupling, we ultimately obtain the Hamiltonian

$$\hat{H} = \sum_j \left[2\pi\hbar f_j a_j^\dagger a_j + g_j(t)(a_j^\dagger a_j^\dagger + a_j a_j + 2a_j^\dagger a_j) \right], \quad (4.3)$$

where $a_j^{(\dagger)}$ are the annihilation (creation) operators for quanta in the mode j and $g(t)$ is the coupling with the periodicity of the drive.

By moving to the rotating frame and applying the rotating-wave approximation to eliminate the time-dependence of the drive $g(t)$ we find the effective Hamiltonian

$$\hat{H}_{\text{eff}} = \sum_j \left[2\pi\hbar(f_j - f_D/2)a_j^\dagger a_j + g_{j,0}(a_j^\dagger a_j^\dagger + a_j a_j) \right], \quad (4.4)$$

where $g_{j,0}$ is proportional to the amplitude of the drive. Note that this yields



a Hamiltonian, which is time independent in the rotating frame, and that represents the appropriate Hamiltonian for prethermalization of the system.

The mode that is observed depends on the driving frequency f_D and the driving amplitude $\langle \delta A_D / \bar{A}_D \rangle$ [31]. In Fig. 4.6 the minimum required amplitude for existence of a space-time crystal is shown as a function of the driving frequency. In absence of damping, as shown in Fig. 4.6a, a mode j can be driven with an arbitrary small amplitude, if the resonance condition $2f_j = f_D$ is fulfilled. In the case of damping, the threshold for exciting the pattern becomes nonzero. Applying the analysis of Ref. [31] to our experimental conditions (see Fig. 4.6b) shows that the driving amplitude used in our experiment is sufficient to excite several modes j . The competition between these modes causes one of the modes to grow exponentially, thus dominating the observed pattern.

The Hamiltonian of Eq. (4.4) explicitly breaks the $U(1)$ symmetry $a \rightarrow ae^{i\vartheta}$. This implies that in the laboratory frame $\langle a_j a_j \rangle \propto e^{-2\pi i f_D t}$ is always non-zero and oscillates with the period of the drive. However, there is an additional \mathbb{Z}_2 symmetry $a_j \rightarrow -a_j$, which is spontaneously broken when $\langle a_j \rangle \neq 0$, which occurs when the mode is Bose condensed. This leads to the appearance of the time-dependence $\langle a_j \rangle \propto e^{-\pi i f_D t}$ in the laboratory frame. The breaking of this \mathbb{Z}_2 symmetry thus leads to an oscillation with period $2T_D$. We propose that for low occupation ($\langle a_j \rangle \simeq 0$) the system is in a state dominated by a description based on the evolution of the pair correlation $\langle a_j a_j \rangle$. As occupation in the mode grows, *i.e.*, the occupation number of the mode $\langle a_j \rangle$ goes up, there is a phase transition from the paired state to a state dominated by dynamics in $\langle a_j \rangle$, breaking the \mathbb{Z}_2 symmetry. We identify this transition as the phase transition to the time crystal.

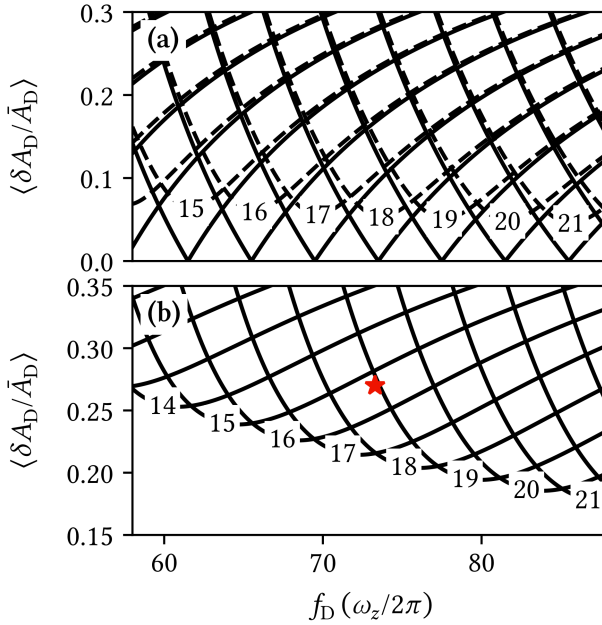


Figure 4.6: Minimum required driving amplitude $\langle \delta A_D / \bar{A}_D \rangle$ as a function of the driving frequency f_D in linear response analysis [31]. (a) Without damping (solid line) a mode j can be driven with arbitrary small amplitude, if the driving frequency coincides with twice the mode frequency f_j , whereas for small damping (dashed line) there is for any drive frequency a threshold, below which the mode is not excited. (b) Under our experimental conditions (indicated by the red star), the damping is larger and the threshold for exciting modes becomes larger. In the case of linear response, the modes $j = 16, 17$, and 18 can be excited and depending on the competition between these modes, one of them dominates the pattern [31].

4.5 Conclusion

In summary, we have shown the existence of a space-time crystal which is long-lived and robust against fluctuations in experimental parameters. Future experiments are aimed at studying elementary excitations such as solitons and sound in the presence of a space-time crystal, as our system is an excellent testing ground for these excitations. Moreover, it can be explored whether this spatially ordered state has supersolid properties, as this would allow study of out-of-equilibrium supersolids [32, 33], combining the fields of time crystals and supersolids and exploring a currently unknown corner of physics.

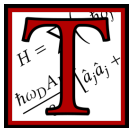
References

- [1] J. Smits, L. Liao, H. T. C. Stoof, and P. van der Straten, *Phys. Rev. Lett.* **121**, 185301 (2018).
- [2] F. Wilczek, *Phys. Rev. Lett.* **109**, 160401 (2012).
- [3] P. Bruno, *Phys. Rev. Lett.* **110**, 118901 (2013).
- [4] P. Nozières, *Europh. Lett.* **103**, 57008 (2013).
- [5] H. Watanabe and M. Oshikawa, *Phys. Rev. Lett.* **114**, 251603 (2015).
- [6] D. V. Else, B. Bauer, and C. Nayak, *Phys. Rev. Lett.* **117**, 090402 (2016).
- [7] K. Sacha, *Phys. Rev. A* **91**, 033617 (2015).
- [8] L. Guo, M. Marthaler, and G. Schön, *Phys. Rev. Lett.* **111**, 205303 (2013).
- [9] V. Khemani, A. Lazarides, R. Moessner, and S. L. Sondhi, *Phys. Rev. Lett.* **116**, 250401 (2016).
- [10] C. W. von Keyserlingk, V. Khemani, and S. L. Sondhi, *Phys. Rev. B* **94**, 085112 (2016).
- [11] N. Y. Yao, A. C. Potter, I.-D. Potirniche, and A. Vishwanath, *Phys. Rev. Lett.* **118**, 030401 (2017).
- [12] J. Zhang, P. W. Hess, A. Kyprianidis, P. Becker, A. Lee, J. Smith, G. Pagano, I.-D. Potirniche, A. C. Potter, A. Vishwanath, N. Y. Yao, and C. Monroe, *Nature* **543**, 217 (2017).
- [13] S. Choi, J. Choi, R. Landig, G. Kucsko, H. Zhou, J. Isoya, F. Jelezko, S. Onoda, H. Sumiya, V. Khemani, C. von Keyserlingk, N. Y. Yao, E. Demler, and M. D. Lukin, *Nature* **543**, 221 (2017).
- [14] J. Rovny, R. L. Blum, and S. E. Barrett, *Phys. Rev. Lett.* **120**, 180603 (2018).
- [15] S. Pal, N. Nishad, T. S. Mahesh, and G. J. Sreejith, *Phys. Rev. Lett.* **120**, 180602 (2018).
- [16] J. Rovny, R. L. Blum, and S. E. Barrett, *Phys. Rev. B* **97**, 184301 (2018).
- [17] D. V. Else, B. Bauer, and C. Nayak, *Phys. Rev. X* **7**, 011026 (2017).

-
- [18] B. Huang, Y.-H. Wu, and W. V. Liu, *Phys. Rev. Lett.* **120**, 110603 (2018).
- [19] K. Sacha, *Phys. Rev. A* **91**, 033617 (2015).
- [20] E. Lustig, Y. Sharabi, and M. Segev, ArXiv e-prints, 1803.08731 (2018).
- [21] W. W. Ho, S. Choi, M. D. Lukin, and D. A. Abanin, *Phys. Rev. Lett.* **119**, 010602 (2017).
- [22] K. Mizuta, K. Takasan, M. Nakagawa, and N. Kawakami, ArXiv e-prints, 1804.01291 (2018).
- [23] A. Russomanno, F. Iemini, M. Dalmonte, and R. Fazio, *Phys. Rev. B* **95**, 214307 (2017).
- [24] K. Sacha and J. Zakrzewski, *Rep. Progr. Phys.* **81**, 016401 (2018).
- [25] W. Bao, D. Jaksch, and P. A. Markowich, *J. Comp. Phys.* **187**, 318 (2003).
- [26] P. Engels, C. Atherton, and M. A. Hoefer, *Phys. Rev. Lett.* **98**, 095301 (2007).
- [27] E. Zaremba, *Phys. Rev. A* **57**, 518 (1998).
- [28] See Section “Numerical simulations” of the Supplemental Material of Ref. [1] for more information.
- [29] See Section “The coupling between the radial breathing mode and the scissors mode” of the Supplemental Material of Ref. [1] for more information.
- [30] C. J. Pethick and H. Smith, *Bose-Einstein Condensation in Dilute Gases*, 2nd ed. (Cambridge University Press, 2008).
- [31] L. Liao, J. Smits, P. van der Straten, and H. T. C. Stoof, *Phys. Rev. A* **99**, 013625 (2019).
- [32] J. Leonard, A. Morales, P. Zupancic, T. Esslinger, and T. Donner, *Nature* **543**, 87 (2017).
- [33] J.-R. Li, J. Lee, W. Huang, S. Burchesky, B. Shteynas, F. Ç. Top, A. O. Jamison, and W. Ketterle, *Nature* **543**, 91 (2017).

5 Dynamics of a Space-Time Crystal in an Atomic Bose-Einstein Condensate

A space-time crystal has recently been observed in a superfluid Bose gas. Here we construct a variational model that allows us to describe from first principles the coupling between the radial breathing mode and the higher-order axial modes that underlies the observation of the space-time crystal. By comparing with numerical simulations we verify the validity of our variational Ansatz. From the model we determine the requirements for the observation of the space-time crystal and the Ising-like nature of the symmetry breaking involved. Also, we find the onset and growth rate of the space-time crystal, which can be compared to experiments.



THE idea of time crystals was proposed by Wilczek in 2012 [2, 3], where for a system in its ground state the continuous time-translation symmetry is spontaneously broken. The proposal stimulated vigorous debates about the properties of a time crystal [4, 5]. Time crystals based on the time-dependent correlation functions are proposed by Watanabe *et al.* [6], and they showed that spontaneously

This chapter is based on *Dynamics of a Space-Time Crystal in an Atomic Bose-Einstein Condensate*, L. Liao, J. Smits, P. van der Straten, and H. T. C. Stoof **Phys. Rev. A** **99**, 013625 [1] (© 2019 American Physical Society). The groundwork for this paper has been done by L.L., while J.S. contributed to this paper by rechecking the theory, running simulations, formatting figures and deriving the quantized model from the classical one.



breaking of the continuous time symmetry into a discrete symmetry in the quantum ground state is impossible. However, the possibility of breaking of a discrete time translation symmetry is not ruled out [7–13]. Yao *et al.* [14] proposed a model of a one-dimensional discrete time crystal occurring in periodically driven spin systems, which is followed by experimental observations of a discrete time crystal in an interacting spin chain of trapped atomic ions [15], and in disordered [16] and ordered magnetic systems [17–19]. Although the experiments clearly showed the breaking of discrete time symmetry, the experiments do not allow for a full theoretical description, since the underlying physics of those spin systems is far too complex. In contrast, Smits *et al.* [20] reported the observation of a space-time crystal in a superfluid gas, where excitations can be described nearly from first principles. Recently, time crystals have been reviewed in Ref. [21].

In this paper we describe a variational model, that fully describes the experimental findings of Ref. [20]. The model is based on the interaction between the radial breathing mode and higher-order axial modes, which have been observed before and were dubbed a “Faraday” wave [22]. Both excitations are fully determined by their density and phase and this quantum hydrodynamical description allows for a complete characterization of the different orders of the coupling. The results of the model are compared to numerical simulations based on the Gross-Pitaevskii (GP) equation, which accurately describes the dynamics in the superfluid. The agreement between the model and numerical simulations shows that our model captures all the relevant dynamics in the superfluid needed to understand the formation and growth of the space-time crystal.

Since our variational model is constructed from first principles, we can extract properties of the space-time crystal, which can be compared to the theoretical proposals for space-time crystals [23–27]. In our model we identify a prethermal state for the space-time crystal, that is only weakly coupled to the ground state of the system and thus allows for its observation in the experiment. We show that the Hamiltonian describing the system has a hidden \mathbb{Z}_2 symmetry, which is broken in the crystalline phase.

The paper is organized as follows. In Sec. 5.1 we shortly describe the experimental sequence that leads to the space-time crystal. In Sec. 5.2 we introduce the variational model and define the higher-order axial modes, which are given in terms of Legendre polynomials. The model allows for the description of the coupling between the radial and axial excitations and the second- and third-order interactions are taken into account. In Sec. 5.3 we test our variational *Ansatz* and find satisfactory agreement between the model and simulations for the atomic line density and the atomic flux. In Sec. 5.4 we derive the evolution equations for the amplitudes of the higher-order axial modes and determine the frequencies of the modes, which are compared to the frequency of their oscillations in the numerical simulations. In Sec. 5.5 we show how the higher-order axial modes lead to a back action on the breathing mode. In Sec. 5.6 we present a quantized version of our Hamiltonian and derive the quantum properties of the space-time crystal, that has been observed recently [20]. Finally we derive in Sec. 5.7 the onset of the higher-order axial modes and their gain, and argue that the modes can only be excited in a narrow window of the driving amplitude.

5.1 The experiment

In the experiment [28] we cool ^{23}Na atoms using laser and evaporative cooling techniques to a temperature of 300 nK, which is far below the BEC transition temperature of about 1 μK . In this way the cloud is nearly fully condensed, although there always remains a small fraction of thermal atoms. The atoms are trapped in a cylindrical symmetric harmonic trap with the potential $V(\rho, z)$ given by

$$V(\rho, z) = \frac{1}{2}m\omega_\rho^2 (\rho^2 + \lambda^2 z^2), \quad (5.1)$$

with m the mass of the atoms, ω_ρ the trap frequency in the radial direction ρ and $\omega_z = \lambda\omega_\rho$ the trap frequency in the axial direction z . In the experiment with trap frequencies $(\omega_\rho, \omega_z) = 2\pi \times (52.7, 1.43)$ Hz the aspect ratio λ is



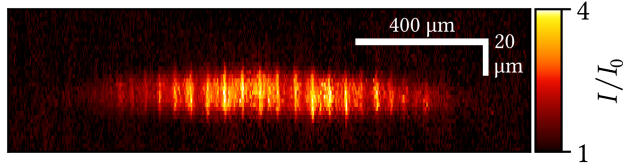


Figure 5.1: Phase contrast image of a higher-order axial excitation. The acquired phase due to the condensate is small with respect to 2π , such that for a phase delay of $\pi/3$ of the phase spot the minimum of the intensity is given by I_0 and the maximum by $4I_0$, where I_0 is the intensity on the camera without the atoms (see Ref. [29]).

small ($\lambda \simeq 0.027$), which causes the cloud of atoms to be cigar-shaped. We condense about $N \simeq 5 \times 10^7$ atoms and the condensate fraction is $N_0/N \simeq 90\%$. After the preparation the radial trap frequency is modulated with three pulses and the radial breathing mode of the Bose-Einstein condensate is excited. The pulse duration is 50 ms and the modulation depth is 0.125. Due to the superfluid character of the cloud the breathing oscillation is only weakly damped and acts as a drive for higher-order axial excitations. Since the trap frequency in the radial direction greatly exceeds the trap frequency in the axial direction, an excitation in the radial direction can couple through the non-linear interaction to high-order excitations in the axial direction.

In Fig. 5.1 a typical experimental result is shown 500 ms after the trap modulation with the three pulses using phase contrast imaging [29]. Although the intensity in a phase contrast image is not linearly dependent on the density, it is clear that the higher-order excitation as indicated by the fast oscillations in the intensity is mainly in the z -direction and that the excitation is almost constant in the radial direction. This is essential for the theoretical model that we construct in this article and allows us to variationally obtain the model from first principles.

5.2 Effective action

In the model we describe only the condensed part of the cloud and neglect the influence of the thermal cloud, whose main effect is to introduce a small damping in the condensate dynamics. The state of the condensate is fully described by the wavefunction $\Psi(\mathbf{r}, t)$ and its evolution is given by the GP equation with a non-linear interaction due to the atom-atom interaction characterized by a single parameter a_s , the s-wave scattering length. Equivalently we can use instead an alternative description, where we treat the condensate as a superfluid and use the techniques of quantum hydrodynamics for its description. The condensate is then fully described by the density $n(\mathbf{r}, t)$ and its phase $\phi(\mathbf{r}, t)$, for which an effective action can be constructed. Note that both descriptions are identical [30], but for our purposes it is more appropriate to use the density and the phase. For our bosonic system the effective action is given by

$$S = \int dt \int d\mathbf{r} L, \quad (5.2)$$

with the Lagrangian density L defined by [31]

$$L = -\hbar n \frac{\partial \phi}{\partial t} - nV(\mathbf{r}) - \frac{T^{2B}}{2} n^2 - \frac{\hbar^2}{2m} \left[\frac{(\nabla n)^2}{4n} + n(\nabla \phi)^2 \right], \quad (5.3)$$

where the quantum pressure is given by the first term within the square brackets. The non-linear interaction is determined by the two-body interaction $T^{2B} = 4\pi\hbar^2 a_s/m$. It is straightforward to check that minimizing the action with respect to the phase ϕ , *i.e.*, $\delta S/\delta \phi = 0$, corresponds to the continuity equation for the density

$$\frac{\partial n}{\partial t} + \nabla \cdot \mathbf{j} = 0. \quad (5.4)$$

Minimizing the action with respect to the density, *i.e.*, $\delta S/\delta n = 0$, corresponds to the Josephson equation

$$\hbar \frac{\partial \phi}{\partial t} + \left(\frac{1}{2} m \mathbf{v}^2 + V + T^{2B} n - \frac{\hbar^2}{2m\sqrt{n}} \nabla^2 \sqrt{n} \right) = 0. \quad (5.5)$$



Here we introduced the current density $\mathbf{j}(\mathbf{r}, t) = n(\mathbf{r}, t)\mathbf{v}(\mathbf{r}, t)$ and the velocity of the flow $\mathbf{v}(\mathbf{r}, t) = \hbar\nabla\phi(\mathbf{r}, t)/m$. The characteristic length of the trap is the harmonic oscillator length a_{ho} , which is defined as $a_{\text{ho}} = \sqrt{\hbar/m\bar{\omega}}$ with the geometric trap frequency $\bar{\omega} = (\omega_x\omega_y\omega_z)^{1/3}$. Note that for the experimental parameters $N_0a_s/a_{\text{ho}} \simeq 10.000$ and thus much larger than 1, such that the quantum pressure term can be neglected, or in the language of the GP equation, that the atoms are in the Thomas-Fermi (TF) limit [30].

In our model we assume that the density modulation of the excitations are small and thus that we can expand the total density n and phase ϕ as the sum of a condensate part determined by n_D and ϕ_D containing the radial dynamics, and the part containing the higher-order axial excitations described by n_A and ϕ_A :

$$n = n_D + n_A, \quad \phi = \phi_D + \phi_A. \quad (5.6)$$

Substituting (5.6) into the Lagrangian density of (5.3), and considering only the second-order and the third-order terms of n_A or ϕ_A , the Lagrangian density becomes

$$\begin{aligned} L_A = & -\hbar n_A \frac{\partial \phi_A}{\partial t} - \frac{T^{2B}}{2} n_A^2 \\ & - \frac{\hbar^2}{2m} (n_D (\nabla \phi_A)^2 + 2n_A \nabla \phi_D \cdot \nabla \phi_A + n_A (\nabla \phi_A)^2). \end{aligned} \quad (5.7)$$

Here the quantum pressure term is neglected, as discussed after (5.5). Terms depending solely on the properties of the radial excitations n_D and ϕ_D have been eliminated, but they are reintroduced later on in Sec. 5.5.

Since radial excitations have a large energy $\hbar\omega_D \simeq 2\hbar\omega_\rho$ with respect to the splitting of the excitations in the axial direction of about $2\hbar\omega_z$, we expect that radial excitations can in principle be coupled to many different modes j in the axial direction. Thus we expand the higher-order axial mode density n_A and phase ϕ_A in modes j as

$$n_A = \sum_j n_j, \quad \phi_A = \sum_j \phi_j, \quad (5.8)$$

where the mode functions associated with the quantum number j are still to be determined.

There has been some theoretical analysis using a time-dependent non-polynomial, non-linear Schrödinger equation applied to model cigar-shaped condensates [32, 33]. However, there are exact solutions using Legendre polynomials $P_j(\tilde{z})$ with $\tilde{z} = z/R_z$ for an one-dimensional Bose-Einstein condensate in a harmonic trap in the TF regime [31, 34]. Here R_z is the Thomas-Fermi size of the condensate in the axial direction. Under our experimental conditions it is clear that the cloud is not in the one-dimensional regime, since the chemical potential μ ($\mu/h \simeq 2$ kHz) is much larger than the excitation energy $\hbar\omega_\rho$. However, as can be seen from the excitation profile in Fig. 5.1, there is nearly no radial dependence of the higher-order axial profile, so the Legendre polynomials seem to be the most suitable basis functions for the expansion of the excitation profile. Furthermore, due to parity conservation the mode number j of $P_j(\tilde{z})$ is required to be even, *i.e.*, the radial breathing mode can only couple to axial modes with an even parity. The higher-order Legendre polynomials have simple sinusoidal behavior around $\tilde{z} \simeq 0$, but for $|\tilde{z}| \rightarrow 1$ their amplitude strongly increases. In the experiment, the density of the condensate goes to zero near the edge with $|\tilde{z}| \simeq 1$, but also the excitation profile diminishes strongly. Thus a single Legendre polynomial does not satisfy the right boundary condition. However, if we subtract two Legendre functions, where the mode numbers differ by two, the linear combination remains a solution for the one-dimensional case and decreases to zero near the edges. Thus we choose the high-order axial mode function $L_j(\tilde{z})$ as

$$L_j(\tilde{z}) = P_{4j+2}(\tilde{z}) - P_{4j}(\tilde{z}), \quad (5.9)$$

where j is chosen in such a way that the mode functions are countable and $j = 0, 1, 2, 3, \dots$. Note that these mode functions are independent of the time t if the length R_z of the condensate is constant. However, in our experiment, where the radial breathing mode is excited, there is coupling with the axial modes [20], as R_z and thus also $L_j(\tilde{z})$ are functions of time.

For the density and the phase of the higher-order axial mode functions we



can now use the variational *Ansatz*

$$n_j(z, t) \equiv -\dot{\kappa}_j(t)L_j(\tilde{z}), \quad (5.10)$$

$$\phi_j(z, t) \equiv \frac{T^{2B}}{\hbar}\kappa_j(t)L_j(\tilde{z}), \quad (5.11)$$

with κ_j the mode amplitude. The relation between the density and phase are taken such that the mode functions obey the Josephson equation of (5.5) if the length of the condensate R_z is constant. In (5.10) and in the remainder of the article the dot indicates the derivative with respect to time. Note that the excitation profile is now fully determined by the time-dependent amplitudes $\kappa_j(t)$.

For the radial excitation, the density and the phase are determined in the TF approximation by [35–38]

$$n_D(\mathbf{r}, t) = \frac{n_0}{b_x b_y b_z} (1 - \tilde{x}(t)^2 - \tilde{y}(t)^2 - \tilde{z}(t)^2), \quad (5.12)$$

and

$$\nabla\phi_D(\mathbf{r}, t) = \frac{mR_\rho(0)}{\hbar} \left(\dot{b}_x \tilde{x}(t) \mathbf{e}_x + \dot{b}_y \tilde{y}(t) \mathbf{e}_y + \frac{\dot{b}_z \tilde{z}(t)}{\lambda} \mathbf{e}_z \right), \quad (5.13)$$

in which the density in the center of the condensate is given by $n_0 \equiv m\omega_\rho^2 R_\rho(0)^2 / 2T^{2B}$ with $R_\rho(0) \equiv R_x(0) = R_y(0)$. The dimensionless time-dependent variables are given by

$$\begin{aligned} \tilde{x}(t) &= \frac{x}{b_x(t)R_x(0)}, & \tilde{y}(t) &= \frac{y}{b_y(t)R_y(0)}, \\ \tilde{z}(t) &= \frac{z}{b_z(t)R_z(0)}, \end{aligned} \quad (5.14)$$

where the parameters $b_i(t)$ with $i = x, y, z$ determine the explicit time-dependence of the size of the condensate and $R_i(0)$ are the equilibrium values. The evolution of the parameters b_i is discussed in Sec. 5.5.

To find the evolution of the amplitudes κ_j we can substitute Eqs. (5.8-5.11) in the Lagrangian density of (5.7) and obtain for the Lagrangian L_A defined by

$L_A = \int d\mathbf{r} L_A$ the result

$$L_A = \eta \sum_{ij} \left(\frac{Q_{ij}}{2} b_x b_y b_z (\dot{\kappa}_i \dot{\kappa}_j - \Gamma_{ij}(t) \kappa_i \kappa_j) + \frac{T^{2B} \lambda^2}{2mR_\rho(0)^2} \frac{b_x b_y}{b_z} \sum_k M_{ijk} \kappa_i \kappa_j \kappa_k \right), \quad (5.15)$$

where we have integrated out the dependence on \mathbf{r} in (5.7), since both the radial and axial modes are fully specified in the ρ and z -direction. The Lagrangian is given in terms of the following integrals

$$T_{ij} = \int_{-1}^1 d\tilde{z} (1 - \tilde{z}^2)^2 L'_i(\tilde{z}) L'_j(\tilde{z}), \quad (5.16)$$

$$Q_{ij} = \int_{-1}^1 d\tilde{z} (1 - \tilde{z}^2) L_i(\tilde{z}) L_j(\tilde{z}), \quad (5.17)$$

$$M_{ijk} = \int_{-1}^1 d\tilde{z} (1 - \tilde{z}^2) L_i(\tilde{z}) L'_j(\tilde{z}) L'_k(\tilde{z}), \quad (5.18)$$

combined with the effective mass parameter η ,

$$\eta = \pi T^{2B} R_\rho(0)^2 R_z(0), \quad (5.19)$$

and the square of the effective frequency $\Gamma_{ij}(t)$ given by

$$\Gamma_{ij}(t) = \frac{\omega_z^2}{4} \frac{T_{ij}}{Q_{ij}} \frac{1}{b_x b_y b_z^3}. \quad (5.20)$$

In Eqs. (5.16-5.18) the prime indicates the derivative with respect to \tilde{z} . Note that the first two terms of the Lagrangian of (5.15) have the form of a harmonic oscillator, where the first term in the brackets is proportional to the kinetic energy and the second part to the potential energy. From the Lagrangian we can derive the evolution equation of the amplitudes κ_i in Sec. 5.4, but before proceeding we need to test the validity of the mode functions $L_i(\tilde{z})$ in our variational *Ansatz*.



5.3 Comparison to numerical simulations

In order to test our mode functions $L_j(\tilde{z})$, we can compare their density profile with the experimental density profiles, as seen for instance in Fig. 5.1. However, in the experiment we have to excite the axial excitation sufficiently to be able to detect the density modulations, although in our model we assume that the excitations are small compared to the condensate density. Strong excitations also have the drawback that multiple modes j can be excited simultaneously and that the experimental excitations have to be compared to a linear superposition of modes. This adds a large number of adjustable parameters in the comparison and thus makes the outcome less certain. Finally, as discussed in Ref. [20], due to small imperfections in the magnetic trap, radial excitations couple to the scissor mode, which adds even more uncertainty in the comparison.

As stated in Sec. 5.2 we incorporate only the condensate in our model and its evolution is described by the GP equation. There are very efficient schemes, which allow for the numerical integration of the GP equation using time-splitting methods. In our case with the cylindrical symmetric trap, we can reduce the number of dimension from three to two, which drastically reduces the computation time. Since in the simulation we simulate the (complex) wavefunction, we have not only access to the density, but can also extract the phase of the condensate. This allows for the determination of the flux in the condensate, which on the one hand only depends on the excitations and not on the bulk of the condensate, and on the other hand is a quantity that cannot be obtained experimentally. Therefore in this section we describe the numerical simulations of the GP equation, and the comparison of the outcomes with the theoretical model.

For simulations, the GP equation is rewritten in cylindrical coordinates (ρ, z) with the condensate wavefunction equal to $\Psi(\mathbf{r}, t) = f(\rho, z, t)/\sqrt{\rho}$ using the

axial symmetry. The equation to solve becomes

$$(i - \hat{\alpha})\hbar \frac{\partial f(\rho, z, t)}{\partial t} = \left(-\frac{\hbar^2}{2m} \left[\frac{\partial^2}{\partial \rho^2} + \frac{\partial^2}{\partial z^2} - \frac{1}{4\rho^2} \right] + V(\rho, z) + \frac{T^{2B}}{2\pi\rho} |f(\rho, z, t)|^2 - \mu \right) f(\rho, z, t), \quad (5.21)$$

where $\hat{\alpha}$ is a phenomenological damping constant [39]. This equation is solved by employing a splitting spectral method [40]. Time steps are chosen to be $0.001\tau_p$ with $\tau_p = 2\pi/\omega_\rho$ the oscillation period in the radial direction. The grid size is 1024×256 with a physical size of $[-2R_z, 2R_z] \times [-2R_\rho, 2R_\rho]$. The simulation is initiated with a profile in the TF limit and the ground state is found by imaginary time evolution. After reaching the ground state, the system can be excited in two ways. First, we can employ the excitation scheme of the experiment by modulating the radial trap frequency. This allows for a full comparison with the outcome of the experiments, although in that case the system is excited strongly. Alternatively, we can artificially imprint the proper phase profile corresponding to one mode function j on the condensate, such that the condensate starts to oscillate in the right mode. From these simulations an accurate frequency for each of the eigenmodes can be extracted. The last method is employed in this section.

In Fig. 5.2 we plot the line density profile of the high-order axial mode $\ell(\tilde{z}) = \pi(1 - \tilde{z}^2)n_A(\tilde{z})$ as a function of \tilde{z} by subtracting the ground state of the condensate from the profile after the phase imprinting. The figure shows that our theoretical prediction agrees well with the simulation data and that there are only relative small deviations near the edge of the condensate at $|\tilde{z}| \rightarrow 1$. Note that due to the quantum pressure term in the simulation the density exponentially decays to zero at the edge, whereas in the model the density has a discontinuity near the edge, which is not physical. This may explain the deviations near the edge of the condensate.

It is also useful to investigate the axial component of the current density $J_z(\tilde{z})$, which is given by

$$J_z(\tilde{\rho}, \tilde{z}, t) \equiv n(\tilde{\rho}, \tilde{z}, t) \frac{\hbar}{m} \frac{\partial \phi(\tilde{\rho}, \tilde{z}, t)}{\partial z}. \quad (5.22)$$



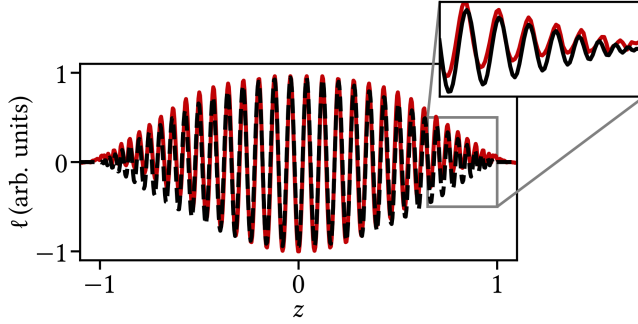


Figure 5.2: The high-order line density profile $\ell(\tilde{z})$ as a function of \tilde{z} with $j = 19$. The black curve is the theoretical prediction of the mode density profile, whereas the red curve corresponds to the numerical simulation.

Using the expansion of (5.6), the expressions for n_D , ϕ_D in Eqs. (5.12-5.14), and n_A , ϕ_A in Eqs. (5.8-5.11), we ultimately obtain

$$J_z(\tilde{\rho}, \tilde{z}, t) = \left(\frac{n_0}{b_x b_y b_z} (1 - \tilde{\rho}^2 - \tilde{z}^2) - \kappa_j L_j(\tilde{z}) \right) \times \left(R_z(0) \dot{b}_z \tilde{z} + \frac{T^{2B} \kappa_j}{m R_z(0) b_z} (8j + 3) P_{4j+1}(\tilde{z}) \right). \quad (5.23)$$

Here the following property of the Legendre polynomials

$$\frac{\partial}{\partial z} (P_{4j+2}(z) - P_{4j}(z)) = (8j + 3) P_{4j+1}(z) \quad (5.24)$$

is used.

In Fig. 5.3 the comparison for the flux between the theoretical model and the simulation is shown. The agreement between theory and simulation is excellent apart from a small deviation near the edge of the condensate. It is also clear that the numerical simulations show only small variations of the flux in the radial direction, proving our basic assumption that the restriction of the mode function to only allow for axial variation is justified.

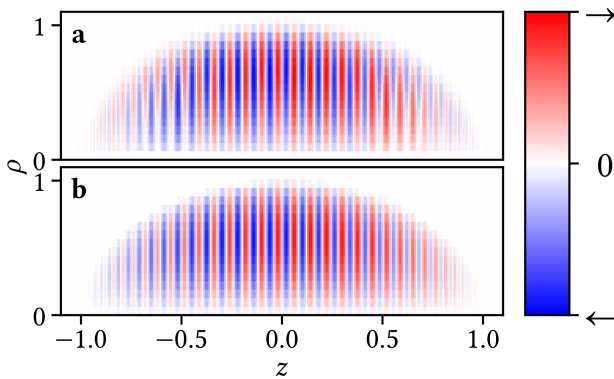


Figure 5.3: The density plot of the axial particle flux $\tilde{\rho} J_z(\tilde{\rho}, \tilde{z}, t)$ as a function of the scaled radial and axial position for $j = 19$ for (a) the numerical simulation and (b) our theoretical model.

The agreement for both the density and the flux between simulation and model shows that our choice for the mode functions is very accurate. Thus we can now address the dynamics of the high-order axial modes using these mode functions.

5.4 No mode coupling between axial modes

If we exclude the coupling of different higher-order modes, we need to consider only the diagonal terms in the Lagrangian L_A in (5.15) and we obtain

$$\begin{aligned}
 L_A = & \eta \sum_j \left(\frac{Q_{jj}}{2} b_x b_y b_z [\dot{\kappa}_j^2 - \Gamma_{jj}(t) \kappa_j^2] \right. \\
 & \left. + \frac{T^{2B} \lambda^2}{2mR_\rho(0)^2} \frac{b_x b_y}{b_z} M_{jjj} \kappa_j^2 \dot{\kappa}_j \right). \quad (5.25)
 \end{aligned}$$



Because the Lagrangian contains only the first-order time derivative $\dot{\kappa}_j$, the equations of motions follow from the Euler-Lagrange equation

$$\frac{\partial L}{\partial \kappa_j} - \frac{d}{dt} \frac{\partial L}{\partial \dot{\kappa}_j} = 0. \quad (5.26)$$

Using (5.26) for the Lagrangian of (5.25) the equation of motion for the amplitudes of the higher-order axial mode becomes

$$\begin{aligned} \ddot{\kappa}_j + \Gamma_{jj}(t)\kappa_j + \left(\frac{\dot{b}_x}{b_x} + \frac{\dot{b}_y}{b_y} + \frac{\dot{b}_z}{b_z} \right) \dot{\kappa}_j \\ + \frac{T^{2B}\lambda^2 M_{jjj}}{2mR_\rho(0)^2 Q_{jj}} \left(\frac{\dot{b}_x}{b_x} + \frac{\dot{b}_y}{b_y} - \frac{\dot{b}_z}{b_z} \right) \frac{\kappa_j^2}{b_z^2} = 0. \end{aligned} \quad (5.27)$$

When the radial excitations are small and the terms \dot{b}_i/b_i can be neglected in (5.27), the solution of (5.27) is simply sinusoidal with a frequency Ω_j given by

$$\Omega_j = \sqrt{\Gamma_{jj}} = \frac{\omega_z}{2} \sqrt{\frac{T_{jj}}{Q_{jj}}}, \quad (5.28)$$

with $b_x = b_y = b_z = 1$. The integrals T_{jj} and Q_{jj} can easily be evaluated and for large j this leads to $\Omega_j \simeq (2j + 3/4)\omega_z$. So in particular the splitting of the modes is equal to $2\omega_z$.

In Fig. 5.4 we show the comparison between the theoretical results of the high-order axial-mode frequency Ω_j and the numerical simulation through the phase-imprinting method, where the mode frequency is extracted by fitting the oscillatory pattern after the imprinting. The deviations are of the order of 5% in the interesting region near $j = 19$, or alternatively, the mode number j is off by 1. This is acceptable considering the fact that the variational model uses a very small number of parameters to describe the dynamics of the whole superfluid. One possible explanation for the deviations is the axial dependence of the mode profile. To investigate, whether this deviation derives from the difference between the theoretical mode function and mode function in the simulation, we used the mode profile from the simulation to calculate T_{jj} from (5.16) and Q_{jj} from (5.17) to calculate an estimate of Ω_j using (5.20). Although these values of Ω_j are

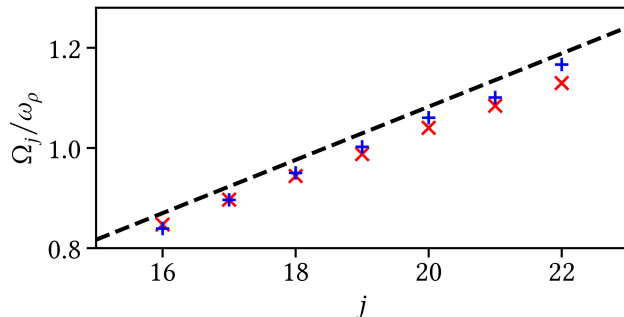


Figure 5.4: High-order axial mode frequency Ω_j in units of ω_p as a function of mode number j . The black dashed line is the theoretical prediction of (5.28), the red times signs (\times) are the frequencies for the simulation data by phase-imprinting and the blue plus signs ($+$) are the frequencies obtained by the integration of the mode function found from the simulation data (as discussed in the text).

closer to values of our theoretical mode function, they still do not fully agree with the theoretical values, presumably due to our assumption of neglecting the radial dependence in the mode profile.

Finally, the Lagrangian L_A of (5.15) contains non-diagonal elements, which we have neglected until now. In principle, these non-diagonal elements Q_{ij} and $\Gamma_{ij}(t)$ can be included in the analysis. Applying the Euler-Lagrange equation including these non-diagonal terms leads to coupling of the form $Q_{j\pm 1,j}$ and $\Gamma_{j\pm 1,j}(t)$. By diagonalizing the resulting equations we find new eigenvectors with almost equal eigenvalues, where the nearest neighbor contribution is less than 5% for our experimental parameters. Therefore, we ignore the non-diagonal effects in the remainder of this article.



5.5 Back-action

In Sec. 5.2 we have concentrated on the part of the Lagrangian density that involves only the higher-order axial modes. However, there is also dynamics in the condensate in the radial direction, and this can be obtained by considering the full Lagrangian density L of (5.3), substituting (5.8) and only retaining terms that are second- or third-order in the density n_A or phase ϕ_A . We obtain for the Lagrangian

$$L = L_D + L_A, \quad (5.29)$$

where L_A is given by (5.15) and the Lagrangian L_D of the condensate is given by

$$L_D = \frac{1}{14} m R_\rho(0)^2 N_0 \left(\dot{b}_x^2 + \dot{b}_y^2 + \frac{1}{\lambda^2} \dot{b}_z^2 - \omega_\rho^2 (b_x^2 + b_y^2 + b_z^2) - \frac{2\omega_\rho^2}{b_x b_y b_z} \right), \quad (5.30)$$

where we applied Eqs. (5.12-5.14). Applying the Euler-Lagrange formalism of (5.26) with respect to the scaling factors b_i for L of (5.29), the equation of motion for b_i with back action of the higher-order axial modes become

$$\ddot{b}_i + \omega_i^2 b_i - \frac{\omega_i^2}{b_x b_y b_z b_i} + \chi \sum_j I_{ij}(t) = 0, \quad (5.31)$$

with $i = \rho, z$ and the back-action parameter $\chi = -7\pi T^{2B} R_z(0)/(2mN_0)$ and

$$I_{\rho j}(t) = Q_{jj} b_\rho b_z \dot{\kappa}_j^2 + \frac{T^{2B} M_{jjj} b_\rho}{m\omega_z^2 b_z} \kappa_j^2 \dot{\kappa}_j, \quad (5.32)$$

$$I_{zj}(t) = \lambda^2 \left(Q_{jj} b_\rho^2 \dot{\kappa}_j^2 - \frac{T^{2B} M_{jjj} b_\rho^2}{m\omega_z^2 b_z^2} \kappa_j^2 \dot{\kappa}_j + \frac{\omega_z^2 T_{jj}}{2b_z^3} \kappa_j^2 \right).$$

In absence of back action of the axial dynamics, (5.31) reduces to the ordinary equations for shape oscillations in a condensate that have already been discussed in Refs. [35–38].

5.6 The space-time crystal Hamiltonian

Although theoretical proposals for time crystals have been discussed in the literature for some time now [23–27], the connection with the present experimental schemes in spin systems have not been established firmly, mainly because the underlying physical description is not known. In the experimental scheme using superfluid bosons [20], this mechanism can be described in detail, as we have shown in Sec. 5.2. One of the open questions in time crystals is their long-term stability. In the spin systems there is a lot of discussion, whether the many-body interactions in the system lead to the stability of the crystal. However, there are also suggestions that time crystals can be stabilized in a so-called prethermal state [12]. In this section we show that our effective Lagrangian predicts a prethermal state, where the Hamiltonian in a rotating frame becomes time independent. We also identify in this Hamiltonian a symmetry, which is broken in the phase transition to the space-time crystal.

In the Lagrangian of (5.25) we substitute for the amplitude κ_j in the rotating frame of the drive

$$\kappa_j = \tilde{\kappa}_j e^{-i\omega_D t/2} + \tilde{\kappa}_j^* e^{+i\omega_D t/2}, \quad (5.33)$$

where we have neglected the third-order term proportional to M_{jjj} . We assume that the breathing mode is weakly excited, such that $b_z = 1$ and $b_x = b_y = 1 + A_D \cos(\omega_D t)$ and only retain terms up to first order in A_D . Since the amplitudes $\tilde{\kappa}_j$ are slowly varying ($|\dot{\tilde{\kappa}}_j/\tilde{\kappa}_j| \ll \omega_D$), we neglect terms proportional to $\dot{\tilde{\kappa}}_j^2$. By substituting (5.33) in (5.25) and applying the rotating-wave approximation, we obtain

$$\begin{aligned} L_A &= \eta \sum_j Q_{jj} \left(\delta_j \omega_D \tilde{\kappa}_j \dot{\tilde{\kappa}}_j^* - \frac{A_D \omega_D^2}{8} [\tilde{\kappa}_j \dot{\tilde{\kappa}}_j + \tilde{\kappa}_j^* \dot{\tilde{\kappa}}_j^*] \right. \\ &\quad \left. - \frac{i\omega_D}{2} [\tilde{\kappa}_j \dot{\tilde{\kappa}}_j^* - \tilde{\kappa}_j^* \dot{\tilde{\kappa}}_j + A_D (\tilde{\kappa}_j \dot{\tilde{\kappa}}_j - \tilde{\kappa}_j^* \dot{\tilde{\kappa}}_j^*)] \right), \end{aligned} \quad (5.34)$$

where we used the approximation $(\omega_D/2)^2 - \Omega_j^2 \simeq \delta_j \omega_D$, with $\delta_j = \omega_D/2 - \Omega_j$.



Using the relation between the Hamiltonian and the Lagrangian

$$H \equiv \sum_j \left(\dot{\tilde{\kappa}}_j \frac{\partial L}{\partial \dot{\tilde{\kappa}}_j} + \tilde{\kappa}_j^* \frac{\partial L}{\partial \tilde{\kappa}_j^*} \right) - L \quad (5.35)$$

the Hamiltonian in the rotating frame becomes

$$H = \eta \sum_j Q_{jj} \left(-\delta_j \omega_D \tilde{\kappa}_j \tilde{\kappa}_j^* + \frac{\omega_D^2 A_D}{8} [\tilde{\kappa}_j \tilde{\kappa}_j + \tilde{\kappa}_j^* \tilde{\kappa}_j^*] \right). \quad (5.36)$$

In the rotating frame the Hamiltonian thus becomes time-independent leading to the stability of the space-time crystal.

In the space-time crystal the time- and space-translation symmetry of the Hamiltonian are broken. To explore the symmetry breaking, it is most convenient to work in second quantization. Note that the condensed state contains phase fluctuations, but the number of condensed atoms is large (of $O(10^7)$) and the model so far is a mean-field description. However, in this section we quantize the Hamiltonian by replacing the amplitudes $\tilde{\kappa}_j$ and $\tilde{\kappa}_j^*$ by the annihilation \hat{a}_j and creation \hat{a}_j^\dagger operator, respectively.

For the quantized Hamiltonian the commutation relation between the creation and annihilation operator $[\hat{a}_j, \hat{a}_j^\dagger] = 1$ needs to be fulfilled, such that the operator $\hat{a}_j^\dagger \hat{a}_j$ determines the number of excitations. For the quantization we replace in (5.36) $\tilde{\kappa}_j$ and $\tilde{\kappa}_j^*$ by

$$\tilde{\kappa}_j \rightarrow q_j \hat{a}_j, \quad \tilde{\kappa}_j^* \rightarrow q_j \hat{a}_j^\dagger, \quad (5.37)$$

where q_j is a j -dependent normalization parameter, which is determined from the Lagrangian in (5.34) by calculating the canonical momentum $\hat{\pi}_j = \partial L / \partial \dot{\hat{a}}_j$ and requiring $[\hat{a}_j, \hat{\pi}_j] = i\hbar$. As a result we find

$$q_j = \sqrt{\frac{\hbar}{\eta Q_{jj} \omega_D}}, \quad (5.38)$$

which we substitute in the Hamiltonian in (5.36) to find the quantized Hamiltonian

$$H = \sum_j \left(-\hbar \delta_j \hat{a}_j^\dagger \hat{a}_j + \frac{\hbar \omega_D A_D}{8} [\hat{a}_j \hat{a}_j + \hat{a}_j^\dagger \hat{a}_j^\dagger] \right), \quad (5.39)$$

where the factor in front of the square brackets acts as a driving parameter.

In (5.39) the $U(1)$ symmetry $\hat{a}_j \rightarrow \hat{a}_j e^{i\theta}$ is broken. As a result, when diagonalizing and solving the system using a Bogoliubov transformation, we find that $\langle \hat{a}_j \hat{a}_j \rangle$ is non-zero. Physically this describes the squeezing of the probability distributions of the conjugate variables \hat{n}_j and $\hat{\phi}_j$ due to the driving process even when $\langle \hat{n}_j \rangle = \langle \hat{\phi}_j \rangle = 0$. The Hamiltonian in (5.39) does have the \mathbb{Z}_2 symmetry $\hat{a}_j \rightarrow -\hat{a}_j$. This discrete symmetry is spontaneously broken when the mode j has a large occupation, indicating that a phase transition has occurred to a phase with $\langle \hat{n}_j \rangle \neq 0$ and $\langle \hat{\phi}_j \rangle \neq 0$, which we identify as the space-time crystalline phase. In the rotating frame this phase can exist for arbitrarily long time, which implies that it is a prethermal phase. Note that the symmetry of the Hamiltonian reflects the fact that the (temporal) phase factor of the space-time crystal is determined by the drive only up to a sign. Choosing one particular sign breaks this Ising symmetry and leads to the formation of the space-time crystal.

5.7 Onset of the space-time crystal

One of the outcomes of the experiment is that the higher-axial modes appear a long time after the excitation [41]. As already discussed in Sec. 5.2, many modes can be excited, but in the experiment only one or a few modes are observed. In this section we exploit the equation of motion of (5.27) to find the frequencies, growth rates and threshold for the higher-order axial modes.

In the experiment, there are certain dissipative processes involved, which have not been included in the model so far. One of the most important dissipation mechanisms occurs through the thermal cloud, although its density is small compared to the condensate. As shown in Ref. [42], by moving through the thermal cloud, excitation in the condensate can be induced, which lead to damping of its motion. We include the damping in



(5.27) by adding a phenomenological damping parameter α ,

$$\ddot{\kappa}_j + \Gamma_{jj}(t)\kappa_j + \left(\frac{\dot{b}_x}{b_x} + \frac{\dot{b}_y}{b_y} + \frac{\dot{b}_z}{b_z} + \alpha \right) \dot{\kappa}_j = 0, \quad (5.40)$$

which assumes that the damping is proportional to the velocity of the condensate. Here we have again neglected the third-order term proportional to M_{jjj} in (5.27) for simplicity.

Since the higher-order axial mode is driven at the radial breathing mode frequency ω_D , and the higher-order axial mode oscillates at nearly one half of this frequency, we substitute (5.33) in (5.40) and only retain non-oscillating terms, which corresponds to the rotating-wave approximation of Sec. 5.6. Since the mode amplitude is nearly constant during one oscillation of the drive, the second-order derivative of $\ddot{\kappa}_j(t)$ can safely be ignored and we obtain

$$\left(-\delta_j - i\frac{\alpha}{2} \right) \tilde{\kappa}_j + A_D \frac{\omega_D}{4} \tilde{\kappa}_j^* = i\dot{\tilde{\kappa}}_j. \quad (5.41)$$

Here we have neglected the back action of the higher-order axial modes on the breathing mode as discussed in Sec. 5.5 and thus assumed A_D to be constant. The solutions are given by $\tilde{\kappa}_j \propto \exp(-i\Delta\Omega_j t)$ with

$$\Delta\Omega_j = -i\alpha/2 \pm \sqrt{\delta_j^2 - (A_D\omega_D/4)^2}. \quad (5.42)$$

In case that the expression under the square-root is positive, the solutions (apart from the term proportional to α) are oscillatory and the frequencies are shifted up and down with respect to $\omega_D/2$. However, if this expression is negative, the frequencies becomes complex and thus lead to gain of the amplitude. There is only gain, when the detuning is not too large with respect to ω_D :

$$|\delta_j| < \frac{\omega_D A_D}{4}. \quad (5.43)$$

Here we assumed that α is much smaller than δ_j . In general, there is gain if the growth due to the driving exceeds the damping and the driving amplitude must be larger than the threshold value A_D^{Th} , which is given by

$$A_D^{\text{Th}} = \frac{4\sqrt{\delta^2 + (\alpha/2)^2}}{\omega_D}. \quad (5.44)$$

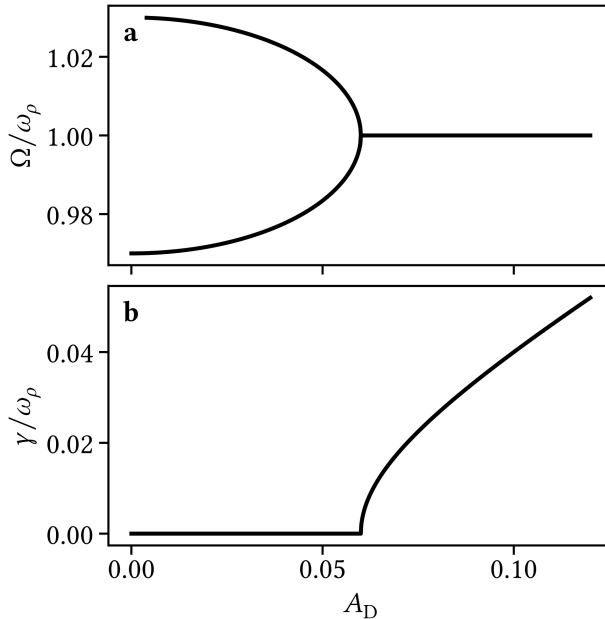


Figure 5.5: (a) The frequency $\Omega = \omega_D/2 + \Delta\Omega_j$ and (b) the growth rate γ in units of ω_p for $j = 19$ as a function of A_D for $\Omega_j = 1.03\omega_p$ and $\omega_D \simeq 2\omega_p$. There is no damping ($\alpha = 0$).

In Fig. 5.5 we show the results for $\alpha = 0$ and non-zero detuning δ . Below the threshold there are two mode frequencies and their splitting decreases if the driving amplitude increases. Above threshold, where the two frequencies coincide, the mode amplitude increases exponentially and the gain coefficient increases nearly linearly with driving amplitude A_D . Note that above threshold the oscillation frequency becomes $\omega_D/2$, which implies that the periodicity of the space-time crystal is twice the periodicity of the drive and the discrete time symmetry is broken.

In Fig. 5.6a we have plotted the threshold as a function of the driving frequency ω_D . In the absence of damping the threshold is zero at resonance and the higher-order axial mode can always be excited. However, for



non-zero damping, which coincides with any realistic experiment, there is a minimum requirement of the driving amplitude, which depends also on the detuning of the mode frequency Ω_j with half the driving frequency $\omega_D/2$. Note that the detuning is not easily adjustable in the experiment, since it depends on Ω_j , which through (5.28) depends in a complicated way on various parameters of the experiment. Increasing the driving amplitude too much causes heating of the condensate and thus leads to a strong reduction of the number of condensed atoms. This makes the observation of the space-time crystal in the laboratory non-trivial, since there is a small window for the driving amplitude for the observation of the higher-order mode. In Fig. 5.6a we have indicated the conditions for the simulations of Sec. 5.3 and from Fig. 5.6a it can be seen that the theoretical model predicts the excitation of predominantly the mode with $j = 18$.

In Fig. 5.6b we have plotted the threshold as a function of the axial trap frequency, where the radial trap frequency and thus the driving frequency is kept constant. We have run the simulations using phase imprinting under the same trapping conditions and analyzed the axial flux of the higher-order axial mode using different mode numbers j . We find the dominant mode from a fit to the simulations by determining the mode j , for which the amplitude in the fit is the largest and simultaneously the reduced chi-squared of the fit is minimal. As can be seen from the fit, the dominant mode is close to the theoretical prediction, although the quantum number j seems to off by 1. This presumably has the same cause as the shift in j in the frequency of the mode (see Sec. 5.3).

On resonance ($\Omega_j = \omega_D/2$), the detuning $\delta_j = 0$ and the growth rate can easily be determined from (5.42):

$$\gamma = \frac{A_D \omega_D}{4} - \frac{\alpha}{2}. \quad (5.45)$$

Hence, for sufficiently small damping the growth rate becomes $\gamma \simeq A_D \omega_D/4$. From the simulations we have determined the growth rate and we typically find values, which are a factor 3 larger. However, in the simulation the excitation is rather strong and presumably no longer in the linear regime, where our model applies.

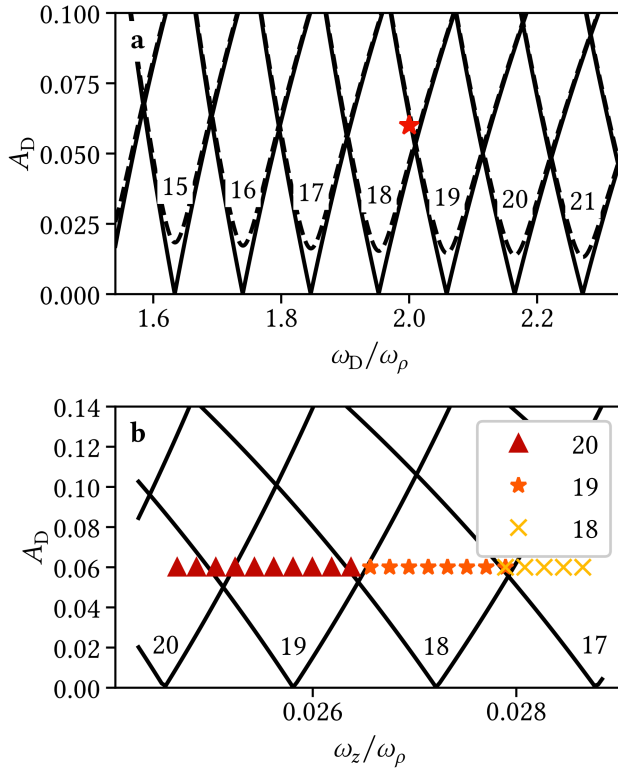


Figure 5.6: (Color online). Linear-response analysis of (a) the threshold of the breathing mode amplitude A_D^{Th} as a function of the radial mode frequency ω_D and (b) as a function of the axial trap frequency ω_z . The results are without damping (solid line) and with damping (dashed line). The red star in (a) indicates the breathing mode amplitude of the simulations of Sec. 5.3. The symbols in (b) indicate the dominant high-order axial mode of the fit for the simulation.



5.8 Conclusion and outlook

In conclusion, we have constructed a variational model that describes the coupling between the radial breathing mode and the higher-order axial modes in a superfluid Bose gas. We have compared the mode profile and the flux of the higher-order modes with numerical simulations and found good agreement. The coupling between these modes leads to the space-time crystal that has recently been observed. Since our model has been constructed from first principles, it allows to investigate the necessary requirements to observe the space-time crystal. In particular, we have identified an Ising-type symmetry breaking, where the symmetry in the sign of the higher-order mode amplitude is broken. The model is used to predict the onset and growth rate of the space-time crystal and we will compare the outcome of the model with the results of experiments in the near future [41].

References

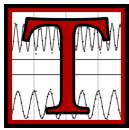
- [1] L. Liao, J. Smits, P. van der Straten, and H. T. C. Stoof, *Phys. Rev. A* **99**, 013625 (2019).
- [2] F. Wilczek, *Phys. Rev. Lett.* **109**, 160401 (2012).
- [3] A. Shapere and F. Wilczek, *Phys. Rev. Lett.* **109**, 160402 (2012).
- [4] P. Bruno, *Phys. Rev. Lett.* **110**, 118901 (2013).
- [5] P. Nozières, *Europh. Lett.* **103**, 57008 (2013).
- [6] H. Watanabe and M. Oshikawa, *Phys. Rev. Lett.* **114**, 251603 (2015).
- [7] L. Guo, M. Marthaler, and G. Schön, *Phys. Rev. Lett.* **111**, 205303 (2013).
- [8] K. Sacha, *Phys. Rev. A* **91**, 033617 (2015).
- [9] D. V. Else, B. Bauer, and C. Nayak, *Phys. Rev. Lett.* **117**, 090402 (2016).
- [10] V. Khemani, A. Lazarides, R. Moessner, and S. L. Sondhi, *Phys. Rev. Lett.* **116**, 250401 (2016).
- [11] C. W. von Keyserlingk, V. Khemani, and S. L. Sondhi, *Phys. Rev. B* **94**, 085112 (2016).
- [12] D. V. Else, B. Bauer, and C. Nayak, *Phys. Rev. X* **7**, 011026 (2017).
- [13] A. Syrwid, J. Zakrzewski, and K. Sacha, *Phys. Rev. Lett.* **119**, 250602 (2017).
- [14] N. Y. Yao, A. C. Potter, I.-D. Potirniche, and A. Vishwanath, *Phys. Rev. Lett.* **118**, 030401 (2017).
- [15] J. Zhang, P. W. Hess, A. Kyprianidis, P. Becker, A. Lee, J. Smith, G. Pagano, I.-D. Potirniche, A. C. Potter, A. Vishwanath, N. Y. Yao, and C. Monroe, *Nature* **543**, 217 (2017).
- [16] S. Choi, J. Choi, R. Landig, G. Kucsko, H. Zhou, J. Isoya, F. Jelezko, S. Onoda, H. Sumiya, V. Khemani, C. von Keyserlingk, N. Y. Yao, E. Demler, and M. D. Lukin, *Nature* **543**, 221 (2017).
- [17] J. Rovny, R. L. Blum, and S. E. Barrett, *Phys. Rev. Lett.* **120**, 180603 (2018).

-
- [18] J. Rovny, R. L. Blum, and S. E. Barrett, *Phys. Rev. B* **97**, 184301 (2018).
- [19] S. Autti, V. B. Eltsov, and G. E. Volovik, *Phys. Rev. Lett.* **120**, 215301 (2018).
- [20] J. Smits, L. Liao, H. T. C. Stoof, and P. van der Straten, *Phys. Rev. Lett.* **121**, 185301 (2018).
- [21] K. Sacha and J. Zakrzewski, *Rep. Progr. Phys.* **81**, 016401 (2018).
- [22] P. Engels, C. Atherton, and M. A. Hoefer, *Phys. Rev. Lett.* **98**, 095301 (2007).
- [23] B. Huang, Y.-H. Wu, and W. V. Liu, *Phys. Rev. Lett.* **120**, 110603 (2018).
- [24] E. Lustig, Y. Sharabi, and M. Segev, *ArXiv e-prints*, 1803.08731 (2018).
- [25] W. W. Ho, S. Choi, M. D. Lukin, and D. A. Abanin, *Phys. Rev. Lett.* **119**, 010602 (2017).
- [26] K. Mizuta, K. Takasan, M. Nakagawa, and N. Kawakami, *ArXiv e-prints*, 1804.01291 (2018).
- [27] A. Russomanno, F. Iemini, M. Dalmonte, and R. Fazio, *Phys. Rev. B* **95**, 214307 (2017).
- [28] K. M. R. van der Stam, E. D. van Ooijen, R. Meppelink, J. M. Vogels, and P. van der Straten, *Review of Scientific Instruments* **78**, 013102 (2007).
- [29] R. Meppelink, R. A. Rozendaal, S. B. Koller, J. M. Vogels, and P. van der Straten, *Phys. Rev. A* **81**, 053632 (2010).
- [30] C. J. Pethick and H. Smith, *Bose-Einstein Condensation in Dilute Gases*, 2nd ed. (Cambridge University Press, 2008).
- [31] H. Stoof, K. Gubbels, and D. Dickerscheid, *Ultracold Quantum Fields* (Springer, 2019).
- [32] L. Salasnich, A. Parola, and L. Reatto, *Phys. Rev. A* **65**, 043614 (2002).
- [33] A. I. Nicolin, R. Carretero-González, and P. G. Kevrekidis, *Phys. Rev. A* **76**, 063609 (2007).
- [34] D. S. Petrov, G. V. Shlyapnikov, and J. T. M. Walraven, *Phys. Rev. Lett.* **85**, 3745 (2000).

-
- [35] Y. Kagan, E. L. Surkov, and G. V. Shlyapnikov, *Phys. Rev. A* **55**, R18 (1997).
- [36] Y. Kagan, E. L. Surkov, and G. V. Shlyapnikov, *Phys. Rev. A* **54**, R1753 (1996).
- [37] F. Dalfovo, C. Minniti, S. Stringari, and L. Pitaevskii, *Physics Letters A* **227**, 259 (1997).
- [38] F. Dalfovo, C. Minniti, and L. P. Pitaevskii, *Phys. Rev. A* **56**, 4855 (1997).
- [39] H. T. C. Stoof, *Journal of Low Temperature Physics* **114**, 11 (1999).
- [40] W. Bao, D. Jaksch, and P. A. Markowich, *J. Comp. Phys.* **187**, 318 (2003).
- [41] A. Groot, “Excitations in hydrodynamic ultra-cold Bose gases”, PhD thesis (Universiteit Utrecht, 2015).
- [42] R. Meppelink, S. B. Koller, J. M. Vogels, H. T. C. Stoof, and P. van der Straten, *Phys. Rev. Lett.* **103**, 265301 (2009).

6 On the long-term stability of space-time crystals

We investigate a space-time crystal in a superfluid Bose gas. Using a well-controlled periodic drive we excite only one crystalline mode in the system, which can be accurately modeled in the rotating frame of the drive. Using holographic imaging we observe the stability of the crystal over an extended period of time and show the robustness of its structure in both space and time. By introducing a fourth-order term in the Hamiltonian we show that the crystal stabilizes at a fixed number of quanta. The results of the model are compared to the experimental data and show good agreement, with a small number of free parameters. The results yield insights in the long-term stability of the crystal, which can only be obtained by the combination of the extended control in the experiment and the nearly ab-initio character of the model. From the model we derive a phase diagram of the system, which can be exploited in the future to study the phase transitions for this new state of matter in even more detail.



THE concept of time crystals was first introduced by Frank Wilczek in 2012 as a novel state of matter, breaking the continuous time translation symmetry in the ground state [2, 3]. This sparked intense discussion on the feasibility of time crystals [4, 5], leading to a no-go proof pertaining to breaking of continuous time translation symmetry in a quantum-mechanical ground state [6]. Therefore, the focus shifted from

This chapter is based on *On the long-term stability of space-time crystals*, J. Smits, H. T. C. Stoof, and P. van der Straten **New J. Phys.** 22, 105001 [1].



breaking the continuous symmetry to breaking a discrete one, introducing the Floquet time crystal. Many proposals have since followed to realize such a Floquet time crystal in different systems [7–22] and several experimental realizations using different systems have been demonstrated [23–29].

In a previous work we presented the observation of a space-time crystal in a cigar-shaped Bose-Einstein condensate (BEC) [28]. By modulating the trap in the radial direction a radial breathing mode is excited. This radial breathing mode in turn acts as the driving force for a collection of axial modes of the cloud, realizing a Floquet time crystal which also exhibits high spatial ordering. In that study it was hard to conclusively show long term stability due to the spurious excitation of additional collective modes and loss of particles due to imaging. In this paper we will show how we have overcome these problems and report on our results.

The paper is organized as follows. In Sec. 6.1 the experimental setup is discussed, with an emphasis on the improvements to the experimental setup and sequence compared to the previous work. In Sec. 6.2 the model of Ref. [30] is expanded with a fourth-order interaction term, which provides insight into the stabilization mechanism bounding the growth of the observed pattern. In Sec. 6.3.1 we explicitly show the broken time-symmetry in our experiment. The updated model is used in Sec. 6.3.2 to relate the growth of the crystal in the experiment to the driving strength, detuning and the value of the fourth-order term. Finally, in Sec. 6.3.3 the saturated amplitude of the space-time crystal for different driving strengths is compared to the model.

6.1 Experiment

In our experiment, a superfluid cloud of sodium atoms is trapped in an elongated magnetic trap, resulting in a cigar-shaped Bose-Einstein condensate. By modulating the trap in the radial direction, a radial size oscillation is induced. In previous work [28] we have demonstrated that this

mode, the radial breathing mode, couples to a higher-order axial mode through a non-linear coupling. The induced higher-order axial mode is shown to satisfy all the requirements of a time crystal, with the addition of also exhibiting spatial ordering.

A bottleneck in previous experiments was the loss of particles as a result of photon scattering during imaging. For this work an imaging method based on off-axis holography was used [31, 32] instead of a phase-contrast imaging method. As a result, the BEC is imaged at comparable signal-to-noise ratio (SNR), but at loss rates a factor of 50 lower than in previous experiments. Bose-Einstein condensates are recorded with a sampling rate of up to 1 kHz, and up to 250 images are taken of a single sample with an approximate total particle loss of less than 20% during the entire imaging sequence.

Further improvements are made to the method by which the sample is prepared and the initial modulation is applied. As the resonance conditions for each axial mode depend on the axial extent (length) of the BEC, the length of the cloud has to be constant to draw conclusions about true single mode long-term stability. In this work, the magnetic trap containing the atom cloud is deformed to the parameters which will be used in the experiment prior to crossing the transition to a Bose-Einstein condensate. Any excitations due to the trap deformation will damp out and thermalize or be quelled by the subsequent cooling process. After the BEC is created, the radial confinement is modulated using a triangular waveform with a period of 10 ms, which is approximately the time-scale associated with the radial trapping frequency, and varying modulation depth. The short driving period and moderate modulation depth ensure the relative amplitude of the oscillation of the length is always less than 2.5%.

The experiments in this work are performed in a cylindrically symmetric magnetic trap with trapping parameters $(\omega_\rho, \omega_z) = 2\pi \times (92.09(2), 5.048(10))$ Hz with about 10^7 particles at a condensate fraction of above 90%. In the experiment the radial breathing mode, which functions as the periodic driving mode, is excited and the sample is left to evolve freely for a variable time after the initial excitation.



After this hold time, a sequence of 250 consecutive images is recorded with a 1.1 ms interval. At this imaging interval we fully resolve the radial breathing mode, which has the highest frequency of the excited collective modes in the system. Each image yields a two-dimensional column-density profile, with one of the radial directions integrated over. After correcting only for displacement and tilt of the sample, the remaining radial direction is integrated out and a line-density profile along the axial direction is constructed for each frame. By collecting all line-density profiles in a two-dimensional (space-time) density plot, the time behavior of the axial modes is visualized (Fig. 6.1a). With the used sampling rate and the number of images taken, we are able to resolve ≈ 30 periods of oscillation of the time crystal in a single measurement. Over the entire measurement run a moderate loss of signal is observed corresponding to particle loss due to imaging. The oscillation of the length of the condensate is in this case less than 1%.

A two-dimensional Fourier transform of the space-time resolved data is shown in Fig. 6.1b. Peaks in a rectangular formation in (f, k) space are observed, the clear signature of space-time crystalline ordering, in analogy with well-known X-ray Bragg spectroscopy on crystals with rectangular lattices. Peaks related to the space-time crystal appear at $f = \pm 90.5$ Hz, $k_z = \pm 0.14 \mu\text{m}^{-1}$. The width of a frequency bin is approximately 3 Hz. No broadening is observed along the frequency axis, implying a very well-defined frequency. Indeed, direct fitting of the driving mode and crystal yield $\omega_D = 2\pi \times 183.26(4)$ Hz and $\omega_X = 2\pi \times 91.61(3)$ Hz, respectively, confirming that within the quoted uncertainty the space-time crystal oscillates with half the drive frequency. Some broadening along the wavevector axis observed for the four peaks associated with the crystalline order is attributed to the inhomogeneous spatial profile, which in turn is a result of the inhomogeneous trap shape. The peak at the center of the Fourier space corresponds to the equilibrium profile and is broadened along the spatial (wavenumber) axis due to the spatial profile of the BEC and along the frequency axis due to particle losses caused by the imaging.

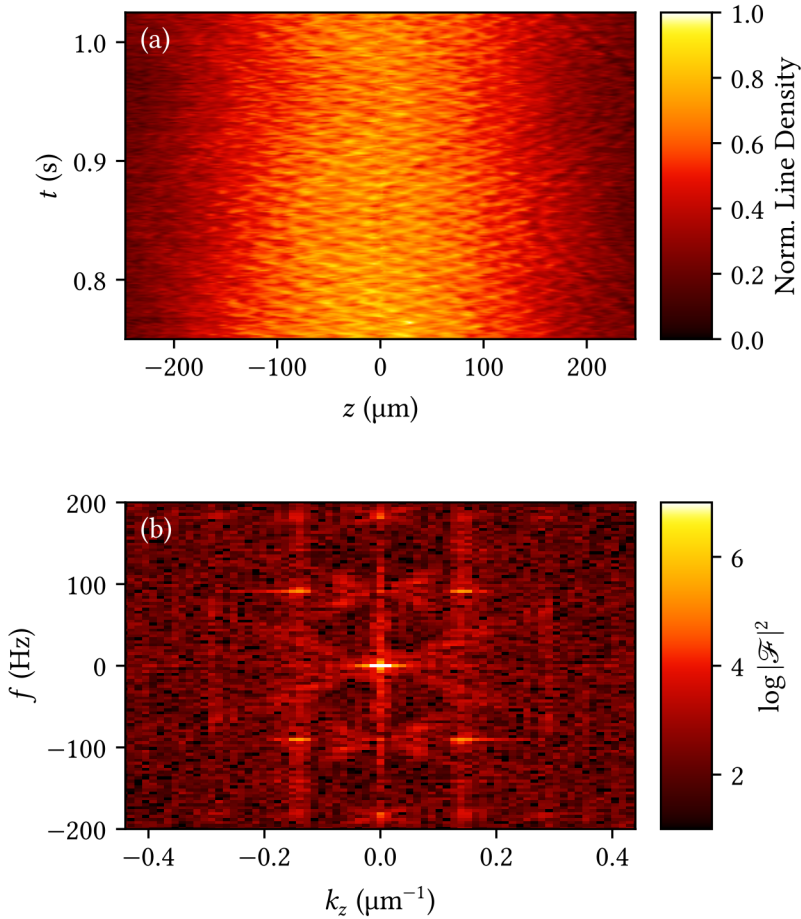


Figure 6.1: (a) Space-time crystal over an extended range of time. The signal strength remains nearly constant over the whole range. The “wavy” pattern is due to center-of-mass motion correction and inhomogeneity of the camera sensor sensitivity. (b) Fourier spectrum of the space-time crystal on a logarithmic scale.

6.2 Modelling

The excitation observed in the experiment is quantified by fitting the column density profile with the sum of a Thomas-Fermi density profile and a higher-order pattern along the length of the cloud, where the density of the latter is proportional to the mode function

$$L_j(\bar{z}) = P_{j+2}(\bar{z}) - P_j(\bar{z}), \quad (6.1)$$

where P_j represent Legendre polynomials and \bar{z} is the coordinate along the axial direction, normalized to the length of, and centered on, the cloud. The Legendre polynomials are chosen as they are the solution of the one-dimensional problem [33]. The difference is taken to make sure boundary conditions are satisfied. Note that the indexing j has been changed compared to previous work [30] to include both even and odd $L_j(z)$ instead of only even modes. In the current work, j alternates between $j = 40$ and $j = 41$ without clear relation to the particle number and condensate length. A fit of this model to a two-dimensional column density profile can be seen in Fig. 6.2.

The dynamics of the space-time crystal were modeled in Ref. [30] up to third order in the crystal mode amplitudes. The model describes the space-time crystal as a single excited mode in a collection of axial modes of the BEC. This model can be reduced, for only one dominant axial mode in the rotating frame of the drive, to

$$\hat{H} = -\hbar\delta\hat{a}^\dagger\hat{a} + \frac{\hbar\omega_{\text{D}}A_{\text{D}}}{8}(\hat{a}^\dagger\hat{a}^\dagger + \hat{a}\hat{a}), \quad (6.2)$$

where δ is the detuning from resonance, ω_{D} is the driving frequency, A_{D} is the relative driving amplitude and $\hat{a}^{(\dagger)}$ is the annihilation (creation) operator of a quantum in the dominant axial mode. This model predicts infinite growth as long as $A_{\text{D}} > 4|\delta|/\omega_{\text{D}}$. However, in the experiment we do not observe infinite growth for the space-time crystal but rather stabilization at some finite amplitude. We therefore expand the model with the only fourth-order term that is resonant in the rotating frame, resulting in

$$\hat{H} = -\hbar\delta\hat{a}^\dagger\hat{a} + \frac{\hbar\omega_{\text{D}}A_{\text{D}}}{8}(\hat{a}^\dagger\hat{a}^\dagger + \hat{a}\hat{a}) + \frac{\hbar g}{2}\hat{a}^\dagger\hat{a}^\dagger\hat{a}\hat{a}, \quad (6.3)$$

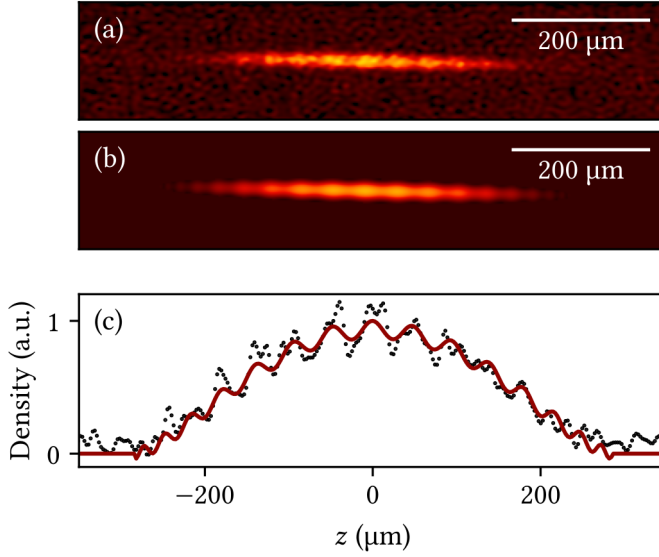


Figure 6.2: A comparison of model and experimental observation of the column density profile. Full column density profile as observed in the experiment (a) and a two-dimension fit on the data (b) using the model in Ref. [30]. (c) A cut through the center of the cloud. The points represent data, the solid line is a fit of the model for $j = 40$.

where $g = g' + ig''$ is a complex-valued parameter capturing all the fourth-order terms not yet calculated in earlier work [30], but which are introduced here in the model as a single phenomenological parameter. This model has been explored previously in a more general context in Ref. [34]. Note that since g can be complex-valued, \hat{H} is not generally Hermitian. If $\langle \hat{a} \rangle \gg 1$, the creation (annihilation) operators can be reinterpreted as classical fields, $\hat{a}^{(\dagger)} \rightarrow a^{(*)}$, and the equations of motion for the fields a and a^* are given by

$$i \frac{d}{dt} a = (-\delta + g|a|^2) a + \frac{\omega_D A_D}{4} a^*, \quad (6.4)$$

$$-i \frac{d}{dt} a^* = (-\delta + g^*|a|^2) a^* + \frac{\omega_D A_D}{4} a. \quad (6.5)$$



Note that $|a|^2$ is then equivalent to the number operator $\hat{a}^\dagger \hat{a}$ and represents the number of quanta in the dominant axial mode. A negative imaginary part of g introduces weak amplitude-dependent dissipation, bounding the maximally attainable amplitude. In Fig. 6.3 the equations of motion are solved for different starting conditions. It takes 100–150 ms for the pattern to be observable as the mode is not observable for low amplitude and growth occurs exponentially. When the real part of g is zero, the final value of $|a|^2$ only relies on the magnitude of the detuning δ , although the growth rate relies on the sign of δ as well. For a non-zero real part of g the final value of $|a|^2$ relies on both sign and magnitude of δ . The maximum value for the number of quanta $|a|^2$ is shifted towards positive δ for positive g' .

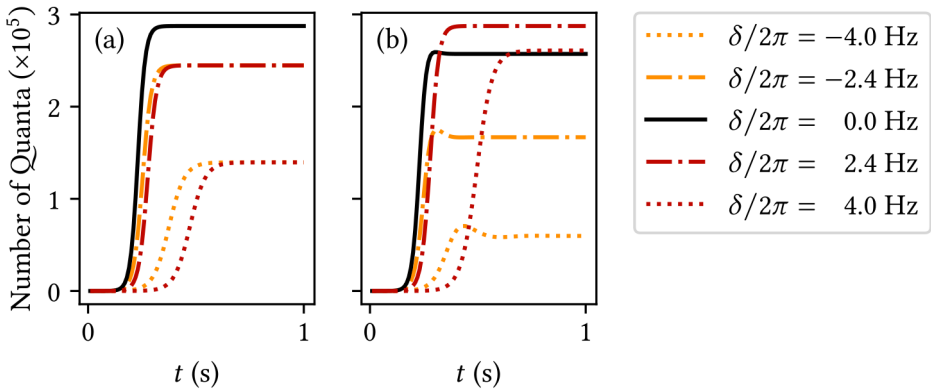


Figure 6.3: Number of quanta as a function of time for $\omega_D = 2\pi \times 183$ Hz, $g'' = 10^{-4} \text{ s}^{-1}$, $A_D = 0.1$ and (a) $g' = 0 \text{ s}^{-1}$ or (b) $g' = 10^{-4} \text{ s}^{-1}$. The dynamics are simulated for up to a second assuming $a = 1$ at $t = 0$. The value $|a|^2$ corresponds to the number of quanta in the crystalline mode.

To further elucidate the behavior of the equation of motion, we can write the evolution of $|a|$ from Eqs. (6.4) and (6.5) close to equilibrium in terms of an

effective potential $V(|a|)$ given by

$$\frac{d^2}{dt^2}|a| = -\frac{d}{d|a|}V(|a|), \quad \text{with}$$

$$V(|a|) = -\frac{1}{2} \left[\left(\frac{\omega_D A_D}{4} \right)^2 - \delta^2 \right] |a|^2 - \frac{g'}{2} \delta |a|^4 + \frac{|g|^2}{6} |a|^6. \quad (6.6)$$

Interestingly, this effective potential is equivalent to a Landau free energy for a system with a tricritical point at $(A_D, \delta) = (0, 0)$ [35]. The extreme values of the potential are found by calculating $\frac{d}{d|a|}V(|a|) = 0$ and are given, for $g \neq 0$, by

$$|a|^2 = \frac{g'}{|g|^2} \delta + \frac{1}{|g|} \sqrt{\left(\frac{\omega_D A_D}{4} \right)^2 - \frac{(g'')^2}{|g|^2} \delta^2}. \quad (6.7)$$

Note that only g with $g'' < 0$, *i.e.* with dissipation, will result in the system relaxing, in the rotating frame, to one of the minima of the potential. For purely imaginary g with $g'' > 0$ super-exponential growth is observed, while $g'' = 0$ results in exponential growth. The real part g' induces an amplitude-dependent frequency shift, which will reduce the amplitude in the final result in the case of finite negative g'' or alternating exponential growth and decay in the case of a purely real g .

Figure 6.4 shows the phase diagram associated with the potential in Eq. (6.6), where only the shaded area supports the existence of a stable space-time crystal. For $g' = 0$, as shown in Fig. 6.4a the phase transition between the non-crystalline and the time-crystalline phase is always smooth and of tri-critical nature and the transition point is found at $|\delta| = \frac{\omega_D A_D}{4}$. Experimentally, this means that the sign of the detuning is irrelevant for how large the crystal amplitude becomes in steady state. The space-time crystal is a single excited mode in a collection of available axial modes, and each of these modes satisfies a similar phase diagram. As every mode has a different detuning with respect to the drive, the mode with the smallest detuning will be present in the experiment as this mode has the highest gain and the highest number of quanta in the equilibrium state.

For $g' > 0$, as shown in Fig. 6.4b the graph is unchanged for $\delta < 0$. However, for $\delta > 0$ the phase transition becomes a (discontinuous) first-order phase



transition and the line is shifted such that now

$$\delta = \left(1 - \frac{3(g')^2}{4|g|^2}\right)^{-1/2} \frac{\omega_D A_D}{4}. \quad (6.8)$$

As opposed to the case $g' = 0$, for non-zero g' and $\delta > 0$ the minimum value for $|a|$ is finite up to the phase transition. The number of quanta is also no longer symmetric with respect to the sign of the detuning, so the mode with the dominant mode is no longer necessarily that with the smallest detuning. It also implies that a change in the parameters such as variation of the detuning δ due to oscillations of the length of the condensate can promptly cause the crystalline state to collapse when, for example, the discontinuous transition threshold is passed.

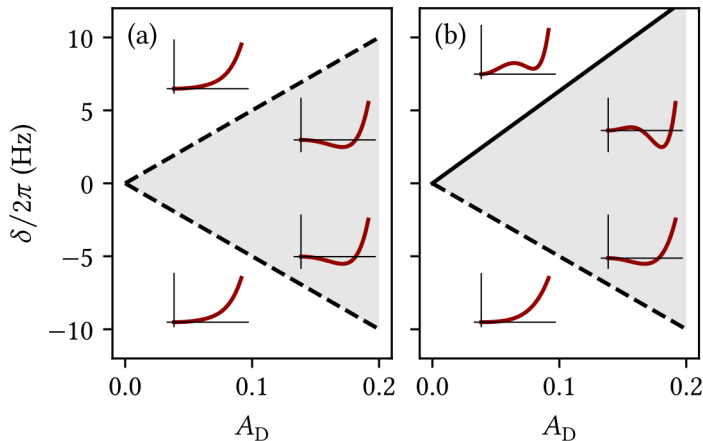


Figure 6.4: Phase diagram as a function of driving amplitude and detuning, associated with the potential in Eq. (6.6) for (a) $g' = 0 \text{ s}^{-1}$ and (b) $g' = 10^{-4} \text{ s}^{-1}$. The other parameters used are $\omega_D = 2\pi \times 200 \text{ Hz}$ and $g'' = -10^{-4} \text{ s}^{-1}$. The shaded area indicates the parameters for which a stable space-time crystal is possible. The striped lines indicate smooth tricritical (left) or second-order (right) phase transitions between the crystalline and non-crystalline state. The solid line indicates a discontinuous first-order phase transition between the crystalline and non-crystalline state. The insets are a schematic representation of the potential of Eq. (6.6) in each region, plotted as a function of $|a|$.

6.3 Experimental results

One of the challenges of the experiment is to excite the periodic (Floquet) drive sufficiently without inducing unwanted excitations. The condensate is trapped in an harmonic trap and in principle the drive, which is the radial breathing mode in our case, can be solely excited by modulating the radial trap frequency quickly. In practice, there are many complications to take into account. First of all, the trap is not purely harmonic and higher-order terms, although small, play a role. Furthermore, there are small imperfections in the



construction of the trap, which lead to coupling between different modes in the trap. So apart from inducing the radial breathing mode, there are dipole modes in the radial and axial direction, a breathing mode in the axial direction and a scissor mode, which are induced simultaneously. In order to minimize the effects of other modes the current through the cloverleaf coils is reduced in a zigzag manner with a modulation depth of $\approx 10\%$ and returned to its original value, within a period of 10 ms. This procedure is repeated a second time, such that the modulation can be kept small. This procedure minimizes the breathing mode in the axial direction, which is beneficial in the analysis of the experiment, since the crystalline mode that is excited depends strongly on the length of the condensate.

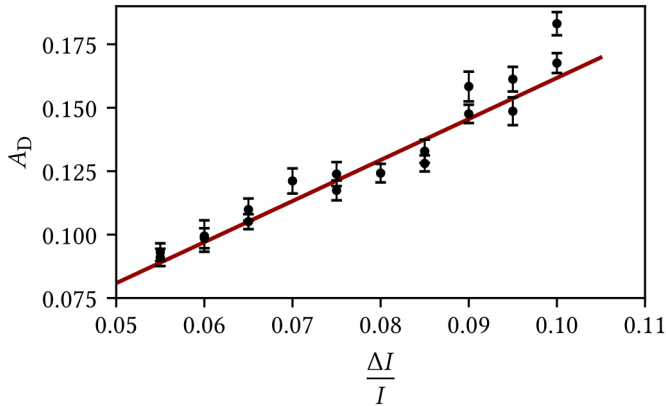


Figure 6.5: The amplitude of the radial breathing mode for different modulation depths $\Delta I/I$ of the cloverleaf current. The amplitude of the breathing mode is 1.572 ± 0.017 times the modulation depth.

In Fig. 6.5 the amplitude of the breathing mode is plotted against the modulation depth, *i.e.*, the relative change $\Delta I/I$ in the current through the cloverleaf coils. The relative driving amplitude A_D is directly proportional to the modulation depth and for the largest modulation depth A_D becomes ≈ 0.17 . Although we can produce modulation depths that are much smaller than a minimum modulation depth of 0.05 in the experiment, the crystalline

mode grows exponentially with a growth rate proportional to A_D and small growth rates produce a detectable crystalline mode that grow in times longer than 1 s. Therefore we have used a minimum modulation depth of 0.05. At the same time the relative amplitude of the axial breathing mode remains below 2.5%, which allows for single mode excitation of the crystal.

To determine which mode has been induced, we first fit the image using the column density of an unperturbed condensate. This fixes the position, length, width, number of particles and angle of the condensate in the images. The number of particles is about 17×10^6 , the length is $291 \mu\text{m}$ and the width is $17 \mu\text{m}$. Next we add a column density $A_X L_j(\bar{z})$ of the crystalline mode to the column density and fit the amplitude A_X leaving the other parameters free. In the fit, the mode number j is varied and the proper mode j is determined using several criteria. First of all, the mode that has the smallest χ_{red} and the largest A_X is selected. In all cases we either find a symmetrical, even mode $j = 40$, or an asymmetrical, uneven mode $j = 41$. Furthermore, it is checked that the position of the condensate in the axial direction is not changed appreciable. For example, an uneven mode has zero density in the center. If the crystalline mode increases the density in the center of the condensate, the fit procedure might shift the condensate to the side in order to minimize χ_{red} , indicating that the proper mode in that case is not uneven. Finally, it is checked that the amplitude A_X displays a sinusoidal oscillation in time, since shifting the condensate might change the sign of the fitted A_X . Only two longitudinal modes have been detected, with $j = 40$ and $j = 41$. It shows that our imaging system has sufficient resolution to distinguish between two adjacent modes, and that our excitation scheme is tailored to excite only one single mode.

The holographic imaging technique allows for the determination of the column density ρ_c of the atomic cloud and due to the cylindrical symmetry of the cloud for the determination of the density ρ . Since the crystalline mode has no radial dependence and the mode only exists within the condensate, the density ρ of the crystalline mode is given by $\rho = \rho_c / (2R_\rho)$ with R_ρ the radial width of the condensate. As shown in Ref. [30] the



density of a crystalline mode containing one quantum is given by

$$q_j = \sqrt{\frac{\hbar\omega_D}{2T^{2B}R_\rho^2R_zQ_{jj}}}, \quad (6.9)$$

where the factor Q_{jj} is a known normalization constant for the overlap of the mode within the condensate. Equation 6.9 allows us to express the amplitude A_X in terms of the number of quanta in the crystalline mode.

6.3.1 Breaking discrete time symmetry

In Fig. 6.6 the amplitude of the breathing mode in the radial direction is shown together with the amplitude A_X of the crystalline mode. From the figure it is immediately clear that the discrete time-symmetry of the periodic drive, the radial breathing mode, is broken and that the crystal oscillates with half the frequency. Note that the amplitudes of both modes are constant and that the crystalline mode is in phase with the breathing mode, although the breathing mode has been excited 0.75 s or nearly 140 periods before. It shows the small damping and large coherence in our superfluid system, where the fraction of thermal atoms is very low ($< 10\%$).

6.3.2 Growth rate

In the experiments the crystalline amplitude A_X is detected for various modulation depths after a hold time of 0.05 and 0.75 s. In the first case, the crystalline mode is only observed for the highest modulation depth of 0.1, whereas in the other case the crystal has already saturated to the final value for most of the modulation depths. Since the density of the crystal is superposed on the density of the condensate and its amplitude is small, the crystal grows quickly from below the detection threshold to its limiting value. Thus we can only observe the growth of the crystal during a small number of oscillations. The result for a hold time of 0.05 s is shown in Fig. 6.7a. The space-time crystal starts growing above the detection threshold

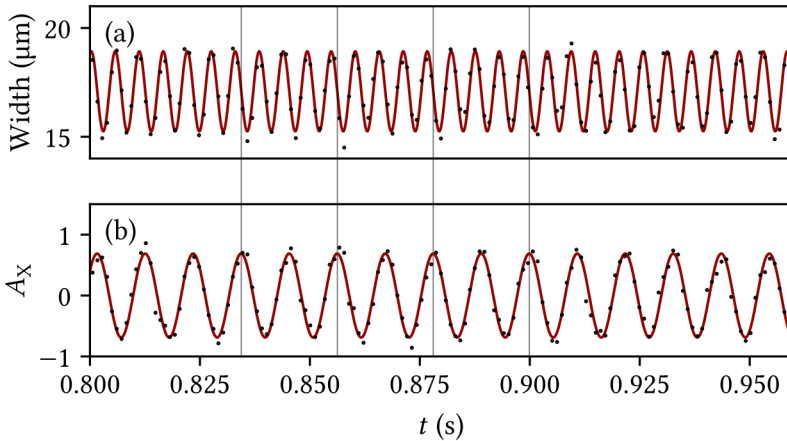


Figure 6.6: The radial breathing mode (a) vs. the crystalline mode (b) for a modulation depth of 0.0675. Here the radial breathing mode has a frequency of 183.26 ± 0.04 Hz. The crystalline mode is $j = 40$ and oscillates at a frequency of 91.61 ± 0.03 Hz, which is within the uncertainty a factor 2 smaller.

about 0.2 s after the excitation. To model the observations it is assumed that the field $a = 1$ at $t = 0$ and the equations of motion from Eqs. (6.4) and (6.5) are used to model the growth using only the detuning δ and g as free parameters. For the driving amplitude A_D as determined from the modulation depth we find $\delta = 3.07$ Hz, indicating that the growth rate is strongly reduced due to the detuning δ . The optimal value of g has a large uncertainty, since the signal is not yet saturated at the end of the measurement.

For a larger holding time of 0.75 s the growth is close to saturation, as shown in Fig. 6.7b. The pattern is shown to grow until $t \approx 0.9$ s, when the pattern saturates and levels out. Again the model is fitted using only δ and g as free parameters. Now $|g|$ is accurately determined with only half of a percent relative uncertainty. It is seen that the model, despite having only a few free parameters, fits the data well. Note that in the model we have assumed that the dominant higher-order term allowed by symmetry is of fourth order,



whereas in principle terms of any even order are possible. Thus the value of g found from the model does not have to correspond exactly to the fourth-order term from the model, since higher-order terms in the Hamiltonian might also contribute to the saturation.

6.3.3 Saturation

One of the key issues in the discussion about time crystals is the long-term stability. In some cases it is argued that the many-body localization plays a crucial role in the stabilization process, whereas in other cases it is shown theoretically that crystals can be stabilized in a so-called pre-thermal phase. Since our system can be described nearly *ab-initio* and a direct comparison between model and experiment is feasible, we can test the requirements for the long-term stability of the space-time crystal in our case. By adding the fourth-order term to the Hamiltonian, the number of quanta in the crystalline mode stabilizes as given by Eq. (6.7). Note that the imaginary part of g provides for damping, whereas the number of quanta becomes purely oscillatory in case the imaginary part of g is exactly zero.

To study the saturation of the number of quanta in the space-time crystal mode, the number of quanta in this mode is studied after 0.75 s for those cases, where the modulation depth is sufficient for the number of quanta to stabilize. The results are shown in Fig. 6.8. As can be seen from the figure, the number of quanta slightly increases for higher modulation depth. This indicates that for the modulation depths used in the experiment the absolute value of the detuning $|\delta|$ is smaller than the driving term $A_D\omega_D/4$ as expected. The expression of Eq. (6.7) is fitted to the data assuming $|g|$ proportional to A_D , which is reasonable given the fact that the fourth-order terms contributing to g are proportional to the deformation of the condensate. The fits yields a value of $\delta = 3.04$ Hz and the value of g is found to be in close agreement with the fit to the data in Fig. 6.7. Thus all experimental data can be explained using the model described in Sec. 6.2 using similar parameters, which lends further credibility to our model.

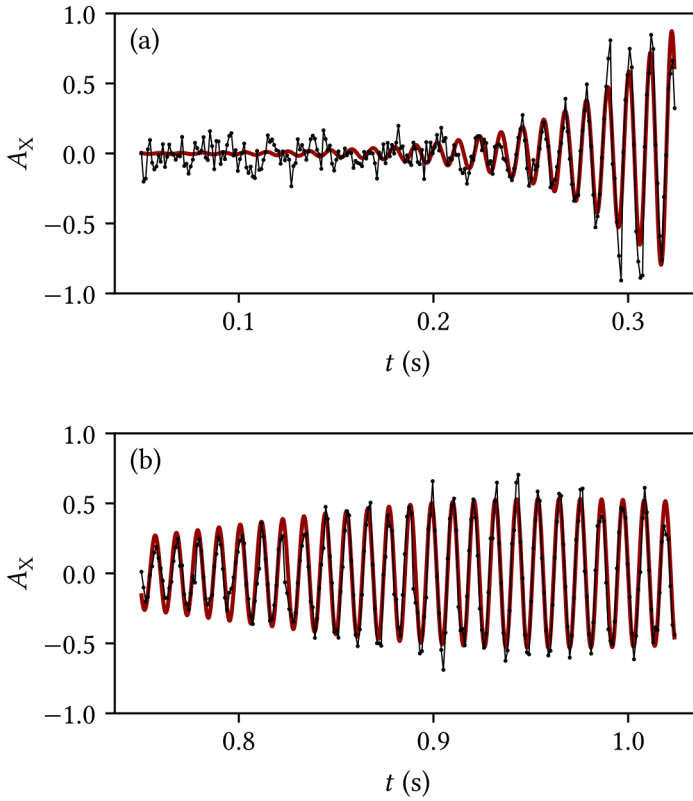


Figure 6.7: Initial growth rate of the space-time crystal pattern. The points represent the amplitude of then mode with $j = 41$ fitted to the data as in Figure 6.2. The line is the model of Eqs. (6.4) and (6.5) with fixed starting conditions $a = 1$, $\delta = 3.07$ Hz, and g , the frequency ω_X and phase as fit parameters. (a) Observation of the growth right after a strong excitation. The space-time crystal appears after approximately 0.2 s. Fitting the model to the data with fixed $A_D = 0.1$ results in $|g| = 0.19(25) \times 10^{-4} \text{ s}^{-1}$. (b) Observation of the growth a long time after a weaker excitation. The pattern is still growing after 0.75 s. Fitting the model to the data with fixed $A_D = 0.072$ results in $|g| = 0.404(2) \times 10^{-4} \text{ s}^{-1}$.



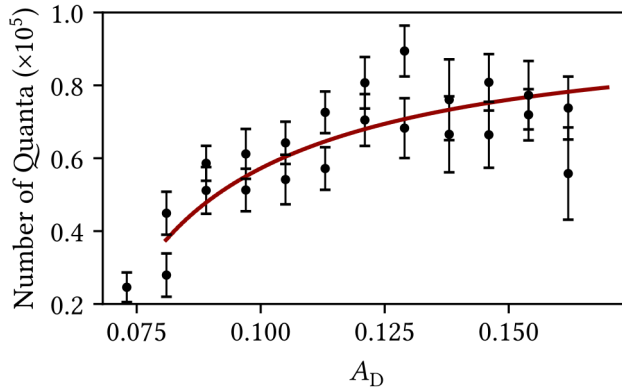


Figure 6.8: The number of quanta in the space-time crystal at saturation, for different drive strengths. The line indicates the maximum possible number of quanta for each drive strength, derived from Eq. (6.7) for fixed $\delta = 3.04$ Hz and fitted $|g|/A_D = 0.48(5) \times 10^{-3} \text{ s}^{-1}$.

6.4 Conclusion and outlook

By deforming the trap during the final stages of the cooling process it is possible to create a Bose-Einstein condensate with large aspect ratio. Radially exciting this BEC realizes a stable Floquet space-time crystal, in which the radial excitation acts as a periodic drive, while the space-time crystal is a higher-order axial mode. Using a minimally destructive holographic imaging method the dynamics of this space-time crystal is studied for 250 recordings or 30 periods of the space-time crystal. By calculating a line-density profile for each recording and studying the behavior of these line-density profiles in time, a pattern periodic in space and time is observed. By calculating the Fourier transform of a time-series of these line-density profiles, a quartet of peaks is observed in a rectangular orientation. The peaks are no more than a pixel wide along the frequency axis, indicating coherence over the entire time of the recording. The rectangular orientation of the peaks is a clear indication of long-range space-time crystalline ordering. The frequency at which the peaks appear corresponds to half the driving frequency, which is confirmed within margin of uncertainty by direct fitting of the crystal amplitude.

To better understand the saturation of the crystal observed in experiments in this work and previous works the original model is expanded with a fourth-order term which has previously been neglected. It is found that addition of this complex-valued fourth-order parameter explains the saturation. Moreover, this fourth-order term leads to an interesting phase diagram exhibiting a tricritical point and both smooth and discontinuous phase transitions.

It is shown that the excitation of the driving mode is in linear relation with the modulation of current through the coils generating the trapping field. By carefully modulating only the coils responsible for the radial trapping frequency the axial size, or length, of the BEC is not disturbed, leading to an oscillation only along the radial direction. The emergent space-time crystal appears at exactly half the frequency of the driving mode and is phase-locked to the driving mode, breaking discrete time translation symmetry. Using the



fourth-order model, the initial growth rate and saturation of the space-time crystal can be adequately described assuming that the fourth-order coefficient is proportional to the amplitude of the driving mode. The model is also used to calculate the saturation amplitude of the space-time crystal for a range of driving mode amplitudes. Good agreement between parameters in the model is found when comparing the growth-rate and saturation data, showing the efficacy of the presented model.

Our system provides an excellent platform for studying space-time crystalline phenomena as the space-time crystal can be very well modeled using a nearly ab-initio model. Minimally destructive imaging can be used to study perturbations of the crystalline phase for an extended period of time. Future work can be directed towards exploring the presented phase diagram, which exhibits a discontinuous phase transition for positive detuning which might support meta-stable space-time crystalline states and therefore hysteresis close to the transition line. It is also possible to introduce a controlled excitation of the length of the condensate, the effect of which should be adequately described using the phase diagram and which might lead to the space-time crystalline ordering appearing and reappearing multiple times over prolonged period of time.

References

- [1] J. Smits, H. T. C. Stoof, and P. van der Straten, *New Journal of Physics* **22**, 105001 (2020).
- [2] A. Shapere and F. Wilczek, *Phys. Rev. Lett.* **109**, 160402 (2012).
- [3] F. Wilczek, *Phys. Rev. Lett.* **109**, 160401 (2012).
- [4] P. Bruno, *Phys. Rev. Lett.* **110**, 118901 (2013).
- [5] P. Nozières, *EPL (Europhysics Letters)* **103**, 57008 (2013).
- [6] H. Watanabe and M. Oshikawa, *Phys. Rev. Lett.* **114**, 251603 (2015).
- [7] L. Guo, M. Marthaler, and G. Schön, *Phys. Rev. Lett.* **111**, 205303 (2013).
- [8] K. Sacha, *Phys. Rev. A* **91**, 033617 (2015).
- [9] V. Khemani, A. Lazarides, R. Moessner, and S. L. Sondhi, *Phys. Rev. Lett.* **116**, 250401 (2016).
- [10] C. W. von Keyserlingk, V. Khemani, and S. L. Sondhi, *Phys. Rev. B* **94**, 085112 (2016).
- [11] D. V. Else, B. Bauer, and C. Nayak, *Phys. Rev. Lett.* **117**, 090402 (2016).
- [12] D. V. Else, B. Bauer, and C. Nayak, *Phys. Rev. X* **7**, 011026 (2017).
- [13] A. Russomanno, F. Iemini, M. Dalmonte, and R. Fazio, *Phys. Rev. B* **95**, 214307 (2017).
- [14] T.-S. Zeng and D. N. Sheng, *Phys. Rev. B* **96**, 094202 (2017).
- [15] Z. Gong, R. Hamazaki, and M. Ueda, *Phys. Rev. Lett.* **120**, 040404 (2018).
- [16] F. Iemini, A. Russomanno, J. Keeling, M. Schirò, M. Dalmonte, and R. Fazio, *Phys. Rev. Lett.* **121**, 035301 (2018).
- [17] K. Mizuta, K. Takasan, M. Nakagawa, and N. Kawakami, *Phys. Rev. Lett.* **121**, 093001 (2018).
- [18] F. M. Gambetta, F. Carollo, M. Marcuzzi, J. P. Garrahan, and I. Lesanovsky, *Phys. Rev. Lett.* **122**, 015701 (2019).
- [19] J. G. Cosme, J. Skulte, and L. Mathey, *Phys. Rev. A* **100**, 053615 (2019).

- [20] T. L. Heugel, M. Oscity, A. Eichler, O. Zilberberg, and R. Chitra, *Phys. Rev. Lett.* **123**, 124301 (2019).
- [21] K. Giergiel, T. Tran, A. Zaheer, A. Singh, A. Sidorov, K. Sacha, and P. Hannaford, arXiv preprint 2004.00755 (2020).
- [22] A. Kuroś, R. Mukherjee, W. Golletz, F. Sauvage, K. Giergiel, F. Mintert, and K. Sacha, arXiv preprint 2004.14982 (2020).
- [23] J. Zhang, P. W. Hess, A. Kyprianidis, P. Becker, A. Lee, J. Smith, G. Pagano, I.-D. Potirniche, A. C. Potter, A. Vishwanath, N. Y. Yao, and C. Monroe, *Nature* **543**, 217 (2017).
- [24] S. Choi, J. Choi, R. Landig, G. Kucsko, H. Zhou, J. Isoya, F. Jelezko, S. Onoda, H. Sumiya, V. Khemani, C. von Keyserlingk, N. Y. Yao, E. Demler, and M. D. Lukin, *Nature* **543**, 221 (2017).
- [25] S. Autti, V. B. Eltsov, and G. E. Volovik, *Phys. Rev. Lett.* **120**, 215301 (2018).
- [26] J. Rovny, R. L. Blum, and S. E. Barrett, *Phys. Rev. Lett.* **120**, 180603 (2018).
- [27] J. Rovny, R. L. Blum, and S. E. Barrett, *Phys. Rev. B* **97**, 184301 (2018).
- [28] J. Smits, L. Liao, H. T. C. Stoof, and P. van der Straten, *Phys. Rev. Lett.* **121**, 185301 (2018).
- [29] N. Träger, P. Gruszecki, F. Lisiecki, F. Groß, J. Förster, M. Weigand, H. Głowiński, P. Kuświk, J. Dubowik, G. Schütz, M. Krawczyk, and J. Gräfe, arXiv preprint 1911.13192 (2019).
- [30] L. Liao, J. Smits, P. van der Straten, and H. T. C. Stoof, *Phys. Rev. A* **99**, 013625 (2019).
- [31] S. Kadlecěk, J. Sebby, R. Newell, and T. G. Walker, *Opt. Lett.* **26**, 137 (2001).
- [32] J. Smits, A. P. Mosk, and P. van der Straten, *Opt. Lett.* **45**, 981 (2020).
- [33] D. S. Petrov, G. V. Shlyapnikov, and J. T. M. Walraven, *Phys. Rev. Lett.* **85**, 3745 (2000).
- [34] Z. R. Lin, Y. Nakamura, and M. I. Dykman, *Phys. Rev. E* **92**, 022105 (2015).

-
- [35] H. Stoof, D. Dickerscheid, and K. Gubbels, *Ultracold Quantum Fields*, Theoretical and Mathematical Physics (Springer Netherlands, 2014).



7 Spontaneous breaking of a discrete time-translation symmetry

SPONTANEOUS symmetry breaking (SSB) is a key concept in physics that for decades has played a crucial role in the description of many physical phenomena in a large number of different areas. In particle physics, for example, the spontaneous symmetry breaking of non-Abelian symmetries provides through the Higgs mechanism the mass of W and Z particles, and introduces the masses of quarks and charged leptons [2–4]. In cosmology, SSB plays a important role in our universe through the different stages of its development, not only during the electro-weak transition just mentioned, but also during inflation [5]. In condensed-matter physics spatial isotropy is broken spontaneously below the Curie temperature to provide a well-defined direction of magnetization to a magnetic material and the phase invariance of the macroscopic wavefunction in superfluid helium is broken below the condensation temperature, to name just two examples [6–8]. SSB is thus an ubiquitous concept connecting several, both “high” and “low” energy, areas of physics and many textbooks describe its basic features in great detail. However, to study the dynamics of symmetry breaking in the laboratory

This chapter is based on the preprint *Spontaneous symmetry breaking in a driven-dissipative system*, J. Smits, H. T. C. Stoof, and P. van der Straten, arXiv:2103.03748 [1].



is extremely difficult. In areas like particle physics and cosmology, the state of matter cannot be studied by changing the control parameter and the symmetry breaking has played its role. In condensed-matter physics tiny external disturbances cause a preference for the breaking of the symmetry in a particular configuration, like a small magnetic field in ferromagnetism, and typically those disturbances cannot be avoided in experiments. Although the latter is not necessary true for a superfluid, the detection of the phase of a superfluid relies on the interferometric observation with another superfluid possessing a well-defined phase, and requires unprecedented phase-stability over long periods. Notwithstanding these complications, here we describe an experiment, in which we directly observe the spontaneous breaking of the temporal phase of a driven system with respect to the drive into two distinct values differing by π .

Consider a domino stone standing on its edge. In a classical world, in the absence of any external perturbation the stone will remain on its edge forever and the situation remains symmetric. In practice, it will eventually always be a small perturbation that pushes the stone either to the left or to the right. The choice for one of two directions is thus not spontaneous in this case. In a quantum world, however, the quantum domino will remain in a linear superposition falling simultaneously both to the left and right and it is not until the domino will be detected that the domino will be found on one of its two sides with exactly equal probability. The symmetry is broken and since there is no force acting on the domino stone to push the stone to a particular side, the symmetry is broken spontaneously. In our experiment we drive a superfluid droplet shaped like a cigar with an oscillatory field, which excites a high-order mode in the long direction of the droplet (see Fig. 7.1). In the experiment a phase lag ϕ appears between the mode and the drive determined by the driving conditions. However, a phase lag of ϕ and $\phi + \pi$ are energetically identical, as the energy depends on the square of the amplitude of the mode. Whether a phase lag ϕ or $\phi + \pi$ is preferred, is thus undetermined at the start of the experiment. These two phases are analogues to the two sides of the domino stone. Since we can detect the shape of the superfluid non-destructively, we can detect all the collective modes of the superfluid as a

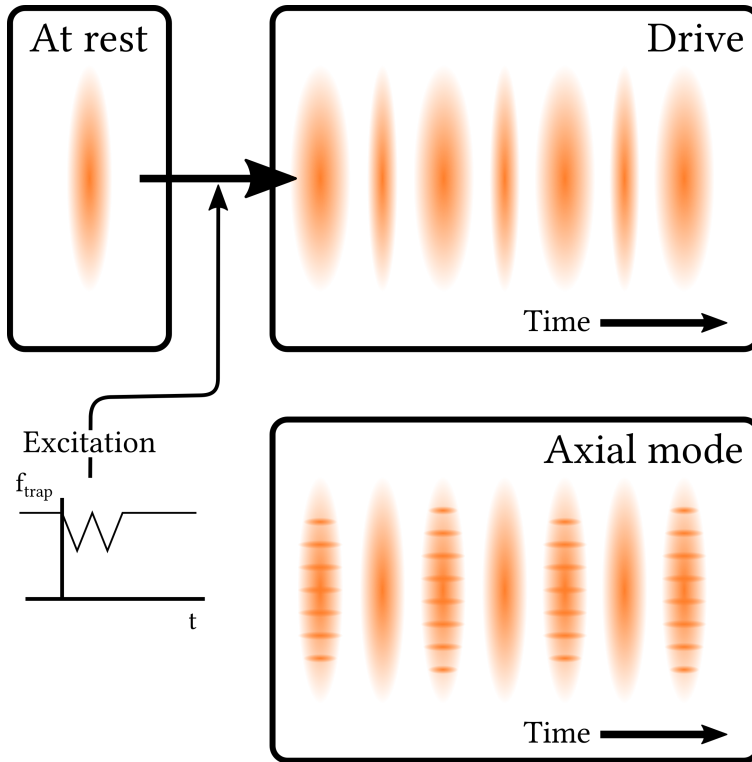


Figure 7.1: Schematic diagram of the experiment. A superfluid droplet at rest is excited by quickly modulating the trap frequency. The superfluid starts oscillating in a breathing mode in the short (radial) direction, which acts as the drive. The drive excites in the long (axial) direction a high-order mode visible as a striped density modulation. The oscillation of the axial mode has a phase delay with respect to the drive, which is determined up to a phase difference of π . This indeterminacy is spontaneously broken in the experiment.

function of time and thus extract the phase lag ϕ for any particular realization of the experiment.

The experiment is conducted in the following way. Cold atoms are trapped in a magnetic trap and evaporatively cooled to temperatures below the critical temperature for Bose-Einstein condensation [9, 10]. The resulting Bose-Einstein condensate is a superfluid and at the temperatures in the experiment, approximately 90% of atoms are condensed leaving 10% as thermal atoms. The thermal atoms induce a small amount of dissipation for excitations in the superfluid. The magnetic trap is harmonic, and the trap frequency in the radial direction is much larger than the trap frequency in the axial direction. The resulting cloud of atoms will thus have an elongated, cigar-like shape. At $t = 0$ the superfluid is excited by modulating the radial trap frequency by quickly ramping the current through the magnetic coils responsible for the radial confinement. This excitation induces a long-lasting oscillation of the radial size (width) of the cloud. The oscillation of the width, which is commonly referred to as the radial breathing mode [11], functions as the drive in the experiment.

Through the non-linearity of the interactions in the superfluid different collective modes of the superfluid become coupled and in particular the drive couples to an axial mode. The drive is weak and as a result the amplitude of the axial mode is small as well. Because the coupling between the two modes is small and the axial mode grows exponentially in time, it is only possible to detect its magnitude after a certain waiting time. After this waiting time we acquire a sequence of nearly non-destructive images of the density of the superfluid using an holographic imaging technique [12]. From the dynamics of the width of the superfluid we can deduce the frequency and phase of the drive with high accuracy. The axial mode is visible as an oscillation of the density profile in the axial direction and from its magnitude in time the frequency and phase of the axial mode are determined. The experiment is repeated approximately hundred times under identical initial conditions to deduce the statistics of the phase lag ϕ between axial mode and drive.

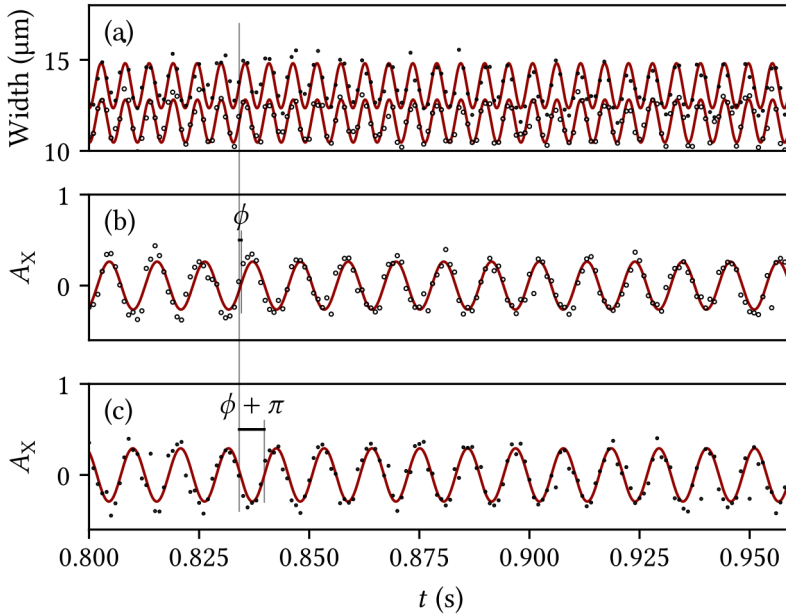


Figure 7.2: Excitation of the modes in the experiment. (a) Radial width of the superfluid as a function of time after the kick. The two data-sets (solid and open dots) are from different sequences, where the sample has been prepared using identical parameters. For clarity, the open dots have been shifted down by $1 \mu\text{m}$. The two curves are adjustments to the data using an oscillatory function and shows the good reproducibility of the drive. (b) and (c) Amplitude of the axial mode (dots) as a function of time after the kick, where the phase lag with the drive differs between the data in (b) and (c) by π . The solid lines are adjustments using an oscillatory function, which clearly shows the period doubling associated with the presence of a discrete time crystal [13, 14].

Figure 7.2 shows the results of two measurements with identical excitation of the drive. In one case the phase lag is ϕ , whereas in the other measurement the phase lag is $\phi + \pi$. The amplitude of the axial mode is determined by fitting the mode profile of the axial mode in each image [15]. Due to the broken discrete time symmetry in our system, the axial mode oscillates with a subharmonic of the drive [13–17]. From the data we can extract the phase lag ϕ , as indicated by the shift of the zero crossing of the two oscillatory patterns. The experiment is repeated using the same parameters and a nearly identical drive is observed owing to the remarkable coherence properties of the superfluid. The axial mode, shown in Fig. 7.2b,c also occurs in a reproducible manner, except for a phase lag difference of π between the two cases. The π phase difference between different realizations is a result of the broken discrete time symmetry that mathematically is identical to a SSB of the \mathbb{Z}_2 (Ising-like) symmetry of the Hamiltonian [15].

In Fig. 7.3 we plot the complex amplitude of the axial mode for different experimental runs using the same parameters for the excitation. The absolute value of the amplitude can be obtained from the experimental results as shown in Fig. 7.2b,c. The phase of the amplitude is determined with respect to the driving amplitude. As the figure clearly shows, the results are binned in two areas, where the absolute values are approximately constant, but the phases differ by π . In total we have 140 experimental runs, and 69 runs have a phase lag close to 0 and 71 runs have a phase lag close to π . As a result, the probability p to obtain a phase lag close to 0 is $p = 0.49 \pm 0.04$, which is a clear signature that the symmetry breaking is indeed spontaneous with $p = 1/2$.

In general, there can be small perturbations (noise) that can also lead to an explicit symmetry breaking. However, in our case the axial mode has a strongly oscillating spatial pattern and a well-defined oscillation frequency. This spatial and temporal pattern is impossible to induce with our magnetic coils, that are located far away from the center of our experiment. Furthermore, from the simulations that we have carried out of the process, as discussed below, we find that the axial mode grows out of an initial state

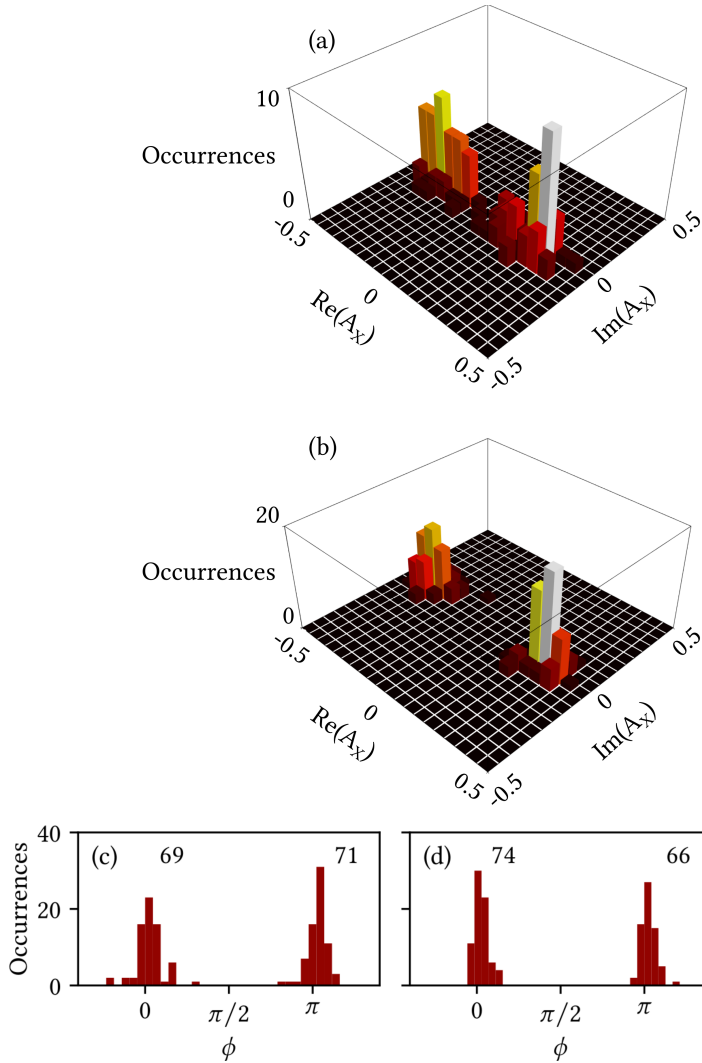


Figure 7.3: The amplitude of the axial mode. (a) Experimental results for 140 runs, where the amplitude is represented in the complex plane with the absolute value proportional to the amplitude of the axial mode and the phase determined by the phase lag ϕ with the drive. (b) Result of the simulation for 140 runs with $\delta = (2.00 \pm 0.75)$ Hz, and $g = (2 \pm 1) \times 10^{-4}$ Hz. (c) and (d) Histogram of the phase lag ϕ of the axial mode with the drive for the experiments and simulation, respectively.



with on the order of fifty quanta reminiscent of thermal fluctuations. In the case of technical noise, the number of induced quanta can have any magnitude. Finally, for technical noise the probability p can be anywhere between 0 and 1 and it is coincidental that its value becomes so close to $1/2$.

In Ref. [15] we have shown that our system can be very well described by the following Hamiltonian:

$$\hat{H} = -\hbar\delta\hat{a}^\dagger\hat{a} + \frac{\hbar\omega_D A_D}{8}(\hat{a}^\dagger\hat{a}^\dagger + \hat{a}\hat{a}) + \frac{\hbar g}{2}\hat{a}^\dagger\hat{a}^\dagger\hat{a}\hat{a}, \quad (7.1)$$

where δ is the detuning from resonance in the rotating frame, ω_D is the driving frequency, A_D is the relative driving amplitude, $\hat{a}^{(\dagger)}$ is the annihilation (creation) operator of a quantum in the axial mode, and $g = g' + ig''$ is a complex-valued fourth-order interaction parameter. This Hamiltonian fully describes our driven-dissipative system, where the drive is given by the term proportional to A_D and the dissipation induced by the thermal cloud is determined by the imaginary part g'' of the parameter g . The Hamiltonian in Eq. (7.1) has a \mathbb{Z}_2 symmetry $\hat{a} \rightarrow -\hat{a}$, but this symmetry is spontaneously broken when $\langle\hat{a}\rangle \neq 0$. Once the system has chosen one particular sign, the “domino” symmetry is broken and leads to the growth of the axial mode amplitude with this sign.

The time-evolution of the probability distribution $P(a^*, a; t)$ of the eigenvalue of the annihilation operator is determined by a Fokker-Planck equation based on the Hamiltonian of Eq. (7.1) [18]. Here, we simulate this numerically in a semi-classical way solving the equations of motion for a and a^* (see Methods). In order to include the fluctuations due to the nonlinear dissipation, we add Stratonovich multiplicative noise with a strength given by g'' and a random phase, as dictated by the fluctuation-dissipation theorem. This yields a random term to the growth with a Gaussian spread. The initial distribution is $P(a^*, a; 0) \propto \exp[-|a|^2/(N + 1/2)]$, where $N = 45$ is the number of initial thermal quanta (see Methods). For the starting value of $a(t)$ we take for each run a random initial value using this distribution. The results are similar to the experimental results, but the spread in the simulation is smaller compared to the spread in the experiment.

Although the experimental runs are performed under identical conditions, there are always small technical fluctuations that contribute to the final result. In the experiment, superfluidity is obtained due to Bose condensation and the preparation of the superfluid droplet leads to fluctuations in the experimental parameters. There are schemes to reduce those fluctuations [19], but this is beyond the scope of the present paper. Here, we can include those technical fluctuations in our simulation by taking the corresponding parameters δ and g Gaussian distributed around their average value, where the spread is small compared to the average value. The results of Fig. 7.3 show that such technical fluctuations in combination with fluctuations due the dissipation can explain the observed width in the experiment. Note that the technical fluctuations ultimately are number fluctuations and these do not break the \mathbb{Z}_2 symmetry. Again the probability p is close to $1/2$, showing that the SSB is well predicted by the simulation and is fully encapsulated in the model.

The simulation allows us to investigate the initial stage of the growth of $\langle |\hat{a}| \rangle$. In Fig. 7.4 we show the individual trajectories for $a(t)$ for only driving the system for 10 periods. Although the initial amplitudes are fully random, all trajectories eventually evolve to either the lower right or upper left of the figure. The division is determined by the drive parameters δ and A_D and the real part of the fourth-order term g . However, all the initial values lying below the dashed line eventually end up at a phase lag $\phi \approx 0$, whereas all initial values above this line end up at a phase lag $\phi \approx \pi$. So on the basis of a Langevin description, the breaking of the symmetry occurs due to the choice of the initial value of $a(0)$ and since this value is chosen randomly, the process is spontaneous. Of course, if the Fokker-Planck equation for $P(a^*, a; t)$ is solved directly, the symmetry is never broken explicitly.

In conclusion, we have observed the spontaneous symmetry breaking of a discrete time translation symmetry. Our experiment breaks the most simple symmetry that can be broken, namely a \mathbb{Z}_2 symmetry, with only two possible outcomes of the experiment. Our space-time crystal is a new state of matter and allows us to further explore this symmetry breaking. For instance, by applying an excitation to the system we can induce tunneling in the system, where the phase lag will tunnel from one value to the other [20]. Another



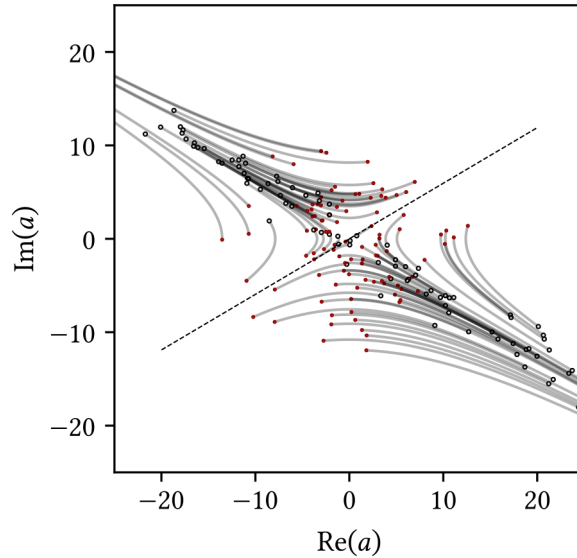


Figure 7.4: Quantum trajectories for the expectation value $\langle \hat{a} \rangle$, where the initial value is shown by the solid dots and the value after 10 periods by the open dots. The dashed line shows the division between initial values, where all points below the line yield a phase lag of ϕ and all points above the line yield a phase lag of $\phi + \pi$. Since the initial phase in the simulation is randomly chosen, the breaking of the symmetry is spontaneous.

possibility is to apply a $\pi/2$ -type pulse to our system and drive the system from a linear superposition of both phase lags to one particular phase lag. This engineering of excitations in space and time is a rich field that requires future experiments to fully exploit all possibilities.

7.1 Methods

7.1.1 Experiment

The superfluid mentioned in the main paper is a Bose-Einstein condensate of sodium atoms. Using a combination of laser cooling and evaporative cooling, a Bose-Einstein condensate of approximately 5×10^6 sodium atoms is created. The sodium atoms are confined in a cylindrically symmetric magnetic trap with effective trapping frequencies $(\omega_\rho, \omega_z) = 2\pi \times (92, 5)$ Hz. Initially the superfluid is at rest in the trap, since the evaporative cooling damps any residual motion in the superfluid due to the interaction with the thermal cloud. For the drive we only want to excite the radial breathing mode, but since all modes are coupled in the superfluid and the magnetic coils are not perfectly symmetric, many modes can become excited during the kick. The kick is induced by modulating the current through the coils providing the radial confinement. This modulation consists of two V-shaped pulses with a modulation depth of 5% and a total duration of 10 ms per pulse. The procedure is optimized in such a way that mainly the breathing mode becomes excited.

In order to detect the different modes, the superfluid is observed using a minimally destructive holographic imaging technique. After a waiting time of ≈ 0.75 s over 250 images are taken, By fitting each image with a Thomas-Fermi distribution, we can determine the position, width, angle and phase shift of the superfluid. Figure 7.5 shows the position, width and angle of the superfluid for one experimental run. In Fig. 7.5ab the position of the superfluid is shown in the radial and axial direction, respectively. The center-of-mass mode is fully decoupled from the other modes (Kohn theorem) in our harmonic trap. However, it does allow for a detection of the trap frequencies and the adjustment of the data to a sinusoidal function yields for this measurement trap frequencies of $\omega_\rho/2\pi = 92.002 \pm 0.005$ Hz and $\omega_z/2\pi = 4.98 \pm 0.03$ Hz.

In Fig. 7.5cd the width of the superfluid is shown. The oscillation of the breathing mode in the radial direction acts as the drive in the experiment. The

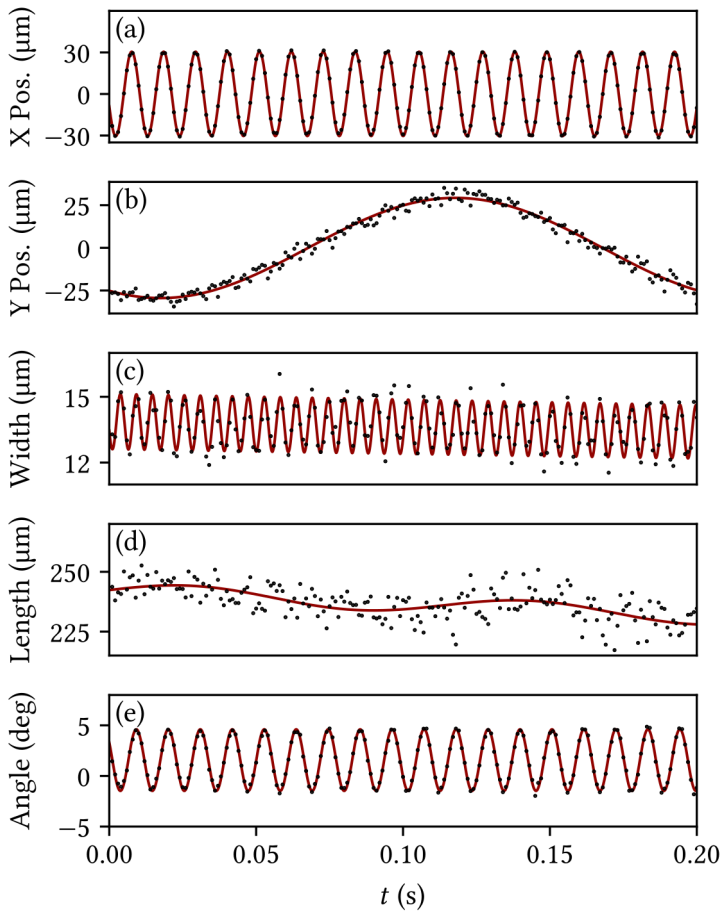


Figure 7.5: Modes of the superfluid. (a) Position of the center of the superfluid in the radial direction. (b) Position of the center of the superfluid in the axial direction. (c) Width of the superfluid in the radial direction. (d) Width of the superfluid in the axial direction. (e) Angle of the superfluid with respect to the detection plane of the camera.

frequency of the radial breathing mode is $\omega_D/2\pi = 183.74 \pm 0.09$ Hz, which is close to twice the frequency of the breathing mode as expected for a trap with a large aspect ratio. In the axial direction the breathing mode frequency is $\omega_B/2\pi = 8.1 \pm 0.2$ Hz, which is close to $\sqrt{5/2}$ of the trap frequency in the axial direction, again as expected for a trap with a large aspect ratio. Note that the amplitude of the breathing mode in the axial mode is very small (2% of the width). If the axial width oscillates strongly in time, the resonance condition for the high-order mode in the axial direction depends on time and thus not one mode becomes excited. In our case, the excitation scheme causes only a single mode to become excited.

In Fig. 7.5e the angle of the superfluid is shown. The angle oscillates in time and this is due to the scissor mode in the superfluid [21]. The scissor mode is a clear sign of the superfluidity in the fluid and the frequency is $\omega_{sc}/2\pi = 91.887 \pm 0.014$ Hz. The frequency of the scissor mode is close to the trap frequency in the radial direction, since the axial frequency is much smaller than the radial frequency. Note that the amplitude of the scissor mode is constant and that the spatial symmetry of the scissor mode is uneven with respect to reflection in the plane containing the long axis of the condensate, and thus does not couple to the high-order axial mode.

In Fig. 7.6 the ratio between the period of the high-order axial mode and the period of the drive is shown for the experimental runs on one day. The figure shows that the ratio is exactly two within experimental uncertainty, as expected for the discrete time crystal [13, 14]. The results show that the SSB experiment can be carried out in a reproducible way over a long period of time.

In the off-axis holography we also detect the phase shift of the center of the superfluid, and together with the width of the superfluid in the axial and radial direction we can determine the total number of atoms in the superfluid. In Fig. 7.7a the number of atoms is shown as function of the time during the detection. The time constant τ for decay due to the imaging is $\tau = 0.93 \pm 0.04$ s, and since the dwell time between images is 1 ms, the loss rate per images is only 0.09%, which is extremely low. In Fig. 7.7b the fluctuations in the

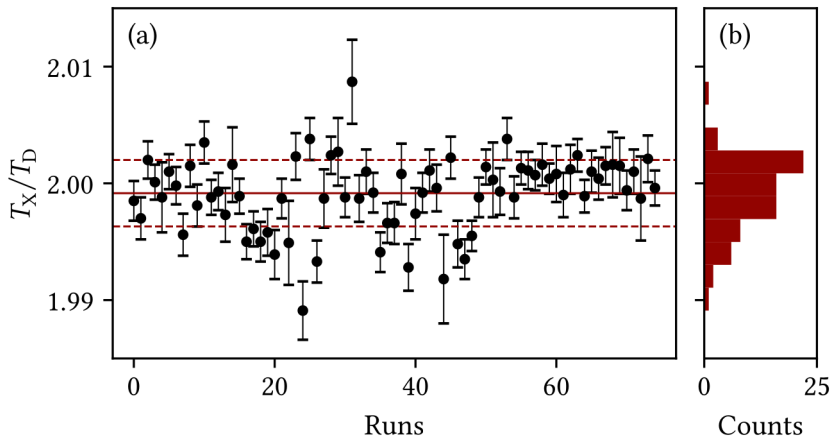


Figure 7.6: The ratio between the period T_X of the high-order axial mode and the period T_D of the drive for all the runs on a day. The ratio is 1.999 ± 0.003 , which is within 1‰ of the factor 2 to be expected for a discrete time-crystal.

imaging between subsequent images is shown, corrected for the exponential decay caused by the imaging. The results show that the statistical uncertainty in the detection technique is 4%, which makes the technique very reliable for imaging the superfluid.

7.1.2 Analysis

From each measurement run, the experimental data is analyzed as described in previous work [15]. The images are fitted with a function which contains the density profile of the high-order axial mode. From the fit we obtain the position and widths of the cloud, and the amplitude A_X of the axial profile, for which the results are shown in Fig. 7.2. From the fit of the breathing mode, we choose a zero crossing of the oscillation with positive ramp at a time t_0 after a fixed number of oscillations after the kick. We identify the zero crossing in the fit of the axial mode closest to t_0 and determine the phase lag ϕ based



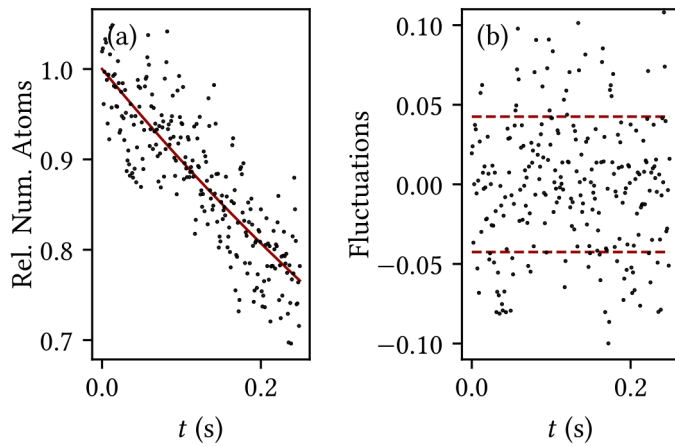


Figure 7.7: Number for atoms in the superfluid. (a) Total number of atoms in the superfluid as a function of time during the imaging. The number of atoms exponentially decreases with a time constant determined by the imaging technique. (b) Fluctuation of the number of atoms as a function of time.

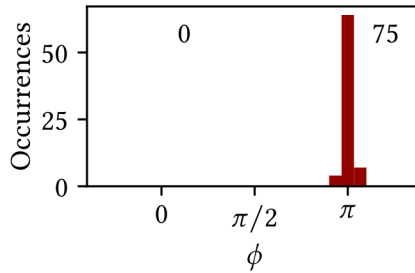


Figure 7.8: Histogram of the phase lag between the scissor mode and the drive.

on the time between the zero crossing and t_0 . In case of a zero crossing with negative ramp, we add an additional factor π to the phase lag. This method properly takes into account the difference between ω_D and $2\omega_X$ in the fit.

To rule out the possibility that the high-order axial mode is driven by the scissor mode, we have determined the phase lag of the scissor mode with respect to the drive using the same method. The scissor mode is found to be always pinned at approximately a phase lag of π , as shown in Fig. 7.8. This precludes the possibility that the scissor mode drives the high-order axial mode.

7.1.3 Number of quanta

The high-order axial mode is quantized, as shown in Ref. [17]. The density of the mode $n_X(z, t)$ in the axial direction is given by $n_X(z, t) \equiv -\dot{\kappa}(t)L_j(\bar{z})$, where the dot represents the time-derivative and $L_j(\bar{z}) = P_j(\bar{z}) - P_{j-2}(\bar{z})$ is the mode profile and j the mode number. Here $\bar{z} = z/R_z$ is the reduced distance in the z -direction with R_z the Thomas-Fermi width and $P_j(\bar{z})$ are Legendre polynomials of order j . It is assumed that there is no dependence of the mode in the radial direction and that the density of the axial profile is only non-zero, where the superfluid has a non-zero density. In the frame rotating with the drive frequency ω_D , the amplitude $\tilde{\kappa}$ can be related to



the annihilation operator \hat{a} using $\tilde{\kappa} = q\hat{a}$, where $q = \sqrt{\hbar/(\eta Q\omega_D)}$ is the normalization parameter. Here Q is the overlap of the mode function,

$$Q = \int_{-1}^{+1} d\bar{z}(1 - \bar{z}^2)L_j(\bar{z})^2,$$

and $\eta = \pi T^{2B} R_\rho R_z$ is the effective mass parameter. Using the experimental parameters the density modulation for one quantum in the axial mode becomes 1.03×10^{15} atoms/m³, which is far too small to be observable in our setup. However, the axial mode grows exponentially in time and after a wait time of about 1 s, the density modulation has become sufficiently large to be observable. This analysis allows us to scale the value of a from the simulation to the amplitude A_X and plot its value in Fig. 7.3. The density modulation is proportional to the time-derivative of κ and thus we have to add a factor $\pi/4$ to the phase of κ to compare our results with the experimental values.

7.1.4 Initial number of quanta

The initial number of quanta N in the axial profile is determined by the thermal fraction of this mode, as determined by the Bose-Einstein distribution. The temperature of the thermal cloud is in our case $T \approx 200$ nK and the energy of the mode becomes $\hbar\omega_X$, where $\omega_X/2\pi = 92$ Hz is the frequency of the high-order axial mode. So the number of quanta becomes $N_{\text{init}} = 45$, which is much larger than the quantum fluctuation of $1/2$.

7.1.5 Fluctuations in the growth

The semi-classical analysis starts with the equations of motion for $a(t)$ and $a(t)^*$ as given in Ref. [15]:

$$i\frac{d}{dt}a = (-\delta + g|a|^2)a + \frac{\omega_D A_D}{4}a^*, \quad (7.2)$$

and the complex conjugate for $a^*(t)$. In order to include the fluctuations we have to include multiplicative noise $\eta(t)a^*(t)$ with $\langle \eta^*(t)\eta(t) \rangle = D\delta(t - t')$

in the model, where D in our case is given by $D = 2\hbar(N_{\text{fluc}} + 1/2)g''$ as determined by the fluctuation-dissipation theorem. Here, N_{fluc} accounts for the increase of noise due to thermal fluctuations. Its value is estimated by first determining the oscillation frequency ω_{eff} in the effective potential $V(|a|)$, as given in Eq. (7) of Ref. [15]. Given our experimental parameters we find $\omega_{\text{eff}} = 8.5$ Hz and assuming that our system is in equilibrium with the thermal cloud at a temperate $T = 200$ nK, the number of quanta becomes $N_{\text{fluc}} = 456$.

To include the fluctuations to the model we add a stochastic noise term $a^*(t)\sqrt{D/\Delta t}x_i$ to Eq. (7.2) and the complex conjugate to the equation for $a^*(t)$ with Δt the step-size in time in the integration. Here, x_i is a Gaussian-distributed complex variable with unit absolute value, which is randomly selected for each time step.

7.1.6 Dependencies on system parameters

To exclude the possibility of the phase being pinned at either ϕ or $\phi + \pi$ by some underlying phenomena related to particle number, mode function or a date-specific parameter, the data set has been split in two parts along different criteria, see Fig. 7.10. Fig. 7.10a shows the same histogram as in the main paper. The chance to get phase ϕ is calculated from the data as $p = N_0/(N_0 + N_\pi)$, with uncertainty $\sigma_p = \sqrt{p(1-p)/(N_0 + N_\pi)}$. For the full data set, this results in $p = 0.49 \pm 0.04$. Figure 7.10bc show the data split by particle number. In Fig. 7.10b, all data points with a particle number below the median particle number are taken, which results in $p = 0.51 \pm 0.06$. In Fig. 7.10c, all data points with a particle number above the median particle number are taken, which results in $p = 0.47 \pm 0.06$. As calculated probabilities are within a margin of error of $p = 1/2$, the particle number does not appear to prefer one solution for the phase over the other. Figure 7.10de show the data split by mode number (see Sec. 7.1.3). In Fig. 7.10d, all data points with an odd mode are shown, which results in $p = 0.41 \pm 0.07$. In Fig. 7.10e, all data points with an even mode are shown, which results in $p = 0.55 \pm 0.05$. For odd modes, the calculated probability deviates from $p = 1/2$ with a margin of error which is a little large than one standard deviation, however, the number of



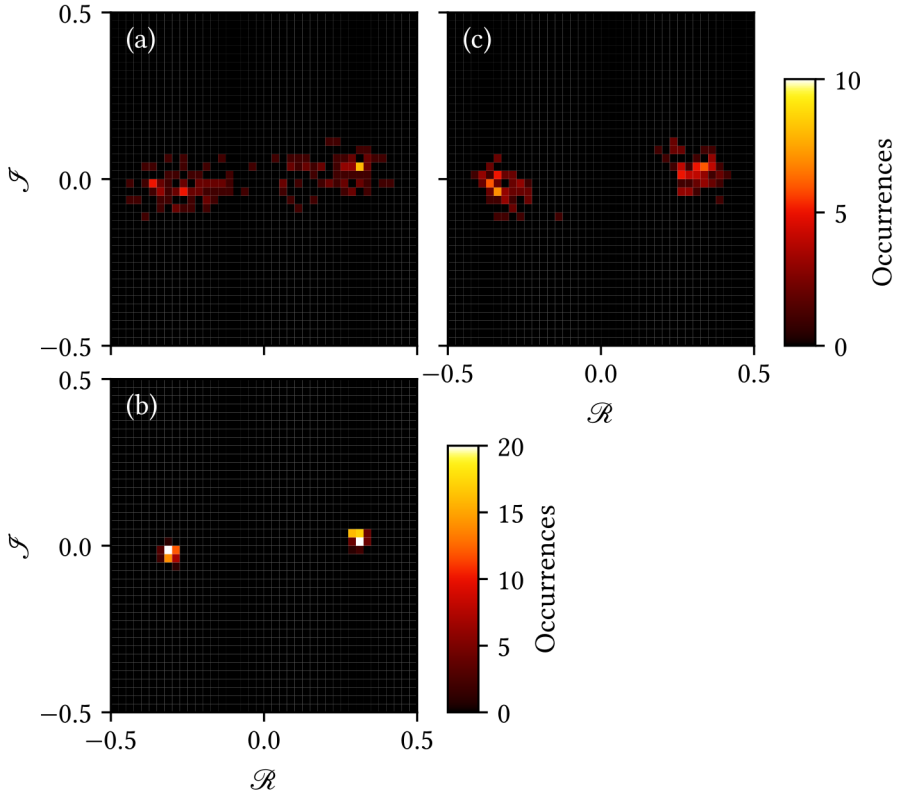


Figure 7.9: Comparison between the experiment and the simulations for the high-order axial mode amplitude A_X . In each case the histogram contains 140 runs. (a) Contour plot of the results of the experiments. (b) Contour plot of the simulations, where only the thermal fluctuations are taken into account. (c) Contour plot of the simulations, where both the thermal and technical fluctuations are taken into account.

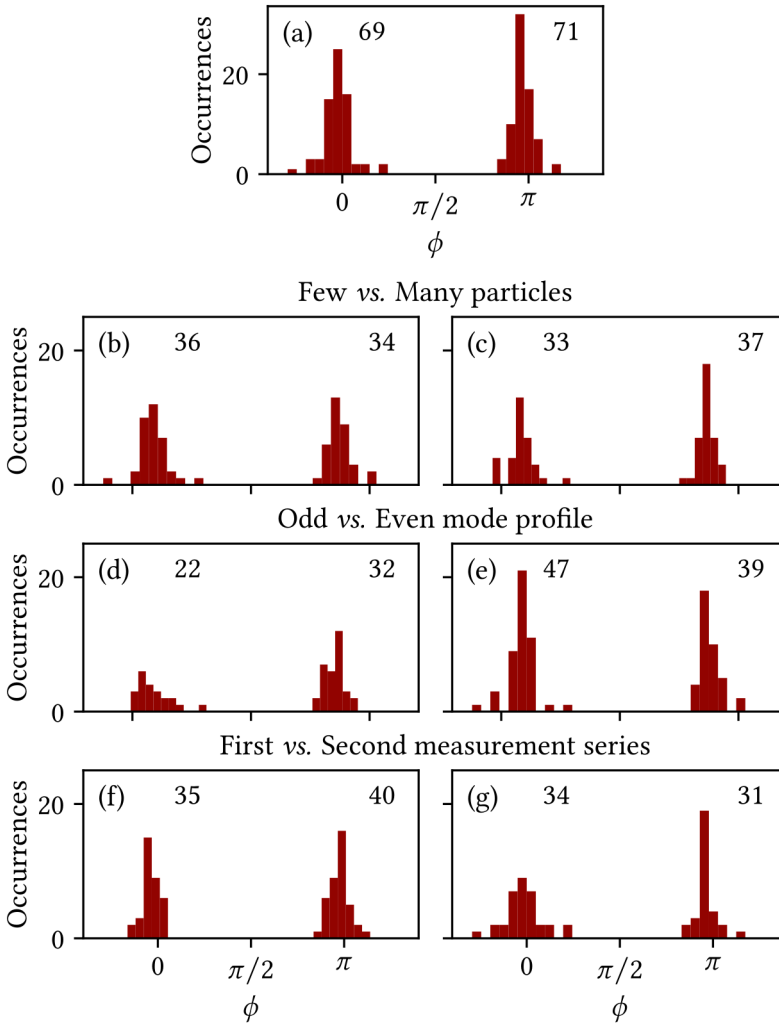


Figure 7.10: Histogram of the phase with data split in different ways. By splitting the data set it is excluded that ϕ or $\phi+\pi$ is more prevalent in certain subsets of the data set. It is seen that, cutting the data set into approximately equal pieces does not disturb the 50/50 balance. (a) Full data set. (b,c) Data set split into less (b) and more (c) particles than the median number of particles in the BEC. (d,e) Data split into odd (d) and even (e) modes, as described in previous work [15]. (f,g) First (f) and second (g) measurement series.

data points is small. Finally, since data was acquired on two separate days, the data set was split in Fig. 7.10fg by measurement series. Data acquired on the first day is shown in Fig. 7.10f. Analysis of this data results in $p = 0.47 \pm 0.06$. Data acquired on the second day is shown in Fig. 7.10g. Analysis of this data results in $p = 0.52 \pm 0.06$. From this it is concluded that from day to day there no preference between either the ϕ or $\phi + \pi$ solutions.

Note added after completion of this work: In the appendix of Ref. [22] we have found in the Methods section also experimental results for the breaking of a different \mathbb{Z}_2 symmetry in a driven-dissipative system.



References

- [1] J. Smits, H. T. C. Stoof, and P. van der Straten, arXiv preprint 2103.03748 (2021).
- [2] L. H. Ryder, *Quantum Field Theory*, 2nd ed. (Cambridge University Press, 1996).
- [3] A. Zee, *Quantum Field Theory in a Nutshell* (Princeton U. Press, 2003).
- [4] J. I. Kapusta and C. Gale, *Finite-Temperature Field Theory: Principles and Applications*, 2nd ed., Cambridge Monographs on Mathematical Physics (Cambridge University Press, 2006).
- [5] P. F. Kiskak, ed., *Symmetry Breaking & Symmetry in Cosmology*, 1st ed. (CreateSpace Independent Publishing Platform, 2016).
- [6] J. Negele and H. Orland, *Quantum Many-Particle Systems*, 1st ed. (CRC Press, 1998).
- [7] P. M. Chaikin and T. C. Lubensky, *Principles of Condensed Matter Physics* (Cambridge University Press, 1995).
- [8] H. Stoof, D. Dickerscheid, and K. Gubbels, *Ultracold Quantum Fields, Theoretical and Mathematical Physics* (Springer Netherlands, 2014).
- [9] M. H. Anderson, J. R. Ensher, M. R. Matthews, C. E. Wieman, and E. A. Cornell, *Science* **269**, 198 (1995).
- [10] M.-O. Mewes, M. R. Andrews, N. J. van Druten, D. M. Kurn, D. S. Durfee, and W. Ketterle, *Phys. Rev. Lett.* **77**, 416 (1996).
- [11] S. Stringari, *Phys. Rev. Lett.* **77**, 2360 (1996).
- [12] J. Smits, A. P. Mosk, and P. van der Straten, *Opt. Lett.* **45**, 981 (2020).
- [13] D. V. Else, C. Monroe, C. Nayak, and N. Y. Yao, *Annual Review of Condensed Matter Physics* **11**, 467 (2020).
- [14] K. Sacha and J. Zakrzewski, *Rep. Progr. Phys.* **81**, 016401 (2018).
- [15] J. Smits, H. T. C. Stoof, and P. van der Straten, *New Journal of Physics* **22**, 105001 (2020).

-
- [16] J. Smits, L. Liao, H. T. C. Stoof, and P. van der Straten, *Phys. Rev. Lett.* **121**, 185301 (2018).
- [17] L. Liao, J. Smits, P. van der Straten, and H. T. C. Stoof, *Phys. Rev. A* **99**, 013625 (2019).
- [18] H. T. C. Stoof and M. J. Bijlsma, *Journal of Low Temperature Physics* **124**, 431 (2001).
- [19] M. A. Kristensen, M. Gajdacz, P. L. Pedersen, C. Klempt, J. F. Sherson, J. J. Arlt, and A. J. Hilliard, *Journal of Physics B: Atomic, Molecular and Optical Physics* **50**, 034004 (2017).
- [20] X. Yang and Z. Cai, *Phys. Rev. Lett.* **126**, 020602 (2021).
- [21] D. Guéry-Odelin and S. Stringari, *Phys. Rev. Lett.* **83**, 4452 (1999).
- [22] H. Kessler, P. Kongkhambut, C. Georges, L. Mathey, J. G. Cosme, and A. Hemmerich, arXiv preprint 2012.08885 (2020).



Nederlandse samenvatting



DE verschillende fasen waarin een materiaal zich kan bevinden en de faseovergangen tussen deze fasen zijn al sinds het begin van de geschiedsschrijving één van de fascinaties geweest van wetenschappers. In de oudheid bediscuseerden Griekse filosofen wat materie precies is. Later, in de 18^{de} en 19^{de} eeuw onderzochten wetenschappers of moleculen, combinaties van de ondeelbare atomen, de bouwstenen zijn van alle materie. Zij dachten dat moleculen in drie fasen kunnen bestaan: gas, vloeibaar en vast. Om tussen deze fasen te wisselen varieerde men de temperatuur of de druk. Met water als voorbeeld: wanneer we op kamertemperatuur beginnen en afkoelen, verandert het water op 0 °C van een vloeistof in een kristallijne vaste stof. Deze faseovergang, van de ene fase naar de andere, is bij iedereen bekend, maar wat er gebeurt is eigenlijk best merkwaardig. De temperatuur wordt gelijkmatig verlaagd, zonder plotse stappen, maar de ordening in het materiaal verandert in een plotse stap van een vloeistof waarin alle deeltjes vrij rond kunnen bewegen, naar een vaste stof waarin de deeltjes in een kristalrooster zijn vastgezet. Deze veranderingen in materiaaleigenschappen zoals dichtheid of ordening als gevolg van veranderingen in externe parameters zoals temperatuur of druk, zijn karakteristiek voor faseovergangen. Er zijn, sinds de vroegste dagen van de wetenschap, veel nieuwe fasen ontdekt, waaronder geïoniseerd plasma, het quark-gluon plasma bij de Large Hadron Collider en het Bose-Einstein condensaat. Deze laatste, het Bose-Einstein condensaat, is waar dit proefschrift over gaat.



Geschiedenis van de Bose-Einstein condensatie

Toen Satyendra Nath Bose de theorie ontwikkelde die later de grondslag zou zijn voor de Bose-Einstein statistiek, probeerde hij geen nieuwe fase te beschrijven, maar een verduidelijking van de wet van Planck [1] te geven. Omdat het niet lukte zijn werk te publiceren, nam hij, in een poging samen te werken, contact op met Albert Einstein. Als hij Einstein zou kunnen overtuigen, dan zou hij zijn werk gepubliceerd kunnen krijgen. Einstein hielp Bose om zijn werk gepubliceerd te krijgen [2], maar realiseerde zich ook, dat de theorie die Bose alleen op lichtdeeltjes toepast ook goed zou werken op de deeltjes in een ideaal gas. In zijn werk *Quantentheorie des einatomigen idealen Gases* uit 1924 [3] leidde Einstein alle thermodynamische relaties af die volgden uit de nieuwe statistiek van Bose. Toen hij in 1925 nog een keer op het onderwerp terugkwam [4], leidde hij af dat volgens deze theorie het systeem maar een eindige capaciteit zou moeten hebben voor thermische deeltjes. Dit impliceert dat wanneer het totale aantal deeltjes groter is dan de capaciteit voor thermische deeltjes, de overgebleven deeltjes een “condensaat” van deeltjes zouden vormen in de laagste energietoestand. Een nieuwe fase van materie! Aangezien de capaciteit voor thermische deeltjes afhangt van de temperatuur, suggereert dit dat er een kritische temperatuur is waarop het aantal deeltjes de capaciteit voor thermische deeltjes zal overschrijden. Vervolgens liet men zien dat de kritische temperatuur voor de faseovergang van een thermisch gas naar een Bose-Einstein condensaat ongeveer gelijk was aan de temperatuur waarop de thermische golflengte van de deeltjes gelijk is aan de gemiddelde afstand tussen de deeltjes.

In de tijd dat deze nieuwe fase voorspeld werd, was het enige toegankelijke Bose-Einstein condensaat Helium-II. Vloeibaar helium, afgekoeld tot onder de kritische temperatuur (het λ -punt, op 2.18 Kelvin), gedraagt zich als een supervloeistof. Wanneer men in een supervloeistof roert ontstaat niet één grote draaiklok, maar een heel rooster van kleine draaikolkjes. In het algemeen is een Bose-Einstein condensaat met interacties tussen de deeltjes een supervloeistof: een vloeistof die langs obstakels kan stromen zonder op



te warmen. Helium-II gedraagt zich als een supervloeistof, maar door de sterke interacties tussen de deeltjes is het een moeilijk systeem om theoretisch te beschrijven. Het Bose-Einstein condensaat kan beschreven worden als een quantummechanische golf functie, afhankelijk van alle deeltjes in het condensaat. Als de afstand tussen de deeltjes voldoende groot is, is het mogelijk om een *mean field* benadering te doen. De quantummechanische golf functie van het hele condensaat wordt dan benaderd door het product van identieke golf functies behorende bij een enkel deeltje. Het condensaat kan dan beschreven worden door een quantummechanische golf functie alsof het één enkel deeltje is [5, 6]. Wanneer twee van deze Bose-Einstein condensaten zich vermengen kan dan ook een interferentiepatroon waargenomen worden. De golf functies van beide condensaten tellen dan op, of juist niet, op basis van de lokale fase, net als lichtgolven of golven op water.

Temperaturen in de orde van nanokelvins, vlakbij het absolute nulpunt, zijn nodig om de kritieke temperatuur voor BEC te bereiken in ultra-koude atoomgassen. Het bereiken van deze temperaturen was in de jaren '30 van de 20^{ste} eeuw verre van mogelijk. Voortgang op het gebied van koude atomen maakte uiteindelijk de eerste BECs in deze systemen mogelijk. Atomen werden in eerste instantie tot bundels gevormd uit een oven, waarna ze met licht van gasontladingslampen (met hetzelfde element) gemanipuleerd werden. Door atomen in een vacuüm op te sluiten worden ze van de omgeving geïsoleerd, waardoor geen warmteuitwisseling plaatsvindt. De ontwikkeling van lasers was een grote stap vooruit. Plotseling waren intense lichtbronnen met extreem smalle lijnbreedte beschikbaar, waardoor atomen effectief gemanipuleerd konden worden. In de jaren '80 werd Dopplerkoeling ontwikkeld, waardoor het mogelijk was om met lasers enorme krachten op atomen uit te oefenen, waardoor atomen van thermische snelheden tot bijna stilstand afgeremd konden worden [7–9]. Doorontwikkeling van Dopplerkoeling leverde de magneto-optische val op [10, 11], afgekort ook wel *MOT* genoemd (*Magneto-Optical Trap*). In een MOT worden atomen in een wolkje gedrukt en in het vacuüm geleviteerd. Atomen in de MOT bereiken temperaturen in de orde van

enkele honderden microkelvin. Voor het ontwikkelen en doorontwikkelen van laserkoeltechnieken hebben Steven Chu, Claude Cohen-Tannoudji en William Philips de Nobelprijs voor Natuurkunde van 1997 in ontvangst mogen nemen.

De MOT biedt een goed beginpunt om Bose-Einstein condensatie te bereiken, maar de temperatuur moet nog met een factor 1000 omlaag voordat de kritische temperatuur bereikt wordt. Om dit te bewerkstelligen worden de atomen overgebracht naar een magnetische val. Vervolgens worden de warmste atomen, die met vele malen de gemiddelde energie, uit de magnetische val verwijderd. De temperatuur van de atoomwolk daalt hierdoor tot onder de kritische temperatuur voor BEC, en een BEC wordt gevormd. Bose-Einsteincondensatie in ultra-koude atomen werd in 1995, 70 jaar na de eerste theoriepapers, gerealiseerd door twee groepen die onafhankelijk van elkaar werkten bij *JILA* [12] en *MIT* [13]. Eric Cornell, Wolfgang Ketterle en Carl Wieman mochten hiervoor in 2001 de Nobelprijs voor Natuurkunde in ontvangst nemen.

Symmetriebreking als signatuur voor een faseovergang

In de moderne natuurkunde worden faseovergangen meestal beschreven aan de hand van een gebroken symmetrie. In het klassieke voorbeeld van bevriezend water, de overgang van een vloeistof naar een vaste stof, zijn deeltjes in eerste instantie vrij om te bewegen in de vloeistof, maar in de vaste stof worden ze klemgezet in een kristalrooster. Als het systeem voldoende groot is, dan heeft de vloeistof een continue translatiesymmetrie: wanneer men zich door de vloeistof beweegt ziet deze er altijd hetzelfde uit. In een vaste stof zitten de deeltjes echter vast in een rooster, waardoor men het systeem enkel “hetzelfde” ziet wanneer men een discrete stap maakt: dit is een discrete translatiesymmetrie. De overgang van vloeistof naar vaste stof breekt dus de continue translatiesymmetrie van de vloeistof. Zowel de vaste stof als de vloeistof hebben een translatiesymmetrie, maar de discrete

translatiesymmetrie van de vaste stof is minder algemeen dan de continue translatiesymmetrie van de vloeistof.

Fysische systemen worden vaak theoretisch beschreven aan de hand van een formule voor de energie in het systeem: de Hamiltoniaan. De Hamiltoniaan heeft soms bepaalde symmetrieën, zoals de translatiesymmetrie uit de vorige alinea. De symmetriebreking kan dan wiskundig worden beschreven. Een symmetrie wordt gebroken genoemd wanneer de toestand van het systeem niet dezelfde symmetrieën heeft als de onderliggende Hamiltoniaan. In het geval van Bose-Einsteincondensatie is de gebroken symmetrie een zogenaamde $U(1)$ -symmetrie, de symmetrie geassocieerd met de fase van een complex getal. De Hamiltoniaan die de dynamica van een BEC beschrijft, zet de complexe fase van de golffunctie niet vast, maar een meting van de fase moet een bepaalde waarde opleveren. Op het moment dat het BEC wordt gevormd, is de fase dus nog onbepaald, maar wanneer deze gemeten wordt, neemt deze een waarde aan. De $U(1)$ symmetrie van de Hamiltoniaan wordt dus spontaan gebroken

Het ruimte-tijkristal

De hoofdstukken in dit proefschrift draaien allemaal om een nieuw fenomeen: het ruimte-tijkristal. In 2012 suggereerde Frank Wilczek dat een systeem op zo'n manier ontworpen kan worden dat het een continue tijdtranslatiesymmetrie breekt in de grondtoestand. Een *tijkristal*, analoog aan de (ruimtelijke) kristallen die de continue ruimtelijke translatiesymmetrie breken [14, 15]. De suggesties van Wilczek werden stevig bekritiseerd en het debat over of de continue tijdtranslatiesymmetrie in de grondtoestand gebroken kan worden is nog steeds gaande [16–18]. Desalniettemin ontstond het onderzoeksveld van discrete tijkristallen, geïnspireerd door de suggesties van Wilczek [19–24]. In een systeem waarin de continue tijdtranslatiesymmetrie al gebroken is door een aandrijvende kracht, kan een discreet tijkristal gerealiseerd worden. Een discreet tijkristaal breekt de symmetrie van de onderliggende Hamiltoniaan. In een systeem, beschreven door een Hamiltoniaan met een tijdsperiodiciteit van

periode T , kan een tijdskristal ontstaan met periode $n \times T$. Een discrete tijdtranslatiesymmetrie wordt dus gebroken, met als gevolg een andere discrete tijdtranslatiesymmetrie met langere periode.

In ons experiment hebben we een ruimte-tijdskristal in een BEC gerealiseerd. Ons BEC is in een sigaarvormige magnetische val gevangen, waardoor het BEC ook de vorm van een sigaar aanneemt. Door in de korte richting van de val te knijpen wordt de breedte van het BEC gemoduleerd. Deze modulatie van de breedte functioneert als aandrijving voor een verzameling van excitaties in de lange richting van de sigaar. Deze excitaties in de lange richting van het BEC oscilleren op precies de helft van de aandrijffrequentie. Hoewel elke experimentele run een net wat ander deeltjesaantal heeft, met variaties tot 10%, zien we de excitaties in de lange richting consistent terug. Dit laat zien dat ons systeem niet gefinetuned hoeft te worden om deze excitaties tevoorschijn te laten komen. Omdat het Bose-Einsteincondensaat een supervloeistof is, is er ook bijna geen wrijving tussen de deeltjes in de wolk en kan de excitatie heel lang bestaan zonder teken van demping. De enige wrijving die de bewegende atomen ondervinden, is met de kleine thermische wolk die na het koelproces overblijft. De excitaties dempen daarom heel erg traag uit, waaruit we kunnen concluderen dat het systeem zich in een pre-thermische toestand bevindt: een toestand die nog moet uitdempen maar dat heel traag doet. Dit proefschrift beschrijft het maken van een pre-thermische, discreet tijdskristal met periodiek ruimtelijk patroon, ofwel een ruimtetijdskristal.

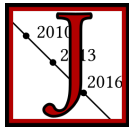
Referenties

- [1] M. Planck, Verhandl. Dtsch. phys. Ges. **2**, 237 (1900).
- [2] S. N. Bose, Zeitschrift für Physik, 178 (1924).
- [3] A. Einstein, Sitzungsberichte der Preußischen Akademie der Wissenschaften zu Berlin, 261 (1924).
- [4] A. Einstein, Sitzungsberichte der Preußischen Akademie der Wissenschaften zu Berlin, 3 (1925).
- [5] E. P. Gross, Il Nuovo Cimento (1955-1965) **20**, 454 (1961).
- [6] L. P. Pitaevskii, J. Exptl. Theoret. Phys. (U.S.S.R.) **40**, 646 (1961).
- [7] T. Hänsch en A. Schawlow, Optics Communications **13**, 68 (1975).
- [8] D. Wineland en H. Dehmelt, Bull. Am. Phys. Soc. **20**, 637 (1975).
- [9] W. D. Phillips en H. Metcalf, Phys. Rev. Lett. **48**, 596 (1982).
- [10] S. Chu, L. Hollberg, J. E. Bjorkholm, A. Cable en A. Ashkin, Phys. Rev. Lett. **55**, 48 (1985).
- [11] E. L. Raab, M. Prentiss, A. Cable, S. Chu en D. E. Pritchard, Phys. Rev. Lett. **59**, 2631 (1987).
- [12] M. H. Anderson, J. R. Ensher, M. R. Matthews, C. E. Wieman en E. A. Cornell, Science **269**, 198 (1995).
- [13] K. B. Davis, M.-O. Mewes, M. R. Andrews, N. J. van Druten, D. S. Durfee, D. M. Kurn en W. Ketterle, Phys. Rev. Lett. **75**, 3969 (1995).
- [14] A. Shapere en F. Wilczek, Phys. Rev. Lett. **109**, 160402 (2012).
- [15] F. Wilczek, Phys. Rev. Lett. **109**, 160401 (2012).
- [16] P. Bruno, Phys. Rev. Lett. **110**, 118901 (2013).
- [17] P. Nozières, Europh. Lett. **103**, 57008 (2013).
- [18] H. Watanabe en M. Oshikawa, Phys. Rev. Lett. **114**, 251603 (2015).
- [19] K. Sacha, Phys. Rev. A **91**, 033617 (2015).
- [20] D. V. Else, B. Bauer en C. Nayak, Phys. Rev. Lett. **117**, 090402 (2016).

-
- [21] D. V. Else, B. Bauer en C. Nayak, *Phys. Rev. X* **7**, 011026 (2017).
- [22] V. Khemani, A. Lazarides, R. Moessner en S. L. Sondhi, *Phys. Rev. Lett.* **116**, 250401 (2016).
- [23] C. W. von Keyserlingk, V. Khemani en S. L. Sondhi, *Phys. Rev. B* **94**, 085112 (2016).
- [24] K. Sacha en J. Zakrzewski, *Rep. Progr. Phys.* **81**, 016401 (2018).



Curriculum Vitæ



ASPER Smits was born in Zuidland, Bernisse, the Netherlands on December 27 1991. He completed his secondary education at Penta College CSG Blaise Pascal in Spijkenisse in 2010. He enrolled in the double bachelor's programme Mathematics and Physics & Astronomy at Utrecht University in the same year, attaining both bachelor degrees with honours. After obtaining his BSc degree he enrolled in the master programme Experimental Physics also at Utrecht University. His research project during his MSc degree (under the supervision of prof. Peter van der Straten) focussed on imprinting phase structures on Bose-Einstein condensates using shaped light in conjunction with an optical Raman transition,. He attained his MSc degree with honours in the fall of 2016. Starting from the second year of his BSc education, he has functioned as a teaching assistant at several physics courses, in particular at the bachelor-level experimental courses.

Consecutively he started as a PhD Candidate in the research group of prof. Peter van der Straten. He continued his research on Bose-Einstein condensates and developed a method to image ultra-cold atoms using off-axis holography. This imaging method is applied to study driven-dissipative dynamics in Bose-Einstein condensates. The imaging method and the result of the following studies can be found in this dissertation. As part of the teaching responsibilities which come with the PhD position, he was part of the team that transitioned the first year programming course away from *Mathematica* and towards *Python*, co-authoring a large part of the syllabus. As a super teaching assistant he



was also responsible for coordinating the experimental part of the DATA course in the year 2019-2020, supervising approximately 8 teaching assistants and 120 students. As part of his PhD project he supervised four students participating in research as part of their MSc degree.

Scientific output

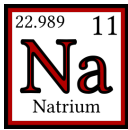
Scientific publications

- *Observation of a space-time crystal in a superfluid quantum gas*, **J. Smits**, L. Liao, H. T. C. Stoof, and P. van der Straten, *Phys. Rev. Lett.* **121**, 185301 (2018).
- *Dynamics of a space-time crystal in an atomic Bose-Einstein condensate*, L. Liao, **J. Smits**, P. van der Straten, and H. T. C. Stoof, *Phys. Rev. A* **99**, 013625 (2019).
- *Imaging trapped quantum gases by off-axis holography*, **J. Smits**, A. P. Mosk, and P. van der Straten, *Opt. Lett.* **45**, 981 (2020).
- *On the long-term stability of space-time crystals*, **J. Smits**, H. T. C. Stoof, and P. van der Straten, *New Journal of Physics* **22**, 105001 (2020).
- *Spontaneous symmetry breaking in a driven-dissipative system*, **J. Smits**, H. T. C. Stoof, and P. van der Straten, arXiv preprint 2103.03748 (2021).

Other Publications

- *Van labboek naar cloudservice*, **J. Smits** and D. van Oosten, *Nederlands Tijdschrift voor Natuurkunde* **85**, 18 (2019).
- *Een ruimte-tijdskristal in een supervloeistof*, **J. Smits**, H. T. C. Stoof, and P. van der Straten, *Nederlands Tijdschrift voor Natuurkunde* **86** (2020).

Dankwoord



ruim vier-en-een-half jaar zwoegen aan een promotieproject, en maar liefst zes-en-een-half jaar in dezelfde onderzoeksgroep leer je, goedschiks of kwaadschiks, dat niemand in zijn eentje de academische wereld aan kan. Ik heb het geluk gehad om tijdens deze periode samen te mogen werken met een geweldige groep mensen die niet alleen op professioneel vlak, maar ook buiten werktijden een steuntje in de rug boden.

Traditiegetrouw begin ik met het bedanken van mijn promotor en dagelijkse begeleider, Peter van der Straten. Peter, toen ik begon aan mijn promotie kenden wij elkaar al goed: Ik had tenslotte mijn masteronderzoek al bij jou volbracht. De beslissing om te blijven voor een promotieproject was dan ook deels gebaseerd op de fijne samenwerking die we dankzij mijn aanstelling in Utrecht konden voortzetten. Over de afgelopen vier-en-half jaar hebben we als een echt team samengewerkt en daarbij een waslijst aan publicaties geproduceerd. Ook al zijn we allebei een beetje koppig: jij meende dat de holografische afbeeldingsmethode waarop een groot deel van dit proefschrift rust echt nooit zou werken voor BECs, ik wilde dingen altijd om mijn manier proberen ook al was jij ervan overtuigd dat jouw suggestie de beste was (en dit was dan ook meer dan eens de waarheid); we hebben altijd overeenstemming kunnen bereiken. Dat jij me uit m'n (soms vastzittende) gedachtegang trok en jouw ideeën aan me "opdrong" heeft mij enorm geholpen om de problemen die we de afgelopen jaren tegenkwamen op te lossen. Ik kijk met goede herinneringen terug op de tijd die we samen hebben mogen werken Peter, bedankt.



En dan Dries: Als co-promotor was jij de sjaak als Peter geen tijd had en ik toch een *slimme jongen* nodig had om ideeën van af te kaatsen. Dikwijls leidden jouw opmerkingen tot nieuwe inzichten en je praktische ervaring in verschillende labs maakte dat jouw advies meer dan eens enkele uren van mijn uitlijntijd heeft afgeschaafd, omdat je altijd een trucje wist waardoor het net wat sneller kon. We deelden een passie voor data netjes opslaan (ook al ging dat voor ons beiden niet vanzelf) en schreven hier zelfs een artikel over in het Nederlands Tijdschrift voor Natuurkunde. Zonder jouw advies en skeptische instelling tegenover tijds kristallen was dit proefschrift niet zo mooi geweest als dat het nu is.

Papers schrijven hoef je gelukkig niet in je eentje te doen. Behalve Peter en Dries heb ik het plezier gehad samen te werken met verschillende collega's in het schrijven van papers. Allard, jouw inzicht in verschillende aspecten van ons onderzoek en de adviezen die je hierover gaf zijn ongelofelijk belangrijk gebleken. In het bijzonder jouw inzichten omtrent de holografische afbeeldingsmethode die bij jou in het lab al zo ingeburgerd was toen wij ermee begonnen hebben ervoor gezorgd dat we netjes om alle hobbels in de weg heen hebben kunnen sturen. Je deur stond altijd open en als je dan eenmaal binnen stapt is het soms lastig om weer te vertrekken, maar altijd met meer kennis dan waarmee je binnen kwam. When it comes to the subject of time crystals: Lei, you were the theory guy that started it all off. We worked together to develop an ab-initio theory on which a large portion of the studies of time crystals in this thesis rest. Wanneer de blik van een theoreet nodig was konden we ook altijd op Henk rekenen en Henk, zonder jouw sturing waren we niet zo ver gekomen.

Elke wetenschappelijke publicatie kent ook haar onbezongen helden. Mensen die een bijdrage leveren in een ondersteunende rol, als technicus of op administratief gebied. Mensen die men niet terugvindt in een auteurslijst (ook al zou dat misschien wel moeten? Een discussie voor een ander moment), maar zonder wie het experiment simpelweg niet zou draaien. Frits, jij zei ooit tegen me: "Ik onderhoud het experiment en jij mag ermee spelen", en hoewel ik altijd protest aantekende, kan ik niet ontkennen dat jij tot je vertrek (jaren na je pensioen, uiteindelijk min of meer definitief

door de coronapandemie) een integrale rol hebt gespeeld bij het draaiende houden van het experiment. Jij hebt me bijna alles geleerd wat ik nu weet over hoe ik met extreem hoog vacuüm moet werken, en ook mijn basiskennis van electronica heb ik voor een deel aan jou te danken. Ik zeg, voor een deel, want ook Dante heeft getracht mij wat over electronica bij te brengen. Voor simpele problemen werd ik geadviseerd om zelf het schema eens te bekijken, mijn voorgestelde oplossing door te spreken, en dan vervolgens ook zelf de soldeerbout te hanteren. En voor de problemen die ik zelf niet kon oplossen was er ook altijd een gaatje. Ook niet te vergeten dat onder toezienend oog van de meester altijd kapotte elektronica van thuis meegebracht kon worden om aan de studententafel een poging te doen deze te repareren, iets waar ik meer dan eens gebruik van heb gemaakt. En dan de andere buurman, Paul. Jij staat altijd voor ons klaar, we komen langs voor een praatje, bespreken wat we nodig hebben, en binnen een half uur ligt er een schets, of sta je al aan de draaibank om even snel wat te fabriceren zodat we verder kunnen. Jij houdt bovendien niet alleen het onderzoek draaiende, maar ook het onderzoeksteam. Als drijvende kracht achter de borrels en de frituurpan houd je de sociale cohesie in het oog.

Aan de optica-en-computers kant stond Cees altijd voor ons klaar. Het schoonmaken van een lastig te kuisen spiegel, zoals in de trillholte van de laser, of een raar probleem met de computer, Cees was de man. Maar ook voor een kort (of wat langer) gesprek over (Amerikaanse) politiek was altijd wel een momentje vrij. Als Cees' opvolger heb jij, Aron, grote schoenen te vullen. In de korte tijd dat ik je ken heb ik met plezier met je samengewerkt. *Last, but not least* van de ondersteunende staf is er Mijke. Problemen met formulieren? Een update van je XS-card nodig? Zin in een obscure boekreferentie? Mijke staat voor je klaar. Jij was mijn maatje en functioneerde dikwijls (onvrijwillig) als praatpaal. Bedankt daarvoor.

Ik wil ook de studenten die ik begeleid heb bedanken: Sanne, Wouter, en Bart. Sanne, zonder jou was de off-axis holography nooit zo ver gekomen als het gekomen is. Jouw inzichten en enthousiasme hebben me een *Believer* gemaakt. Wouter, jij hebt als een machine aan de optical trapping gewerkt. Hierbij behaalde je een niveau met dit deel van de opstelling dat het mijne



oversteeg. Jouw bijdrage is van onschatbare waarde geweest. Bart, ook jouw project richtte zich op de optische val, waarvoor je een mooie modelopstelling bouwde. Uiteindelijk lukte het migreren naar de hoofdopstelling niet, en heb je je tijd besteed aan mij helpen het deeltjesaantal te optimaliseren. Jouw enthousiasme en dreunende muziek heeft mij door die tijd heen gesleept. Allen, bedankt!

Naast mijn promotor en co-promotor was mijn mentor Gerhard Blab van onschatbare waarde. Als ik klem zat en Peter en Dries geen uitkomst boden, kon ik twee verdiepingen afdalen om iemand een blik “van buiten naar binnen” te laten werpen. Je hielp me bij het navigeren van sommige subtiliteiten en was aanspreekpunt. Bedankt voor al je ondersteuning tijdens het promotietraject.

Ik wil ook al mijn collega’s bedanken, en aangezien ik over jullie allemaal wel een alinea kan schrijven, noem ik jullie alleen bij naam, en dan mogen jullie de verhalen erbij denken. Vanuit Nano waren er Jin, Sergei, Ole, Sebas, Pritam (hey lekker ding), Arjon, Pegah, Karindra, Sanli, Jacob, Zhu, Dorian, Javi, Abhi, Sid en Nejc. En natuurlijk mijn vroegere kantoorgenoten Jeroen en Marcel, and my later officemates Bohdan and Dashka. Vanuit het practicum wil ik Peter (van Capel) en de technici Rudi, Pascal en Thierry bedanken voor hun ondersteuning in mijn tijd daar.

Maar steun kwam niet alleen vanuit de academische hoek. Vanuit mijn vriendenkring wil ik graag Anne (de Beurs), Peter (Kristel), Emma, en Naomi (Henkes) bedanken. Eigenlijk heb ik je al genoemd, maar ik wil je toch nog een keer noemen als goede vriend, Jeroen. Eerst als kantoorgenoten, de laatste drie jaar als burens, en het laatste jaar als wandel- & fietsmaatjes hebben we elkaar goed leren kennen. Jij wist je promotie een jaar eerder dan ik af te ronden, maar jij was dan ook eerder begonnen. Je was naast een goede vriend en steun in de rug bij alle vraagstukken academisch bovendien een expert op de off-axis holography en je was niet vies om eventjes een half uurtje in het lab mee te kijken. Bedankt!

Charly, tot jij naar Innsbruck vertrok voor je eigen PhD lunchten we bijna

elke dag samen. Je was een moreel kompas en temperde mij een beetje als ik in extremen schoot. Bovendien was je een goede kompaan om een speciaalbiertje (of vijf) mee te drinken. Ontzettend bedankt. Mijke, ook al genoemd als collega; je was als vriendin een steun in de rug. Naast je secretariële taken was je er voor me als ik niet lekker in mijn vel zat. Dankjewel. Ana, for two years we shared the ups and down of doing a PhD. Hvala ljepa. Roeland, voor al het fietsen, de wijsheden die je over de jaren hebt verstrekt, onze vakanties samen en het biertje als het even niet meer ging, bedankt. Naomi (Khouw), bedankt voor de steun en de aanmoedigingen tijdens de laatste loodjes.

Tot slot wil ik mijn familie bedanken. Bauke, voor het gamen samen, de broodnodige ontsnapping. Anne, voor het verstrekken van een eindeloze voorraad biologiememes. Oma Smits, al ben je er inmiddels niet meer, ik kwam graag bij je langs als ik in Zuidland was. Opa en Oma, Jan en Corrie, voor hun liefde en inzichten, en de zeiltrips. En tot slot, pa en ma, voor de goede zorgen, de steun in de rug, en het altijd beschikbaar stellen van een tweede thuis als toevluchtsoord.

Assessment Committee

Prior to the defense of this dissertation, it was read by an assessment committee to determine whether all requirements the work has to abide by have been met, and whether the work is of a sufficiently high level. I would like to thank the following members of the assessment committee:

- prof. dr. R. A. Duine, Institute for Theoretical Physics, Utrecht University
- prof. dr. L. R. M. Maas, Institute for Marine and Atmospheric research (IMAU), Utrecht University
- prof. dr. A. P. Mosk, Debye Institute for Nanomaterials Science, Utrecht University
- prof. dr. K. Sacha, Institute of Theoretical Physics, Jagiellonian University in Krakow
- prof. dr. F. E. Schreck, Van der Waals-Zeeman Instituut, University of Amsterdam

